

TOPOLOGICAL INSULATORS AND SEMIMETALS:
THEORY FOR BULK AND SURFACE ELECTRONIC PROPERTIES

DISSERTATION

zur Erlangung des Doktorgrades der Naturwissenschaften
(Dr. rer. nat.)

der

Naturwissenschaftlichen Fakultät II
Chemie, Physik und Mathematik

der

MARTIN-LUTHER-UNIVERSITÄT
HALLE-WITTENBERG

vorgelegt von

TOMÁŠ RAUCH

geboren am 17.12.1986 in Frýdlant (Tschechische Republik)

Erstgutachterin: Prof. Dr. Ingrid Mertig
Zweitgutachter: Prof. Dr. Steffen Trimper
Drittgutachter: Prof. Dr. Markus Donath

Tag der öffentlichen Verteidigung: 13.07.2016
Vorsitzender der Promotionskommission: Prof. Dr. Jörg Schilling

ABSTRACT

In the present thesis, electronic properties of topologically non-trivial materials are investigated. Theoretical calculations of electronic band structures for various system geometries are performed by means of an *ab initio* based Tight-Binding model. The related topological invariants are calculated for both insulating and metallic materials by methods based on the Berry-phase concept. Topological phase diagrams are generated, showing the different topological phases which can be entered by the examined systems under a change of external parameters, such as strain, disorder or magnetic field. These results are confirmed by simultaneous investigations of the surface electronic band structure featuring topologically protected surface states in the case of non-trivial topological phases.

In der vorliegenden Arbeit werden die elektronischen Eigenschaften topologisch nicht-trivialer Materialien untersucht. Unter Verwendung des auf *ab initio*-Rechnungen basierenden Tight-Binding-Modells werden für verschiedene Systemgeometrien elektronische Bandstrukturen berechnet. Für isolierende und metallische Materialien werden zudem die entsprechenden topologischen Invarianten mit Hilfe des Berry-Phasen-Konzepts bestimmt. Anschließend werden topologische Phasendiagramme erstellt, die die verschiedenen topologischen Phasen zeigen, die von den untersuchten Systemen unter Änderung externer Parameter wie der Verzerrung, Unordnung oder magnetischen Feldes eingenommen werden können. Diese Ergebnisse werden weiterhin bestätigt durch Berechnungen der elektronischen Bandstruktur an Oberflächen der entsprechenden Systeme, die im Falle nichttrivialer topologischer Phasen topologisch geschützte Oberflächenzustände beinhalten.

CONTENTS

List of Figures	9
List of Acronyms	11
1 INTRODUCTION	13
2 BERRY PHASE, CONNECTION AND CURVATURE	15
2.1 Introduction	15
2.2 Basic Quantities	15
2.3 Non-Abelian Formulation	17
2.4 Berry Phase in Solid State Physics	18
3 ELECTRONIC STRUCTURE CALCULATIONS	19
3.1 Introduction	19
3.2 Tight-Binding	19
4 CLASSES OF TOPOLOGICAL INSULATORS	35
4.1 Introduction	35
4.2 Integer Quantum Hall Effect	35
4.3 Chern Insulators	36
4.4 2D Time-Reversal Invariant Topological Insulators	37
4.5 3D Time-Reversal Invariant Topological Insulators	45
4.6 3D Topological Crystalline Insulators	47
5 TOPOLOGICAL SEMIMETALS	51
5.1 Introduction	51
5.2 Topological Dirac Semimetals	51
5.3 Weyl Semimetals	53
6 PUBLICATIONS	57
6.1 Introduction	57
6.2 Pressure-induced Topological Phase Transitions in Rocksalt Chalcogenides	57
6.3 Dual Topological Character of Chalcogenides: Theory for Bi_2Te_3	64
6.4 Nontrivial Interface States Confined between two Topological Insulators	73
6.5 Spin Chirality Tuning and Topological Semimetals in Strained $\text{HgTe}_x\text{S}_{1-x}$	83
7 CONCLUSIONS	93
Bibliography	95
List of Publications	103
Eidesstattliche Erklärung	105
Curriculum Vitae	107

LIST OF FIGURES

Figure 3.1	Comparison of a DFT calculated band structure with the TB fit.	25
Figure 4.1	Surface state in the 1D edge BZ of a Chern insulator.	38
Figure 4.2	TRIMs in a 2D BZ.	39
Figure 4.3	Discretized BZ for the evaluation of the Fu-Kane formula.	40
Figure 4.4	Wannier function centers for Bi_2Te_3	43
Figure 4.5	Surface states in the surface BZ of a 2D TI of the QSHE type.	44
Figure 4.6	Time-reversal invariant planes in a 3D insulator.	46
Figure 4.7	Surface states in strong and weak topological insulators.	48
Figure 4.8	Mirror planes in the bulk and surface BZ.	49
Figure 5.1	Bulk and surface Dirac states in the BZ of a topological Dirac semimetal.	52
Figure 5.2	Phase transition between different insulating and metallic topological phases.	54
Figure 5.3	Weyl states and Fermi arcs in the BZ of a Weyl semimetal.	55
Figure 6.1	Band gap size of PbA , $A = \text{S, Se, Te}$ for different lattice constants.	58
Figure 6.2	Surface electronic structure of $\text{HgTe}(100)$ under strain featuring both surface and bulk Dirac cones.	84

LIST OF ACRONYMS

1D	one-dimensional
2D	two-dimensional
3D	three-dimensional
ABC	accidental band crossing
ARPES	angle-resolved photoelectron spectroscopy
BZ	Brillouin zone
CPA	coherent-potential approximation
DFT	density-functional theory
IS	inversion symmetry
MLWF	maximally localized Wannier function
QHE	quantum Hall effect
QSHE	quantum spin Hall effect
SHE	spin Hall effect
SK	Slater-Koster
SOC	spin-orbit coupling
STI	strong topological insulator
STM	scanning tunnelling microscopy
TB	tight-binding
TCI	topologically crystalline insulator
TDS	topological Dirac semimetal
TI	topological insulator
TRIM	time-reversal invariant momentum
TRS	time-reversal symmetry
VCA	virtual-crystal approximation
WSM	Weyl semimetal
WTI	weak topological insulator

INTRODUCTION

In solid state physics, diverse properties of crystalline materials are examined. Especially the knowledge of their electronic properties is of major interest, since it is the basis of the whole field of electronics, a technology present in almost all aspects of our life. In the last two decades, novel phenomena in the electronic structure of solids were discovered, which improve our understanding of basic quantum mechanical properties of electrons in solids. Materials featuring these phenomena are called topological.

Topological materials and in particular topological insulators (TIs) are systems whose occupied electronic bulk states possess a unique electronic structure that can be characterized by integer numbers. These integers, called invariants, cannot change their values under a smooth change of the electronic properties of the system – the bulk band structure. This explains why the materials are called ‘topological’, reminding of the mathematical field topology, in which the properties of objects are studied that stay unchanged under continuous deformations.

In condensed matter, the non-trivial topological character of occupied electronic bulk states is intimately related to the presence of surface states. These have to cross the insulating fundamental band gap and are therefore always cut by the system Fermi energy, independent of its value. Connecting this idea with the fact that this property does not change under a continuous variation of the system leads to the conclusion that these surface states are peculiarly stable, especially when compared with surface states of topologically trivial materials. The latter can be pushed completely out of the band gap by manipulating the system. This unique property of topological materials, connected with others, such as the spin polarization of the surface states or their suppressed backscattering, makes them a very interesting object of investigations in solid state physics, aiming at both a better understanding of basic principles of quantum mechanical solid state systems and their application in modern technologies.

The story of topological materials began in the 1980s with the discovery of the quantum Hall effect (QHE) [1] and its first theoretical explanations [2], soon leading to the so-called TKNN invariant [3], a topological invariant that does not change its value as long as the electronic structure is subject to only smooth changes. Today the TKNN invariant is called the Chern number and QHE systems are considered as the first topological systems observed. While in the QHE the topologically non-trivial character is generated by an external magnetic field and the system becomes trivial when the field is switched off, in real topological materials the non-trivial character occurs without any external fields. Such systems were first found in the 2000s, originally in two-dimensional (2D) and later also in three-dimensional (3D) systems. Since then, many groups world-wide have been investigating the special properties of topological materials and their surface states. The behaviour of the bulk and surface electronic states under additional effects like strain, adlayer deposition, alloying or external fields is studied. In addition, transport proper-

ties of the systems or the possibility of switching between trivial and non-trivial phases are probed.

For experimental investigations typically two techniques are used. The angle-resolved photoelectron spectroscopy (ARPES) allows for the visualization of both bulk and surface electronic band structures. By this technique, the presence of topologically protected surface states can be confirmed directly, along with its dispersion and special properties such as the spin polarization [4, 5]. A second experimental technique capable of probing especially the unique transport properties of (mostly) the surface states, is the scanning tunnelling microscopy (STM) [6–8]. Additionally, the surface states can be visualized in real space.

Owing to their peculiar properties, topological materials are proposed to be promising candidates for various applications. The suppressed backscattering leading to lower energy losses and the so-called spin-momentum locking – states with a given wave vector possess a fixed spin orientation, the opposite orientation is forbidden – make topological materials good candidates for spin generators and conductors, which could be used in the field of spin electronics, short spintronics [9]. A second widely discussed possible application of topological materials is their presence in future quantum computers. The combination of a TI with a superconductor can give rise to so-called Majorana fermions [10], which could be used as qubits of a quantum computer acting as the basic information storage unit and replacing the classical bits of conventional computers.

In the present thesis, various properties of different topological materials are investigated by theoretical calculations. For TIs and semimetals of diverse types the topological invariants of the occupied bulk electronic states are calculated together with the dispersion relation of the associated surface electronic states. These main properties are investigated under different circumstances such as strain or substitutional disorder. The materials studied are predominantly Bi-chalcogenides (e.g., Bi_2Te_3), rocksalt chalcogenides (e.g., SnTe) and zincblende semiconductors (e.g., HgTe). All calculations are performed by means of an *ab initio* based tight-binding (TB) model, proving excellent for a comprehensive study of topological materials, as it unites all necessary steps in one common model capable of simulating all possible distortions of the system as well as the calculation of the topological invariants and the surface electronic structure.

This thesis is organized as follows: In chapter 2, the concept of Berry phase is introduced and all related quantities are derived. In chapter 3, the TB model is presented, including the modifications required for the calculation of the results of the thesis. In the following two chapters, an overview over TIs (chapter 4) and topological metals (chapter 5) is given. As this is a cumulative thesis, published results can be found in chapter 6, including a short comment on each of the publications. Finally, a conclusion is given in chapter 7.

The overall aim of this thesis is to provide a better understanding of topological properties of crystalline materials, to identify the topological phases accessible in the systems under consideration and to study the behaviour of their electronic properties during phase transitions between various topological phases.

 BERRY PHASE, CONNECTION AND CURVATURE

2.1 INTRODUCTION

The basis for understanding topological properties in solid state physics was given by M. V. Berry. In his work [11] he introduced the geometrical phase accompanying adiabatic changes. This phase, now called Berry phase, and the connected quantities, Berry connection and curvature, are used for calculating the so called topological invariants, which themselves allow to distinguish between specific topology classes.

In common physical problems, it is impossible to consider all influences of the universe on the investigated system. As an approximation, they can be either neglected completely or they can be at least considered as parameters of the Hamiltonian describing the system. This is allowed if the parameters change slowly in comparison to the internal degrees of freedom of the system. The Berry phase emerging in such systems can therefore be seen as a compensation for the adiabatic approximation and it describes the effects of the universe surrounding the otherwise decoupled system.

2.2 BASIC QUANTITIES

The derivation of the quantities follows the original work of Berry. Assume a Hamiltonian $\hat{H} = \hat{H}(\mathbf{R})$ with \mathbf{R} being a 3D parameter. When $\mathbf{R} = \mathbf{R}(t)$ varies slowly with time t , then the adiabatic approximation [12] can be applied. This means that a system which starts in the state $|n(\mathbf{R})\rangle$ with

$$\hat{H}(\mathbf{R}) |n(\mathbf{R})\rangle = E_n(\mathbf{R}) |n(\mathbf{R})\rangle \quad (2.1)$$

at $t = 0$ stays in the same state $|n(\mathbf{R}(t))\rangle$ for any time t . $|n(\mathbf{R}(t))\rangle$ is then eigenstate of $\hat{H}(\mathbf{R}(t))$.

The ansatz for the eigenstate $|\psi(\mathbf{R}(t))\rangle$ of the time-dependent Hamiltonian $\hat{H}(\mathbf{R}(t))$ can be chosen as

$$|\psi(\mathbf{R}(t))\rangle = \exp \left\{ -\frac{i}{\hbar} \int_0^t E_n(\mathbf{R}(t')) dt' \right\} \exp \{i\gamma_n(t)\} |n(\mathbf{R}(t))\rangle. \quad (2.2)$$

The first phase is the common dynamical phase. The second phase factor possesses the geometrical or Berry phase $\gamma_n(t)$ which will be derived in the following. Since the time-dependent Schrödinger equation

$$\hat{H}(\mathbf{R}(t)) |\psi(\mathbf{R}(t))\rangle = i\hbar \frac{d}{dt} |\psi(\mathbf{R}(t))\rangle \quad (2.3)$$

has to be satisfied by $|\psi(\mathbf{R}(t))\rangle$, an equation for the Berry phase can be obtained by inserting equation (2.2) into equation (2.3):

$$\dot{\gamma}_n(t) = i \langle n(\mathbf{R}(t)) | \nabla_{\mathbf{R}} n(\mathbf{R}(t)) \rangle \dot{\mathbf{R}}(t). \quad (2.4)$$

Assuming that the system propagates along a closed loop C in the parameter space with $\mathbf{R}(t=0) = \mathbf{R}(t=T)$, then the total phase gathered along C can be expressed as

$$\gamma_n(C) = i \oint_C \langle n(\mathbf{R}) | \nabla_{\mathbf{R}} n(\mathbf{R}) \rangle d\mathbf{R}. \quad (2.5)$$

Since the Berry phase $\gamma_n(C)$ has to be real, the integrand $\langle n(\mathbf{R}) | \nabla_{\mathbf{R}} n(\mathbf{R}) \rangle$ has to be purely imaginary. This is always fulfilled since

$$0 = \nabla_{\mathbf{R}} 1 = \nabla_{\mathbf{R}} \langle n(\mathbf{R}) | n(\mathbf{R}) \rangle = \langle \nabla_{\mathbf{R}} n(\mathbf{R}) | n(\mathbf{R}) \rangle + \langle n(\mathbf{R}) | \nabla_{\mathbf{R}} n(\mathbf{R}) \rangle \quad (2.6)$$

and

$$\langle \nabla_{\mathbf{R}} n(\mathbf{R}) | n(\mathbf{R}) \rangle = - \langle n(\mathbf{R}) | \nabla_{\mathbf{R}} n(\mathbf{R}) \rangle = \langle n(\mathbf{R}) | \nabla_{\mathbf{R}} n(\mathbf{R}) \rangle^*. \quad (2.7)$$

The integrand

$$A_n(\mathbf{R}) := i \langle n(\mathbf{R}) | \nabla_{\mathbf{R}} n(\mathbf{R}) \rangle \quad (2.8)$$

in equation (2.5) is called Berry connection. This quantity is not gauge invariant, which can be seen by multiplying the state $|n(\mathbf{R})\rangle$ by an arbitrary phase factor $|n(\mathbf{R})\rangle \rightarrow e^{i\phi(\mathbf{R})} |n(\mathbf{R})\rangle$. The Berry connection transforms as $A_n(\mathbf{R}) \rightarrow -\nabla_{\mathbf{R}}\phi(\mathbf{R}) + A_n(\mathbf{R})$. Since it is often more comfortable to operate with gauge invariant quantities, the Berry curvature is defined as the curl of the Berry connection, causing the gradient field $-\nabla_{\mathbf{R}}\phi(\mathbf{R})$ to vanish:

$$\Omega_n(\mathbf{R}) := \nabla_{\mathbf{R}} \times A_n(\mathbf{R}) = i \langle \nabla_{\mathbf{R}} n(\mathbf{R}) | \times | \nabla_{\mathbf{R}} n(\mathbf{R}) \rangle. \quad (2.9)$$

This behavior is similar to the connection between the magnetic field and the vector potential in electrodynamics.

In the following, the expression for the Berry phase will be re-written. The aim is to get a formula for the Berry curvature which includes derivatives of the Hamiltonian $\nabla_{\mathbf{R}} \hat{H}$ instead of the derivatives of the eigenstates $\nabla_{\mathbf{R}} |n(\mathbf{R})\rangle$. This brings many advantages for numerical evaluation of the Berry curvature, since the derivative of the Hamiltonian can be calculated analytically in many cases. The parameter \mathbf{R} will be omitted in some of the equations for simplicity.

For an arbitrary surface S having the closed line C as an edge, the application of Stokes' theorem to equation (2.5) gives

$$\gamma_n(C) = \int_{C=\partial S} A d\mathbf{R} = \iint_S \Omega d\mathbf{S} = i \iint_S \sum_{m \neq n} \langle \nabla n | m \rangle \times \langle m | \nabla n \rangle d\mathbf{S}. \quad (2.10)$$

In the last step, the completeness relation $\hat{1} = \sum_m |m\rangle \langle m|$ was used. The $m = n$ terms have to vanish, since $\langle \nabla n | n \rangle$ is imaginary and $i \langle \nabla n | n \rangle \times \langle n | \nabla n \rangle$ would give an imaginary contribution to the Berry phase.

By applying the gradient operator on the stationary Schrödinger equation (2.1), we get

$$\nabla (\hat{H} |n\rangle) = \nabla (E_n |n\rangle) \Leftrightarrow \nabla \hat{H} |n\rangle + \hat{H} |\nabla n\rangle = \nabla E_n |n\rangle + E_n |\nabla n\rangle.$$

Multiplication by $\langle m|$ from left leads to

$$\langle m | \nabla n \rangle = \frac{\langle m | \nabla \hat{H} | n \rangle}{E_n - E_m}, \quad (2.11)$$

which can be plugged into equation (2.10). The final expression for the Berry curvature becomes

$$\Omega_n(\mathbf{R}) = i \sum_{m \neq n} \frac{\langle n(\mathbf{R}) | \nabla_{\mathbf{R}} \hat{H}(\mathbf{R}) | m(\mathbf{R}) \rangle \times \langle m(\mathbf{R}) | \nabla_{\mathbf{R}} \hat{H}(\mathbf{R}) | n(\mathbf{R}) \rangle}{(E_n(\mathbf{R}) - E_m(\mathbf{R}))^2}. \quad (2.12)$$

This equation can be directly applied for evaluating the Berry curvature numerically, since only the eigenstates, eigenvalues and the gradient of the Hamiltonian are used as input. The former two can be received by solving the stationary Schrödinger equation, the latter can be calculated analytically.

The dependence of the Berry curvature on the energy spectrum can be qualitatively studied already in equation (2.12). Due to $E_m - E_n$ in the denominator, the Berry curvature becomes large predominantly in the cases where the states are energetically close to each other. Ω_n diverges for degenerate states.

A further consequence of equation (2.12) is the fact that the Berry curvature of one state n can be calculated from the properties of all other states $m \neq n$. This is a manifestation of the fact stated earlier, that the Berry phase (given by the Berry curvature) is a kind of a compensation for the adiabatic approximation, which in this case constrains the system to stay in the state $|n(\mathbf{R})\rangle$.

2.3 NON-ABELIAN FORMULATION

The previous discussion is only valid for a single non-degenerate eigenvalue. The approach is called Abelian, because an interchange of two identical (quasi-)particles produces only a one-dimensional (1D) phase factor to the wave functions, whose multiplications are commutative. In a more general approach a set of N states energetically isolated from other electronic states by a finite energy gap for any value of the parameter \mathbf{R} – i.e. which have no degeneracies with other states, but may be degenerate with each other – becomes a vector. Interchanging these states can be described by matrices, whose multiplication is not commutative [13]. Therefore the approach is called non-Abelian.

Since degeneracies occur in many systems, it is important to be able to handle them in order to evaluate the Berry curvature for real systems. This is possible with the non-Abelian formulation of the previous quantities [14]. For N states energetically separated from the rest both the non-Abelian Berry connection \mathcal{A} and Berry curvature \mathcal{F} are vector-valued matrices of rank N ,

$$A_{n,m}(\mathbf{R}) = i \langle n(\mathbf{R}) | \nabla_{\mathbf{R}} m(\mathbf{R}) \rangle, \quad n, m \in \Sigma. \quad (2.13)$$

and

$$\mathcal{F}(\mathbf{R}) = \nabla_{\mathbf{R}} \times \mathcal{A}(\mathbf{R}) - i \mathcal{A}(\mathbf{R}) \times \mathcal{A}(\mathbf{R}), \quad (2.14)$$

$$F_{n,m}(\mathbf{R}) = i \langle \nabla_{\mathbf{R}} n(\mathbf{R}) | \times | \nabla_{\mathbf{R}} m(\mathbf{R}) \rangle + i \sum_{k \in \Sigma} \langle n(\mathbf{R}) | \nabla_{\mathbf{R}} k(\mathbf{R}) \rangle \times \langle k(\mathbf{R}) | \nabla_{\mathbf{R}} m(\mathbf{R}) \rangle, \quad n, m \in \Sigma. \quad (2.15)$$

Σ is the subspace of the Hamiltonian spanned by the N eigenstates. In equation (2.14) the curl was replaced by the covariant derivative [15] $D_{\mathbf{R}} = \nabla_{\mathbf{R}} - i \mathcal{A}(\mathbf{R}) \times$. In the formula for the non-Abelian Berry curvature in equation (2.15) the derivatives of the eigenstates can be substituted by the derivative of the Hamiltonian in the same way as in equation (2.12). The final expression which can be used for practical calculations is

$$F_{n,m}(\mathbf{R}) = i \sum_{k \notin \Sigma} \frac{\langle n(\mathbf{R}) | \nabla_{\mathbf{R}} \hat{H}(\mathbf{R}) | k(\mathbf{R}) \rangle \times \langle k(\mathbf{R}) | \nabla_{\mathbf{R}} \hat{H}(\mathbf{R}) | m(\mathbf{R}) \rangle}{(E_n(\mathbf{R}) - E_k(\mathbf{R})) (E_m(\mathbf{R}) - E_k(\mathbf{R}))}. \quad (2.16)$$

Again, the non-Abelian Berry curvature of the states $n, m \in \Sigma$ is partially given by the properties of the other bands $k \notin \Sigma$. In contrast to the Abelian Berry curvature, there is

no longer a singularity in the formula for the non-Abelian case, since the denominator in equation (2.16) can never equal zero.

Another difference between the Abelian and non-Abelian approach is that the non-Abelian Berry curvature is not gauge invariant. A unitary transformation $\mathcal{U} \in SU(N)$ of the N states yields

$$\mathcal{A}'(\mathbf{R}) = \mathcal{U}(\mathbf{R}) \mathcal{A}(\mathbf{R}) \mathcal{U}^\dagger(\mathbf{R}) + i(\nabla_{\mathbf{R}} \mathcal{U}(\mathbf{R})) \mathcal{U}^\dagger(\mathbf{R}), \quad (2.17)$$

$$\mathcal{F}'(\mathbf{R}) = \mathcal{U}(\mathbf{R}) \mathcal{F}(\mathbf{R}) \mathcal{U}^\dagger(\mathbf{R}). \quad (2.18)$$

2.4 BERRY PHASE IN SOLID STATE PHYSICS

In the previous section, the Berry phase and all the other quantities were derived for general Hamiltonians with an adiabatic dependence on the parameter \mathbf{R} . The concept of the Berry phase should be used for solid state systems. It will be shown that the wave vector \mathbf{k} plays the role of the parameter \mathbf{R} in lattice-periodic crystals [16].

We start with the Bloch theorem [17] for independent electrons under the influence of a periodic potential $V(\mathbf{r}) = V(\mathbf{r} + \mathbf{R})$. In this context, \mathbf{R} is a lattice vector, not the parameter of the Hamiltonian, as was the case in the previous section. The one-electron wave function then satisfies

$$\psi_{n,\mathbf{k}}(\mathbf{r}) = e^{i\mathbf{k}\mathbf{r}} u_{n,\mathbf{k}}(\mathbf{r}) \quad (2.19)$$

with $u_{n,\mathbf{k}}(\mathbf{r})$ being the lattice-periodic part of the wave function,

$$u_{n,\mathbf{k}}(\mathbf{r}) = u_{n,\mathbf{k}}(\mathbf{r} + \mathbf{R}). \quad (2.20)$$

The wave function (2.19) can be plugged into the stationary Schrödinger equation $\hat{H}\psi_{n,\mathbf{k}}(\mathbf{r}) = E_{n,\mathbf{k}}\psi_{n,\mathbf{k}}(\mathbf{r})$. Multiplying by $e^{-i\mathbf{k}\mathbf{r}}$ from left gives then

$$\underbrace{e^{-i\mathbf{k}\mathbf{r}} \hat{H} e^{i\mathbf{k}\mathbf{r}}}_{\hat{H}(\mathbf{k})} u_{n,\mathbf{k}}(\mathbf{r}) = E_{n,\mathbf{k}} u_{n,\mathbf{k}}(\mathbf{r}). \quad (2.21)$$

Equation (2.21) is a new stationary Schrödinger equation with a new Hamiltonian $\hat{H}(\mathbf{k})$ depending parametrically on the wave vector \mathbf{k} . The new eigenvalues are the same as the former ones, but the new eigenstates are only the periodic parts of the electronic wave functions.

Having a Hamiltonian with a parameter \mathbf{k} , the quantities from section 2.2 can be defined in the same way for solid state systems:

$$\gamma_n = i \oint_C d\mathbf{k} \langle u_n(\mathbf{k}) | \nabla_{\mathbf{k}} u_n(\mathbf{k}) \rangle, \quad (2.22)$$

$$\mathbf{A}_n(\mathbf{k}) = i \langle u_n(\mathbf{k}) | \nabla_{\mathbf{k}} u_n(\mathbf{k}) \rangle, \quad (2.23)$$

$$\mathbf{\Omega}_n(\mathbf{k}) = i \langle \nabla_{\mathbf{k}} u_n(\mathbf{k}) | \times | \nabla_{\mathbf{k}} u_n(\mathbf{k}) \rangle. \quad (2.24)$$

From this point of view one can understand that the Berry curvature plays a significant role in many properties of solids, since it follows directly from the electronic band structure, without need for additional quantities.

ELECTRONIC STRUCTURE CALCULATIONS

3.1 INTRODUCTION

One possibility to understand the behaviour of electrons in solids is to perform quantum mechanical electronic structure calculations, i.e. to determine the eigenvalues and eigenfunctions of the Hamiltonian describing the solid system. Since this task would exceed our computational capabilities in most of the cases, typically the Born-Oppenheimer approximation [18] decoupling the electron motion from the one of the ions and the one-electron approximation are applied. In the latter it is assumed, that the potential of each electron can be described as a sum of the ionic potential and an effective potential combining the coupling between the one electron considered and all the other electrons in the crystal.

To finally calculate the electronic structure, an appropriate approach has to be chosen from the variety of models differing in quality of description, complexity, computational effort, etc. In this thesis the tight-binding (TB) model was used, which can be settled approximately in the middle, concerning both the quality and the computational effort of the model.

3.2 TIGHT-BINDING

The TB model is for many reasons a suitable tool for investigating topological materials. In the first place, the basic assumption of the model is that the wave functions of the crystal electrons are similar to atomic wave functions, which is often very accurate for the occupied states below the Fermi energy, but does not hold for excited states. Therefore, only a part of the band structure located in the energy region of interest is considered, neglecting the interaction with the energetically distant states (e.g., high-lying excited states or tightly-bound low-energy core states). Since the properties of topological materials are predominantly given by the occupied states, as shown in the following chapters, TB is a valid model to describe them.

Another advantage of the TB model is the possibility to simulate various geometries of the investigated crystal, including bulk, surfaces, interfaces and slabs, which is very useful for simulating topological materials, whose bulk and surface properties are tightly connected with each other. TB allows to investigate these properties within a single approach.

Finally, based on a calculation for an initial configuration performed by a more accurate approach, the TB model is capable of simulating variations of this configuration, such as strain or disorder, reliably and with low computational effort. The possibil-

ity to calculate and handle both electronic wave functions and Green functions for the different geometries makes TB a versatile tool for describing topological materials.

The first widely used variant of the TB model was introduced by Slater and Koster [19]. This approach will be used, although further developed, more complicated methods are available [20]. The original Slater-Koster method proved reliable enough for describing various materials when based on *ab initio* calculations.

3.2.1 Tight-Binding Matrix

In TB it is assumed that the one-electron Hamiltonian consists of the kinetic energy of the electron and the potential energy, which is a sum of attractive potentials localized at the atomic positions. Since the electrons are assumed to be bound by the potential, the electronic wave function should be similar to an atomic wave function. Therefore, the basis set consists of sums of atomic orbitals $\phi_\sigma(\mathbf{r} - \mathbf{R}_i - \mathbf{t}_l)$ located at the core positions $\mathbf{R}_i + \mathbf{t}_l$, multiplied by a phase factor $e^{i\mathbf{k}\mathbf{R}_i}$ which ensures the Bloch theorem [17] is fulfilled. \mathbf{R}_i denotes the vector to the i -th unit cell and \mathbf{t}_l is the vector to the l -th atom inside the unit cell. The ansatz for the wave function is a linear combination of these Bloch sums,

$$\psi_{n,\mathbf{k}}(\mathbf{r}) = \frac{1}{\sqrt{N}} \sum_{\alpha} c_{n,\alpha}(\mathbf{k}) \sum_{\mathbf{R}_i} e^{i\mathbf{k}\mathbf{R}_i} \phi_{\sigma}(\mathbf{r} - \mathbf{R}_i - \mathbf{t}_l). \quad (3.1)$$

The summation index α in the first sum is a multiindex $\alpha = (\sigma, l)$ combining the orbital quantum numbers σ and the atomic position \mathbf{t}_l in one primitive cell. The summation in the second sum is over all N lattice vectors \mathbf{R}_i of the crystal.

For further calculations it will be assumed that the atomic orbitals localized at different sites are orthogonal,

$$\langle \phi_{\sigma'}(\mathbf{r} - \mathbf{R}_j - \mathbf{t}_m) | \phi_{\sigma}(\mathbf{r} - \mathbf{R}_i - \mathbf{t}_l) \rangle \sim \delta_{\sigma,\sigma'} \delta_{\mathbf{R}_i, \mathbf{R}_j} \delta_{l,m} = \delta_{\alpha,\beta} \delta_{\mathbf{R}_i, \mathbf{R}_j}. \quad (3.2)$$

This is practically achieved by the Löwdin transformation [21]. The new basis set is then a linear combination of atomic orbitals as well. These basis functions are orthogonal but they still possess the symmetry properties of the original orbitals. Since the matrix elements of the Hamiltonian \hat{H} including the basis functions will be used as adjustable parameters in the calculations, it is not necessary to know the precise form of the basis functions.

Since $\psi_{n,\mathbf{k}}(\mathbf{r})$ has to be normalized,

$$\sum_{\alpha} |c_{n,\alpha}(\mathbf{k})|^2 \stackrel{!}{=} 1. \quad (3.3)$$

In the following a matrix expression for the TB problem will be derived. Plugging the ansatz (3.1) into the Schrödinger equation

$$\langle \psi_{n,\mathbf{k}} | \hat{H} | \psi_{n,\mathbf{k}} \rangle = E_{n,\mathbf{k}} \quad (3.4)$$

we get

$$\begin{aligned} & \frac{1}{N} \sum_{\alpha,\beta} c_{n,\alpha}^*(\mathbf{k}) c_{n,\beta}(\mathbf{k}) \times \\ & \times \sum_{\mathbf{R}_i, \mathbf{R}_j} e^{i\mathbf{k}(\mathbf{R}_i - \mathbf{R}_j)} \langle \phi_{\sigma'}(\mathbf{r} - \mathbf{R}_j - \mathbf{t}_m) | \hat{H} | \phi_{\sigma}(\mathbf{r} - \mathbf{R}_i - \mathbf{t}_l) \rangle = E_{n,\mathbf{k}}. \end{aligned} \quad (3.5)$$

Because of lattice periodicity, $\mathbf{R}_i = 0$ can be chosen as a reference cell. The TB matrix is then defined as

$$\begin{aligned} H_{\alpha,\beta}(\mathbf{k}) &= \frac{1}{N} \sum_{\mathbf{R}_i, \mathbf{R}_j} e^{i\mathbf{k}(\mathbf{R}_i - \mathbf{R}_j)} \langle \phi_{\sigma'}(\mathbf{r} - \mathbf{R}_j - \mathbf{t}_m) | \hat{H} | \phi_{\sigma}(\mathbf{r} - \mathbf{R}_i - \mathbf{t}_l) \rangle \\ &= \sum_{\mathbf{R}_j} e^{-i\mathbf{k}\mathbf{R}_j} \langle \phi_{\sigma'}(\mathbf{r} - \mathbf{R}_j - \mathbf{t}_m) | \hat{H} | \phi_{\sigma}(\mathbf{r} - \mathbf{t}_l) \rangle. \end{aligned} \quad (3.6)$$

With the TB matrix in equation (3.6) the equation (3.5) can be written as an eigenvalue problem for the expansion coefficients:

$$\sum_{\alpha,\beta} c_{n,\alpha}^*(\mathbf{k}) H_{\alpha,\beta}(\mathbf{k}) c_{n,\beta}(\mathbf{k}) = \sum_{\alpha,\beta} E_n(\mathbf{k}) c_{n,\alpha}^*(\mathbf{k}) c_{n,\beta}(\mathbf{k}) \delta_{\alpha,\beta}. \quad (3.7)$$

$\underline{H}(\mathbf{k}) := \{H_{\alpha,\beta}(\mathbf{k}) : \alpha, \beta = 1, \dots, N_b\}$ is the TB matrix and $\underline{c}_n(\mathbf{k}) := \{c_{n,\alpha}(\mathbf{k}) : \alpha = 1, \dots, N_b\}$ is the vector of the expansion coefficients. N_b is the number of basis functions considered.

The sum over all lattice cells \mathbf{R}_j in equation (3.6) cannot be evaluated exactly in real calculations. The number of neighbouring atoms considered has to be restricted, same as the number of orbitals N_b considered at one atom. The description of electronic properties improves with increasing number of neighbours and orbitals considered, but the calculation becomes computationally more demanding. Therefore the approximations have to be chosen properly. For the systems considered in this work, nearest and next-nearest neighbours and the atomic s , p and d atomic orbitals in the energy range of interest are considered.

3.2.2 Slater-Koster Formalism

The TB matrix (3.6) includes the integrals $\langle \phi_{\sigma'}(\mathbf{r} - \mathbf{R}_j - \mathbf{t}_m) | \hat{H} | \phi_{\sigma}(\mathbf{r} - \mathbf{t}_l) \rangle$. Since the potential in the Hamiltonian \hat{H} was supposed to be a sum of atomic potentials, these integrals can be divided into three types. When both atomic orbitals and the potential are localized at the same atom $j = 0$, the integral is called on-site integral. The corresponding diagonal element $H_{\alpha,\alpha} = \epsilon_{\alpha}$ has no \mathbf{k} dependency. The case where the orbitals are localized at different atoms but the potential is localized at the same atom as one of the orbitals is called a two-center integral. In the third case both orbitals and the potential are localized at different atoms, hence it is called a three-center integral. In this work three-center integrals are neglected, together with the special case of two-center integrals, where the orbitals are localized at the same atoms but the potential is at a different one. The former are significantly smaller than the two-center integrals with potential located at the same site as one of the orbitals, whereas the latter are a correction to the on-site integral [20], which can be treated as included in the definition of the on-site integrals.

The matrix elements are considered as parameters of the model, won from more sophisticated band structure calculations. The number of the two-center parameters can be lowered significantly when considering a further approximation proposed by Slater and Koster [19]. First, the orbital part of the basis functions has to be expressed in terms of cubic harmonics, orienting the orbitals along Cartesian axes. When \mathbf{R} is the vector connecting the centers of the orbitals, the integrals can be written as a linear combination of orbitals localized parallel and perpendicular to \mathbf{R} with coefficients proportional to

polynomials of direction cosines l, m, n of \mathbf{R} . The new parameters can be written in the form (ija) with $i, j = \{s, p, d, f, \dots\}$ being the orbital angular momenta and $a = \{\sigma, \pi, \delta, \dots\}$ the bond type [22]. An example for an integral of two p_x orbitals localized at different atoms gives

$$\langle p_x(\mathbf{R}) | \hat{H} | p_x(0) \rangle = l^2 (pp\sigma) + (1 - l^2) (pp\pi). \quad (3.8)$$

A full table for $i = s, p, d$ orbitals is given in [19] and in [22] for f orbitals.

3.2.3 Spin-Orbit Coupling

The Schrödinger equation, which is the basis for the TB model, does not account for relativistic effects. Since they play a very important role for TIs, the spin-orbit coupling (SOC) correction to the Schrödinger equation will be expressed in terms of the TB matrix. The derivation follows reference [23].

For simplicity, four orbitals (s, p_x, p_y, p_z) are chosen as a basis. When spin should be treated in the TB model, the basis has to be doubled. In our example we get $(s^\uparrow, p_x^\uparrow, p_y^\uparrow, p_z^\uparrow, s^\downarrow, p_x^\downarrow, p_y^\downarrow, p_z^\downarrow)$ as a new basis, where the spin eigenvalue \uparrow, \downarrow is measured against the z direction. In the new basis, the rank of the TB matrix is doubled and it acquires the form

$$\underline{\underline{H}} = \underline{\underline{H}}_{TB} + \underline{\underline{H}}_{SO} = \begin{pmatrix} \underline{\underline{H}}^{\uparrow\uparrow} & \underline{\underline{H}}^{\uparrow\downarrow} \\ \underline{\underline{H}}^{\downarrow\uparrow} & \underline{\underline{H}}^{\downarrow\downarrow} \end{pmatrix}. \quad (3.9)$$

$\underline{\underline{H}}_{TB}$ consists of two copies of the original TB matrix at the matrix diagonal:

$$\underline{\underline{H}}_{TB} = \begin{pmatrix} \underline{\underline{H}}_{TB}^\uparrow & 0 \\ 0 & \underline{\underline{H}}_{TB}^\downarrow \end{pmatrix}, \quad \underline{\underline{H}}_{TB}^\uparrow = \underline{\underline{H}}_{TB}^\downarrow. \quad (3.10)$$

The SOC part of the Hamiltonian in the on-site approximation can be written as

$$\hat{H}_{SO} = \lambda \hat{\mathbf{L}} \cdot \hat{\mathbf{S}}, \quad (3.11)$$

assuming a spherical symmetric potential. $\hat{\mathbf{L}}$ and $\hat{\mathbf{S}}$ are the angular momentum and spin operator, respectively, λ the SOC parameter. Since \hat{H}_{SO} is not diagonal in the chosen basis set, it has to be transformed in order to evaluate \hat{H}_{SO} . For this purpose the basis functions will be expressed in terms of total angular momentum states. The scalar product in equation (3.11) can be substituted by

$$\hat{\mathbf{L}} \cdot \hat{\mathbf{S}} = \frac{1}{2} (\hat{\mathbf{J}}^2 - \hat{\mathbf{L}}^2 - \hat{\mathbf{S}}^2) \quad (3.12)$$

using the total angular momentum $\hat{\mathbf{J}} = \hat{\mathbf{L}} + \hat{\mathbf{S}}$. From equation (3.12) it is obvious that the s orbitals have no SOC, since they have no angular momentum. The elements of \hat{H}_{SO} containing p orbitals are more complicated to derive. First the p orbitals will be expressed as linear combinations of spherical harmonics:

$$\begin{aligned} p_x &= \frac{1}{\sqrt{2}} [-Y_{1,1} + Y_{1,-1}], \\ p_y &= \frac{i}{\sqrt{2}} [Y_{1,1} + Y_{1,-1}], \\ p_z &= Y_{1,0}. \end{aligned} \quad (3.13)$$

The spin can be attached to spherical harmonics on the same footing as for the atomic orbitals. Therefore, we get $Y_{l,m}^\uparrow$ and $Y_{l,m}^\downarrow$ in the new basis. Since the SOC operator is diagonal in the total angular momentum representation, the aim is now to express the p orbitals in this representation. For this, the spherical harmonics are expressed as linear combinations of total angular momentum states using the Clebsch-Gordan coefficients [24]:

$$\begin{aligned}
\Phi_{\frac{3}{2},\frac{3}{2}} &= Y_{1,1}^\uparrow, \\
\Phi_{\frac{3}{2},\frac{1}{2}} &= \frac{1}{\sqrt{3}}Y_{1,1}^\downarrow + \frac{\sqrt{2}}{\sqrt{3}}Y_{1,0}^\uparrow, \\
\Phi_{\frac{3}{2},-\frac{1}{2}} &= \frac{\sqrt{2}}{\sqrt{3}}Y_{1,0}^\downarrow + \frac{1}{\sqrt{3}}Y_{1,-1}^\uparrow, \\
\Phi_{\frac{3}{2},-\frac{3}{2}} &= Y_{1,-1}^\downarrow, \\
\Phi_{\frac{1}{2},\frac{1}{2}} &= \frac{-1}{\sqrt{3}}Y_{1,0}^\uparrow + \frac{\sqrt{2}}{\sqrt{3}}Y_{1,1}^\downarrow, \\
\Phi_{\frac{1}{2},-\frac{1}{2}} &= \frac{-\sqrt{2}}{\sqrt{3}}Y_{1,-1}^\uparrow + \frac{1}{\sqrt{3}}Y_{1,0}^\downarrow.
\end{aligned} \tag{3.14}$$

Resolving equation (3.14) for the spherical harmonics and plugging them into equation (3.13) leads to

$$\begin{aligned}
p_x^\uparrow &= \frac{1}{\sqrt{2}} \left\{ -\Phi_{\frac{3}{2},\frac{3}{2}} + \frac{1}{\sqrt{3}}\Phi_{\frac{3}{2},-\frac{1}{2}} - \frac{\sqrt{2}}{\sqrt{3}}\Phi_{\frac{1}{2},-\frac{1}{2}} \right\}, \\
p_x^\downarrow &= \frac{1}{\sqrt{2}} \left\{ -\frac{1}{\sqrt{3}}\Phi_{\frac{3}{2},\frac{1}{2}} - \frac{\sqrt{2}}{\sqrt{3}}\Phi_{\frac{1}{2},\frac{1}{2}} + \Phi_{\frac{3}{2},-\frac{3}{2}} \right\}, \\
p_y^\uparrow &= \frac{i}{\sqrt{2}} \left\{ \Phi_{\frac{3}{2},\frac{3}{2}} + \frac{1}{\sqrt{3}}\Phi_{\frac{3}{2},-\frac{1}{2}} - \frac{\sqrt{2}}{\sqrt{3}}\Phi_{\frac{1}{2},-\frac{1}{2}} \right\}, \\
p_y^\downarrow &= \frac{i}{\sqrt{2}} \left\{ \frac{1}{\sqrt{3}}\Phi_{\frac{3}{2},\frac{1}{2}} + \frac{\sqrt{2}}{\sqrt{3}}\Phi_{\frac{1}{2},\frac{1}{2}} + \Phi_{\frac{3}{2},-\frac{3}{2}} \right\}, \\
p_z^\uparrow &= \frac{\sqrt{2}}{\sqrt{3}}\Phi_{\frac{3}{2},\frac{1}{2}} - \frac{1}{\sqrt{3}}\Phi_{\frac{1}{2},\frac{1}{2}}, \\
p_z^\downarrow &= \frac{\sqrt{2}}{\sqrt{3}}\Phi_{\frac{3}{2},-\frac{1}{2}} + \frac{1}{\sqrt{3}}\Phi_{\frac{1}{2},-\frac{1}{2}}.
\end{aligned} \tag{3.15}$$

In the basis of total angular momentum the eigenvalues of the spin-orbit operator have the form

$$\langle \mathbf{L} \cdot \mathbf{S} \rangle = \frac{\hbar^2}{2} \{j(j+1) - l(l+1) - s(s+1)\}. \tag{3.16}$$

Now it is straight forward to calculate the non-zero elements of the SOC part of the TB matrix:

$$\begin{aligned}
\langle p_x^\uparrow | H_{SO} | p_y^\uparrow \rangle &= \langle p_y^\uparrow | H_{SO} | p_z^\downarrow \rangle = -\langle p_x^\downarrow | H_{SO} | p_y^\downarrow \rangle = -\langle p_y^\downarrow | H_{SO} | p_z^\uparrow \rangle = -i\lambda, \\
\langle p_x^\uparrow | H_{SO} | p_z^\downarrow \rangle &= -\langle p_x^\downarrow | H_{SO} | p_z^\uparrow \rangle = \lambda.
\end{aligned} \tag{3.17}$$

The elements for a TB model including d and f orbitals in its basis set can be found in reference [25]. At this point it has to be recalled, that by this method only on-site

elements of the SOC are introduced to the TB model. SOC connecting orbitals localized at different sites is neglected here.

3.2.4 Exchange Interaction

In the last years of the 19th century, Pieter Zeeman observed a broadening of the spectral lines of different gases when put into a magnetic field [26]. Later it turned out that the broadening is in reality a splitting of the spectral lines, given by the loss of spin degeneracy when a magnetic field is turned on. It is coupled to the electrons via the magnetic moment connected to the electron spin. Therefore, the electronic states with spin oriented anti-parallel to the magnetic field are energetically favoured against the states with parallel spin orientation. Using the same description, also magnetic materials can be simulated, assigning local magnetic fields to each atom, originating from their magnetization. In TB, such behaviour can be easily described by adding an exchange or Zeeman term \hat{H}_{XC} to the TB matrix [27],

$$\hat{H}_{XC} = -\mathbf{V}_{XC} \cdot \boldsymbol{\sigma}. \quad (3.18)$$

$\boldsymbol{\sigma}$ is the vector of the Pauli matrices. In \mathbf{V}_{XC} the strength of the magnetic field or the magnetization and the value of the coupling constants are condensed. The vector can also possess different size and direction for different atoms, thus allowing also the modelling of different magnetic structures such as ferromagnets or antiferromagnets, next to the effect of a constant external magnetic field.

3.2.5 Optimization of the Slater-Koster Parameters

In the original work of Slater and Koster [19] it was proposed to fit the two-center integrals (now called Slater-Koster (SK) or TB parameters) to a measured or calculated band structure at high symmetry points in the Brillouin zone (BZ). The TB model was then meant to be used to interpolate the band structure between these points. Today, it is much easier to calculate the band structure in the whole BZ with more sophisticated methods. Therefore, the TB model is used to obtain additional information, mostly when the original structure becomes a subject to small changes. The SK parameters are commonly fitted to a density-functional theory (DFT) bulk band structure. In the TB model one can then easily calculate the effect of e.g. strain or alloying, or consider various geometries like surfaces or interfaces, which requires transferable SK parameters.

In this work, the SK parameters were fitted to a DFT band structure using the Monte Carlo method implemented in the form of the Metropolis algorithm [28], typically used to find the global minimum of a given function. Here, the input are the DFT band energies at discrete points in the BZ. The points are usually located at high symmetry lines, but this does not have to be the case in general. With a starting set of the SK parameters the TB band energies can be calculated. The mean square error of the TB energies compared to the DFT energies is the fitness function f which has to be minimized by the Monte Carlo procedure,

$$f = \frac{1}{N} \sum_{i=1}^N \sqrt{(E_{TB}(\mathbf{k}_i) - E_{DFT}(\mathbf{k}_i))^2}. \quad (3.19)$$

After calculating the starting value of f denoted by f_0 , a random SK parameter is changed by a random value chosen from a reasonable interval (mostly between -0.5 eV

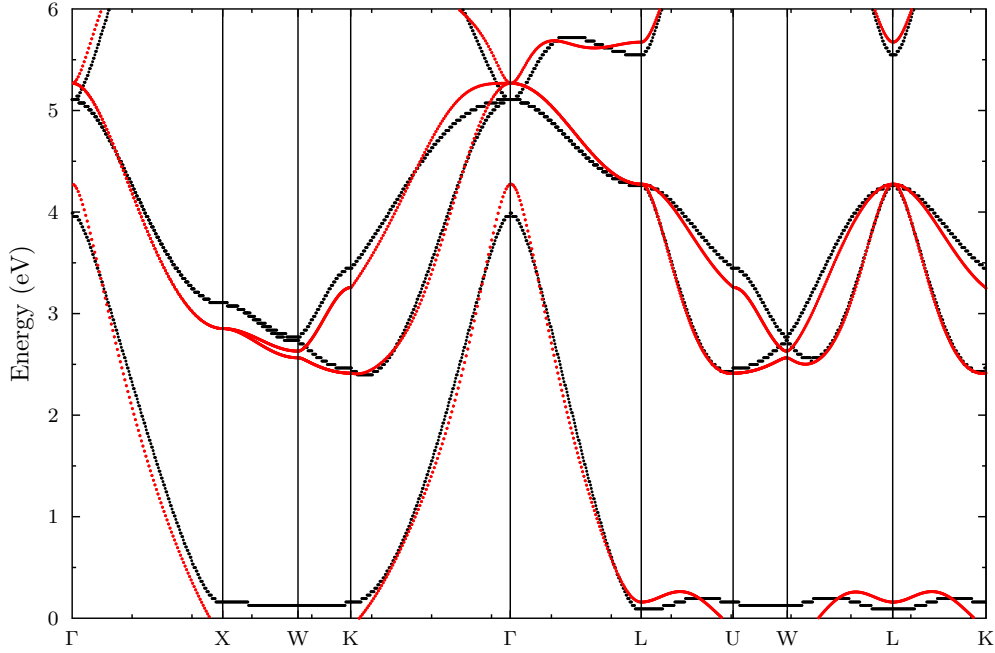


Figure 3.1: Calculated band structure of HgTe along the high symmetry lines of the BZ, without SOC. Red: TB, black: Korringa-Kohn-Rostocker DFT-based method. Figure from [TR1].

and 0.5 eV). Then, the next iteration f_1 is calculated from equation (3.19). If $f_1 < f_0$ then the new values of the SK parameters are taken for the next iteration. Otherwise it is chosen randomly whether the new or the old set of SK parameters is kept, with the probability for keeping the new values being

$$p = e^{-\frac{f_1 - f_0}{\kappa}}. \quad (3.20)$$

κ is a parameter controlling the acceptance probability. In a Monte Carlo calculation minimizing the energy of a system, f would be the energy and $\kappa = k_B T$ the virtual temperature.

This procedure is repeated, until a satisfying value of the error f is achieved. In the beginning κ takes on higher values, which increases the probability of taking SK parameters which are worse than the previous iteration, thus avoiding getting trapped near local minima of f . κ is decreased with higher iteration count, ensuring that the system stays near a global minimum. The proper values of the parameters have to be chosen carefully, depending on many properties of the system such as the number of atoms, SK parameters, quality of the initial values, etc. Usually, 8000 iterations are needed to get a good set of SK parameters.

When SOC is considered, which is always the case for topological materials, it proved to be useful to first do the fitting procedure neglecting SOC in both TB and DFT calculations. In a second step, the values of the SOC parameters are chosen in order to reproduce the splitting of degenerate bands at some high symmetry points of the BZ (mostly Γ). Figure 3.1 shows the result of the optimization for HgTe as an example.

At this point it has to be stated, that in general the valence bands are modelled much better than the conduction bands in TB, owing to the choice of the basis set. The “tightly bound” atomic orbitals can reproduce the energetically lower valence bands very well, but the accuracy in modelling the unoccupied states is much worse. This is discussed e.g., in reference [29]. The authors add an excited atomic s^* state to the basis set in order to get better results also for the conduction bands. Considering more neighbours or orbitals with higher angular momentum can also improve the results, as shown in the references [30, 31]. Klimeck *et al.* [30] also used a genetic algorithm as an alternative to the Monte Carlo algorithm to get the SK parameters. A completely different basis set used widely in the context of topological materials are the maximally localized Wannier functions (MLWFs) [32], because some of the topological invariants can be calculated in a more straightforward way by this approach.

3.2.6 Strain

Having established all the parameters of the TB model using a DFT based calculation, it is possible to use the model for making predictions for special cases differing slightly from the original one. A possible alteration of the system is the application of strain in different directions, which may in reality come from a substrate or from ambient pressure. In this work, the influence of strain on the electronic structure was modelled by the Harrison d^{-2} rule [29, 33]. This predicts for the SK parameters ($ij\alpha$) to depend on distance as follows:

$$(ij\alpha)_{\text{strained}} = \left(\frac{d_{\text{unstrained}}}{d_{\text{strained}}} \right)^2 (ij\alpha)_{\text{unstrained}}. \quad (3.21)$$

d_{strained} and $d_{\text{unstrained}}$ are the inter-atomic distances in the strained and unstrained case, respectively. Equation (3.21) shows the expected behaviour of the SK parameters – originally integrals – which become smaller with increasing distance between the overlapping orbitals. A more complicated dependence of the SK parameters on the inter-atomic distance d is assumed by Papaconstantopoulos and Mehl [20],

$$(ij\alpha) = (e_{ij\alpha} + f_{ij\alpha}d + g_{ij\alpha}d^2) \exp\left(-h_{ij\alpha}^2 d\right) F(d). \quad (3.22)$$

$F(d)$ is a cut-off function and e , f , g and h are the fitting parameters. The number of fitting parameters is four times higher compared with the original set of SK parameters, making the optimization procedure much more demanding. The advantage of this approach is the high transferability of the parameters, which can be used for geometries with different inter-atomic distances once calculated.

3.2.7 Alloys

Another possibility of a variation of the original system which can be studied by the TB model is a substitutional alloy. One way to model a binary alloy would be a supercell which can be repeated periodically [34]. When large enough, the disorder in the alloy can be described sufficiently. In addition, different local environments of the different atoms can be simulated, including the short-range order [35]. A critical aspect is that the calculation becomes expensive because of the large number of atoms in the supercell leading to large TB matrices. Furthermore, the concentration of the binary alloy can be varied only in discrete steps.

Another way of simulating disordered systems is to define some kind of a lattice-periodic virtual potential effectively describing the system. The lattice periodicity is restored in the model, but the key difficulty is transferred to the estimation of the effective potential. In this work the virtual-crystal approximation (VCA) and the coherent-potential approximation (CPA) are used, owing to its low computational cost for the former and reliable results for the latter. In both approximations only the effect of the impurities on the potential can be simulated, not the lattice deformation around single impurities. This would be possible in the supercell approach.

3.2.7.1 Virtual Crystal Approximation

In the VCA approach [36, 37] it is assumed that the potential of the alloy is given as a combination of the potentials of the pure compounds. Mostly, a linear scaling of the potential with the concentration is assumed. When the concentration of compound A and B is x and $1 - x$ respectively, then the potential of A_xB_{1-x} is given as

$$V_{VCA} = xV_A + (1 - x)V_B. \quad (3.23)$$

This transfers to the TB model via the same linear dependence of all parameters, i.e. SK, SOC and exchange parameters, on the concentration. The biggest advantage of this treatment is the possibility to calculate the eigenenergies and eigenvectors, which can be used for further calculations of e.g., topological invariants. VCA works well when both compounds possess similar band structures and the SK parameters do not differ strongly. If the band structures of the pure compounds are qualitatively different, then the result of a linear interpolation between them can give questionable results, as is for example the case in CuNi [38], even though Cu and Ni are neighbours in the periodic table.

3.2.7.2 Coherent Potential Approximation

An improvement to the VCA is the CPA, introduced by Soven [39] for electronic systems. Some applications and a description of the CPA in terms of Green functions can be found in the references [40–43]. In the CPA, the substitutional alloy is treated as an effective periodic medium surrounding the site where one of the original atoms is placed. The potential of the medium can be estimated by exploiting the condition of vanishing scattering from the original atom (treated as an impurity in the medium) averaged by the composition. In this work, only the diagonal disorder was treated within the CPA. The off-diagonal k dependent part of the TB matrix was estimated using the VCA. A possibility to include also off-diagonal disorder in the CPA is described in reference [44].

The derivation of the CPA in the single-site approximation – as used in this work – follows reference [41]. The hat sign marking operators will be omitted in this section for simplicity. Assuming a disordered crystal A_xB_{1-x} with atom A located at each lattice site with the probability $x \in [0 : 1]$ and atom B with probability $1 - x$, the Hamiltonian describing the crystal has the form

$$H = H_0 + V = H_0 + \sum_n V_n \quad (3.24)$$

with V_n is $V_A(V_B)$ for the atom A(B) located at the site n . H_0 is the off-diagonal periodic part of the Hamiltonian and V represents the diagonal random part. The resolvent of the Hamiltonian H is

$$G(z) = (z - H)^{-1}. \quad (3.25)$$

$z = E + i\eta$ is a complex energy. The ensemble average of G defines the energy dependent self-energy Σ which describes an effective medium with restored lattice periodicity:

$$\langle G(z) \rangle = \langle (z - H)^{-1} \rangle \equiv [z - H_0 - \Sigma(z)]^{-1}. \quad (3.26)$$

In the next step H can be re-written by adding and subtracting an energy-dependent periodic potential $\tilde{V}(z) = \sum_n \tilde{V}_n(z)$:

$$\begin{aligned} H &= [H_0 + \tilde{V}(z)] + \sum_n V_n - \tilde{V}_n(z) \\ &= \tilde{H}(z) + V'(z). \end{aligned} \quad (3.27)$$

$\tilde{V}(z)$ will be an initial approximation to the self-energy Σ . $V'(z) = \sum_n V_n - \tilde{V}_n(z) = \sum_n v_n(z)$ describes the scattering off the real atoms A and B embedded within the effective medium, which now acts as a reference. The resolvent of the effective medium is

$$\tilde{G}(z) = (z - \tilde{H})^{-1} \quad (3.28)$$

and is connected to the resolvent of the original disordered system via the Dyson equation (with the z dependence omitted for simplicity)

$$G = \tilde{G} + \tilde{G}V'G = \tilde{G} + \tilde{G}T\tilde{G}. \quad (3.29)$$

T is the scattering operator given by

$$T = V' + V'\tilde{G}T = \sum_n v_n + \sum_n v_n \tilde{G} \sum_m v_m + \dots \quad (3.30)$$

Decomposing T into the sum of contributions from the individual sites

$$T = \sum_n T_n \quad (3.31)$$

leads to

$$T_n = v_n [1 + \tilde{G}T] = t_n \left[1 + \tilde{G} \sum_{m \neq n} T_m \right]. \quad (3.32)$$

t_n is a single-site scattering operator taking on values t_n^A or t_n^B when the atom A or B is located at the site n . It can be written as

$$t_n = v_n + v_n \tilde{G} v_n + \dots = [1 - v_n \tilde{G}]^{-1} v_n = v_n + v_n \tilde{G} t_n \quad (3.33)$$

and seen as a part of equation (3.30) which gives only the pure contribution of the site n to the total scattering operator T . Iterating equation (3.32) leads to a series for the total scattering operator in terms of the single-site contributions

$$T = \sum_n t_n + \sum_n t_n \tilde{G} \sum_{m \neq n} t_m + \dots \quad (3.34)$$

From averaging equation (3.29) it follows that

$$\langle G \rangle = \tilde{G} + \tilde{G} \langle T \rangle \tilde{G}, \quad (3.35)$$

thus introducing the ensemble-averaged total scattering operator. Using Eqs. (3.26) and (3.35) it is possible to derive the following formula for the self-energy,

$$\Sigma = z - H_0 - \langle G \rangle^{-1} = \tilde{V} + \langle T \rangle (1 + \tilde{G} \langle T \rangle)^{-1}. \quad (3.36)$$

The self-energy is therefore given as the initial periodic potential \tilde{V} – which can be seen as a first approximation to the self-energy – plus the effect of the averaged scattering relative to the effective potential \tilde{V} .

At this point, the CPA is introduced by claiming that the scattering has to vanish on average,

$$\langle T \rangle = 0, \quad (3.37)$$

which is equivalent to the equality of the averaged Green function of the disordered medium $\langle G \rangle$ and the Green function of the effective medium \tilde{G} . By this requirement, we get a set of coupled equations, which can be solved for Σ self-consistently.

Thus, the problem of calculating the averaged total scattering operator to evaluate equation (3.36) remains. Averaging equation (3.31) leads to

$$\langle T \rangle = \sum_n \langle T_n \rangle \quad (3.38)$$

$\langle T_n \rangle$ can be calculated from equation (3.32) by rearranging the formula for the covariance of two random variables a and b [45], $\langle ab \rangle = \langle a \rangle \langle b \rangle + \langle (a - \langle a \rangle) (b - \langle b \rangle) \rangle$:

$$\langle T_n \rangle = \langle t_n \rangle \left[1 + \tilde{G} \sum_{m \neq n} \langle T_m \rangle \right] + \left\langle (t_n - \langle t_n \rangle) \tilde{G} \sum_{m \neq n} (T_m - \langle T_m \rangle) \right\rangle \quad (3.39)$$

with the average scattering operator $\langle t_n \rangle$ connected to the site n being

$$\langle t_n \rangle = x t_n^A + (1 - x) t_n^B. \quad (3.40)$$

In the next step, the second fluctuation-like term in the right-hand side of equation (3.39) will be neglected, which is called the single-site approximation. Combined with the equality

$$\sum_{m \neq n} \langle T_m \rangle = \langle T \rangle - \langle T_n \rangle \quad (3.41)$$

it leads to

$$\langle T_n \rangle = [1 + \langle t_n \rangle \tilde{G}]^{-1} \langle t_n \rangle [1 + \tilde{G} \langle T \rangle]. \quad (3.42)$$

Eqs. (3.36) and (3.38) allow to re-write the self-energy Σ as a sum of site-dependent terms,

$$\Sigma = \sum_n \tilde{V}_n + [1 + \langle t_n \rangle \tilde{G}]^{-1} \langle t_n \rangle, \quad (3.43)$$

which is the final equation of the CPA in the single-site approximation. The CPA condition becomes $\langle t_n \rangle = 0$ for all sites n . By exploiting the periodicity of the reference medium, it is sufficient to do the calculation only at one site, e.g., $n = 0$, which is a significant simplification of the problem.

In the TB approach the Hamiltonian H becomes the TB matrix and \tilde{G} the Green function of the reference medium, respectively. The CPA equations can be solved self-consistently by choosing the VCA as an initial approximation to the potential \tilde{V}_n . By iteration, a vanishing scattering matrix is achieved and the Green function \tilde{G} of the reference medium can be calculated. The effect of the complex self-energy describing the reference medium is both a shift of the electronic energies and life-time broadening of the states. Since the CPA is a Green function approach, the electronic band structure has to be calculated via the spectral density

$$N(E, \mathbf{k}) = -\frac{1}{\pi} \Im \text{Tr} \tilde{G}(E + i\eta, \mathbf{k}). \quad (3.44)$$

Usually the CPA gives better results than the VCA, but the main disadvantage of CPA in this work is the unavailability of eigenfunctions, which are crucial for calculating the topological invariants. Therefore, both methods are used dependent on the context, the former for a detailed electronic band structure and the latter to get topological invariants of disordered systems.

3.2.8 Semi-Infinite Crystals and their Interfaces

To calculate the surface electronic structure a renormalization scheme for semi-infinite crystals was used [46]. In this procedure, the crystal is formed by atomic layers ordered parallel to the surface. Since atoms from one atomic layer are assumed to interact only with atoms from a finite number of neighbouring layers, so-called principal layers are constructed from the atomic layers in a way that one principal layer interacts only with the adjacent principal layers. The equation defining the Green function

$$(z - \hat{H}) \hat{G} = \hat{1} \quad (3.45)$$

can then be written in a matrix representation

$$\begin{pmatrix} A^s & -B^s & 0 & 0 & \dots \\ -B^{s\dagger} & A & -B & 0 & \dots \\ 0 & -B^\dagger & A & -B & \dots \\ 0 & 0 & -B^\dagger & A & \dots \\ \vdots & \vdots & \vdots & \vdots & \ddots \end{pmatrix} \cdot \begin{pmatrix} G_{00} & G_{01} & G_{02} & G_{03} & \dots \\ G_{10} & G_{11} & G_{12} & G_{13} & \dots \\ G_{20} & G_{21} & G_{22} & G_{23} & \dots \\ G_{30} & G_{31} & G_{32} & G_{33} & \dots \\ \vdots & \vdots & \vdots & \vdots & \ddots \end{pmatrix} = \begin{pmatrix} 1 & 0 & 0 & 0 & \dots \\ 0 & 1 & 0 & 0 & \dots \\ 0 & 0 & 1 & 0 & \dots \\ 0 & 0 & 0 & 1 & \dots \\ \vdots & \vdots & \vdots & \vdots & \ddots \end{pmatrix}, \quad (3.46)$$

with the abbreviations

$$A^s = z - H_{00}^s \quad (3.47)$$

$$B^s = H_{01}^s \quad (3.48)$$

$$B^{s\dagger} = H_{01}^{s\dagger} \quad (3.49)$$

$$A = z - H_{11} \quad (3.50)$$

$$B = H_{01} \quad (3.51)$$

$$B^\dagger = H_{01}^\dagger. \quad (3.52)$$

The principal-layer index is a multi-index combining the atomic layer, atom type and orbital.

Equation (3.46) cannot be solved by simple inversion, because the dimension of the matrices is infinite, owing to the semi-infinite geometry. Instead, many equations for the block matrices can be extracted, e.g.,

$$A^s = 1 + B^s G_{10} \quad (3.53)$$

$$A G_{10} = B^{s\dagger} G_{00} + B G_{20}. \quad (3.54)$$

Combining these two equations leads to

$$\left(A^s - B^s A^{-1} B^{s\dagger} \right) G_{00} = 1 + B^s A^{-1} B G_{20}. \quad (3.55)$$

By defining

$$E_1^s = A^s - B^s A^{-1} B^{s\dagger} \quad (3.56)$$

$$A_1^s = B^s A^{-1} B \quad (3.57)$$

equation (3.55) becomes

$$E_1^s G_{00} = 1 + A_1^s G_{20} \quad (3.58)$$

which possesses the same structure as equation (3.53). New in equation (3.58) is the fact, that the zeroth (surface) principal layer is now coupled to the second bulk principal layer with a decreased interaction. By the same procedure, similar renormalization can be found for equations containing block matrices of the bulk layers. By iteration, the effective inter-layer interaction A_1, A_1^s becomes small and vanishes for an infinite number of iterations. The Green function of the surface principal layer is then given as

$$G_{00} = (E_i^s)^{-1} \quad (3.59)$$

assuming that the interaction is sufficiently small after the i -th iteration. In a similar way the Green function of a bulk principal layer G_{nn} for $n \rightarrow \infty$ can be calculated. Other blocks can be obtained by applying suitable transfer matrices to already known blocks.

Having constructed the whole Green function $G_{lm}(E, \mathbf{k}_{\parallel})$, the surface electronic structure can be obtained as the spectral density same as in section 3.2.7.2:

$$N_0(E, \mathbf{k}) = -\frac{1}{\pi} \Im \text{Tr} G_{00}(E + i\eta, \mathbf{k}). \quad (3.60)$$

By the same procedure also an interface of two different materials can be simulated. There is a similar renormalization scheme for the interface of two layered materials, each occupying one semi-infinite half-space [47]. The spectral density is again calculated from the Green function as in equation (3.44).

Another possibility to calculate the electronic structure of a crystal surface of a layered material would be a slab. Because of the finite dimension of the TB matrix, the energy eigenvalues can be calculated as for a bulk system. The main disadvantage of this treatment is the non-vanishing interaction between both slab surfaces, which manifests itself in artificial gaps, which can be mostly observed in surface states. Since these finite-size effects could influence the results of this work, the semi-infinite approach was chosen for most of the surface and interface calculations.

3.2.9 Berry Curvature in the Tight-Binding Model

After addressing all common aspects of the TB model, the problem of calculating the Berry curvature will be discussed. We will follow the derivation of Gradhand *et al.* [48].

The first problem is that the Berry curvature is defined for the lattice periodic part of the Bloch wave functions $u_{n,k}(\mathbf{r})$, whereas the result of TB calculations are the full wave functions $\psi_{n,k}(\mathbf{r})$. The connection between the two is given by the Bloch theorem

$$\psi_{n,k}(\mathbf{r}) = e^{i\mathbf{k}\mathbf{r}} u_{n,k}(\mathbf{r}). \quad (3.61)$$

By plugging equation (3.61) into the definition of the Berry connection, equation (2.23), we get two terms:

$$\begin{aligned} A_n(\mathbf{k}) &= i \int_{EZ} d^3r u_{n,k}^*(\mathbf{r}) \nabla_{\mathbf{k}} u_{n,k}(\mathbf{r}) \\ &= i \int_{EZ} d^3r \psi_{n,k}^*(\mathbf{r}) e^{i\mathbf{k}\mathbf{r}} \nabla_{\mathbf{k}} \left[e^{-i\mathbf{k}\mathbf{r}} \psi_{n,k}(\mathbf{r}) \right] \\ &= \int_{EZ} d^3r \psi_{n,k}^*(\mathbf{r}) \mathbf{r} \psi_{n,k}(\mathbf{r}) + i \int_{EZ} d^3r \psi_{n,k}^*(\mathbf{r}) \nabla_{\mathbf{k}} \psi_{n,k}(\mathbf{r}). \end{aligned} \quad (3.62)$$

The first one is called the dipole contribution and the second one gradient contribution. Since we have no knowledge about the spatial distribution of $\psi_{n,k}^*(\mathbf{r})$ the dipole contribution cannot be calculated in the TB approach. The term will be neglected in all calculations, since it is approximately one order of magnitude smaller than the gradient contribution [49].

The gradient contribution of the Berry curvature is given as the curl of the connection, i.e.

$$\boldsymbol{\Omega}_n(\mathbf{k}) = i \int_{EZ} d^3r \nabla_{\mathbf{k}} \psi_{n,k}^*(\mathbf{r}) \times \nabla_{\mathbf{k}} \psi_{n,k}(\mathbf{r}). \quad (3.63)$$

In the TB model this becomes

$$\begin{aligned} \boldsymbol{\Omega}_n(\mathbf{k}) = \frac{i}{N} \sum_{\mathbf{R}_i} \sum_{\alpha} [& -i\mathbf{R}_i \times (\nabla_{\mathbf{k}} c_{n,\alpha}(\mathbf{k})) c_{n,\alpha}^*(\mathbf{k}) - \\ & -i\mathbf{R}_i \times (\nabla_{\mathbf{k}} c_{n,\alpha}^*(\mathbf{k})) c_{n,\alpha}(\mathbf{k}) + (\nabla_{\mathbf{k}} c_{n,\alpha}^*(\mathbf{k})) \times (\nabla_{\mathbf{k}} c_{n,\alpha}(\mathbf{k}))]. \end{aligned}$$

The first two terms vanish since

$$\begin{aligned} \sum_{\alpha} (\nabla_{\mathbf{k}} c_{n,\alpha}(\mathbf{k})) c_{n,\alpha}^*(\mathbf{k}) &= \nabla_{\mathbf{k}} \sum_{\alpha} |c_{n,\alpha}(\mathbf{k})|^2 - \sum_{\alpha} c_{n,\alpha}(\mathbf{k}) (\nabla_{\mathbf{k}} c_{n,\alpha}^*(\mathbf{k})) \\ &= - \sum_{\alpha} c_{n,\alpha}(\mathbf{k}) (\nabla_{\mathbf{k}} c_{n,\alpha}^*(\mathbf{k})). \end{aligned}$$

The final expression for the Berry curvature in TB is

$$\boldsymbol{\Omega}_n(\mathbf{k}) = i \nabla_{\mathbf{k}} \underline{c}_n^\dagger(\mathbf{k}) \times \nabla_{\mathbf{k}} \underline{c}_n(\mathbf{k}). \quad (3.64)$$

Using a similar equality as in equation (2.11),

$$\underline{c}_m^\dagger(\nabla_{\mathbf{k}} \underline{c}_n) = \frac{\underline{c}_m^\dagger(\nabla_{\mathbf{k}} \underline{H}) \underline{c}_n}{E_n - E_m}, \quad (3.65)$$

we obtain

$$\boldsymbol{\Omega}_n(\mathbf{k}) = i \sum_{m \neq n} \frac{\underline{c}_n^\dagger(\mathbf{k}) (\nabla_{\mathbf{k}} \underline{H}(\mathbf{k})) \underline{c}_m(\mathbf{k}) \times \underline{c}_m^\dagger(\mathbf{k}) (\nabla_{\mathbf{k}} \underline{H}(\mathbf{k})) \underline{c}_n(\mathbf{k})}{(E_n - E_m)^2}. \quad (3.66)$$

It is straightforward to evaluate this formula, since the expansion coefficients $\underline{c}_n(\mathbf{k})$ and energies $E_n(\mathbf{k})$ are the results of the diagonalization of the TB matrix $\underline{H}(\mathbf{k})$ and the gradient of the TB matrix can be calculated analytically from equation (3.6):

$$\nabla H_{\alpha,\beta}(\mathbf{k}) = -i \sum_{\mathbf{R}_j} \mathbf{R}_j e^{-i\mathbf{k}\mathbf{R}_j} \langle \phi_{\sigma'}(\mathbf{r} - \mathbf{R}_j - \mathbf{t}_m) | H | \phi_{\sigma}(\mathbf{r} - \mathbf{t}_l) \rangle. \quad (3.67)$$

3.2.10 Conclusion

In this chapter, a TB model for the electronic properties of periodic crystals was introduced. It is based on a set of non-overlapping atomic orbitals. The TB parameters can be obtained from fitting the TB band structure to a DFT band structure. It is possible to calculate the electronic properties for different geometries, including semi-infinite crystals having an interface to vacuum or an interface between two semi-infinite crystals. The properties of systems with substitutional disorder can be modelled using the VCA or CPA.

On top of this, the model also allows to obtain the quantities connected to the topological character of the electronic states. The key quantity which can be computed is the Berry curvature, whose integrals over closed surfaces (mostly the BZ) are topological invariants characterizing the different topological phases.

All this information can be calculated together in the present version of the TB model and therefore it is well suited for exploring topological materials. Different types of these systems will be introduced in the next chapter.

After discussing features which recommend the TB model to be chosen in the present work, also the shortcomings of the model should be discussed. Approximations and problems connected to the basic TB model are mentioned in the first place.

Since TB is based on a single-particle approximation, correlation effects are neglected. This can lead to inaccuracies when calculating the properties of heavier elements, yet it is possible to account for these effects by adding correction terms to the on-site matrix elements as was done for example in [50].

The assumption of a finite localized orthogonal basis set, the two-center approximation and a finite number of interacting neighbours determine the quality of description of the electronic properties. The occupied bands are typically reproduced very well by the model, but it fails when considering excited states. The quality of the model can be increased by considering a non-orthogonal basis set which increases the number of parameters, by introducing additional excited orbitals to the basis set, typically an s^* orbital, or by increasing the number of neighbours considered, which significantly increases both the number of parameters and the computational effort.

After mentioning the basic problems which arise when using the TB model, in the following, the approximations introduced during the application of the model to special systems and the emerging inaccuracies will be discussed.

First of all, when considering geometries different to the infinite-bulk geometry, always the bulk SK parameters were used and no relaxation of the lattice was assumed. This is indeed a crucial approximation, which can lead for example to a badly described surface electronic structure. Therefore, especially in the case of surfaces and interfaces, mainly qualitative results can be achieved. Improvements would be accomplished by distance dependent SK parameters and by lattice relaxation calculations prior to the electronic structure calculation. However, the computational effort would then increase rapidly and it would probably be better to turn completely to a DFT-based model. A further improvement would be the self-consistent calculation of the interface charge [51] to reach charge neutrality. In this way the surface states can be for example shifted in energy towards the experimental values.

The problems of simulating strain and structural disorder were already discussed in sections 3.2.6 and 3.2.7. It should be stated here that both aspects could be described better by using distance-dependent SK parameters in combination with lattice relaxation, as was also the case for the different geometries discussed earlier.

The last source of possible problems is the procedure of parameters fitting. Since the original DFT band structure is not reproduced exactly by the TB model, it is conceivable that some properties of the fitted bands, for example the band inversion in TIs, are not described correctly. These properties have to be checked carefully before using the parameters for further calculations.

Finally, the issue of integrating quantities dependent on the TB-calculated wave function and energies should be addressed. In order to calculate e.g., the averaged Green function within the CPA scheme or the Chern number of a Weyl semimetal (WSM) (see

section 5.3), a numerical integration on a k mesh in the BZ has to be performed. Mostly, the Gaussian quadrature rule [52] with 24 k points for each dimension of the integration area is used. In the case of the topological invariants (which are integers by definition), the error is typically less than 10^{-4} .

CLASSES OF TOPOLOGICAL INSULATORS

4.1 INTRODUCTION

In solid state physics, topological insulators (TIs) are a recent hot topic. There is much effort put into understanding the underlying principles of TIs, describing the key properties, finding the criteria to distinguish between topologically trivial and non-trivial insulators and finally proposing and confirming real materials with non-trivial properties, using both theoretical and experimental techniques. In the past 35 years, many topological phases have been discovered in crystalline systems and even more are yet to be found. In the next chapter the different topological phases will be presented time-ordered. For detailed information see e.g., the references [53–56].

4.2 INTEGER QUANTUM HALL EFFECT

The whole field of TIs was opened by the discovery of the QHE by von Klitzing, Dorda and Pepper [1] in 1980. The authors found experimentally, that for a 2D electron gas in a strong perpendicular magnetic field, the longitudinal conductivity vanishes for some values of the magnetic field and simultaneously the perpendicular Hall conductivity becomes quantized as $\nu e^2/h$, ν being an integer.

The first theoretical explanation for the effect was given by Laughlin [2]. Free electrons in a uniform magnetic field have quantized energy levels, called Landau levels, which are highly degenerate. When the Fermi energy lies between two Landau levels, then the number of completely filled Landau levels ν is the filling factor. It turns out that ν is a topological invariant, in the context of TIs called the Chern number or TKNN invariant (after Thouless, Kohmoto, Nightingale and den Nijs). In their work [3] Thouless *et al.* show that ν is the number of conductivity quanta e^2/h carried by the edge state of the QHE system and that it can be calculated as an integral of the Berry curvature, see section 4.3.

The fact that the Hall conductivity in the QHE is due to surface states can be seen from a semi-classical perspective. Inside the material, the electrons propagate on closed circles, owing to the Lorentz force [57]. Electrons located near the probe boundary bounce back from it during their cyclotron motion and therefore propagate along the boundary as a 1D edge channel. There is one edge channel with a conductivity of e^2/h , also called skipping-orbit, for each occupied Landau level. Such a relationship between the value of the bulk topological invariant and the number of edge states is called bulk-boundary correspondence [53].

4.3 CHERN INSULATORS

An external magnetic field is often necessary to realize the integer QHE. The first theoretical proposal of a QHE realization without any external magnetic field was given by Haldane in 1988 [58]. Haldane constructed a TB model of a 2D hexagonal lattice with two different atomic species. The net magnetic field vanishes, but there is a periodic time-reversal symmetry (TRS) breaking magnetic flux perpendicular to the lattice, which manifests itself in complex-valued next-nearest neighbours hopping elements. Depending on the model parameters, the topological invariant – the Chern number – can take values of 0 and ± 1 . Therefore, the Haldane model is a true TI in the modern sense.

Even though Chern insulators are the first discovered type of TIs, realistic systems were proposed theoretically in recent years [59–62] in magnetically doped 2D TI systems. The first experimental realization of a Chern insulator succeeded in 2013 in magnetically doped thin $(\text{Bi,Sb})_2\text{Te}_3$ layers. The Hall conductivity was measured to be e^2/h , exactly as in the case of the QHE, but without any external magnetic field [63].

Chern Number and Surface States

The Chern number is an integer-valued topological invariant which characterizes 2D TIs with broken TRS. Assuming a 2D system with a BZ in the k_x - k_y plane, the Chern number can be calculated as the integral of the z -component of the Berry curvature $\Omega_n^z(\mathbf{k})$ with the area of integration being the whole BZ:

$$c_n = \frac{1}{2\pi} \int_{\text{BZ}} d^2k \Omega_n^z. \quad (4.1)$$

Equation (4.1) gives the Chern number of the n -th band, which is assumed to be isolated from other bands in this expression.

The calculation of Kohmoto [64] shows that the Chern number has to be integer-valued. Plugging the definition of the Berry curvature, equation (2.9), into equation (4.1), we get

$$c_n = \frac{1}{2\pi} \int_{\text{BZ}} d^2k [\nabla_{\mathbf{k}} \times \mathbf{A}_n(\mathbf{k})]_z \quad (4.2)$$

with $\mathbf{A}_n(\mathbf{k})$ being the Berry connection. Using the fact that owing to its periodicity the 2D BZ has the same geometry as a torus, which does not have any boundary, $c_n = 0$ when the Berry connection is unique and smooth in the whole BZ. Therefore, the system can be topologically non-trivial only when the periodic part of the Bloch functions $u_{n,\mathbf{k}}$ cannot be defined smoothly and uniquely in the whole BZ.

For the further calculation the BZ can be divided into two parts H_I and H_{II} with an interface ∂H . For H_I an $U(1)$ gauge to the wave functions $u_{n,\mathbf{k}}^I$ is chosen such that they become unique and smooth on H_I . A different gauge is chosen on H_{II} , after which $u_{n,\mathbf{k}}^{II}$ is unique and smooth in this region. Therefore, there is a phase mismatch at ∂H ,

$$u_{n,\mathbf{k}}^{II} = e^{i\chi(\mathbf{k})} u_{n,\mathbf{k}}^I, \quad (4.3)$$

with a continuous $\chi(\mathbf{k})$. For the gauge-dependent Berry connection at $\mathbf{k} \in \partial H$ we get:

$$\mathbf{A}_n^{II}(\mathbf{k}) = \mathbf{A}_n^I(\mathbf{k}) - \nabla_{\mathbf{k}} \chi(\mathbf{k}). \quad (4.4)$$

Applying Stokes' theorem in both parts of the BZ yields

$$c_n = \frac{1}{2\pi} \int_{\partial H} d\mathbf{k} [\mathbf{A}_n^I(\mathbf{k}) - \mathbf{A}_n^{II}(\mathbf{k})] = \frac{1}{2\pi} \Delta\chi. \quad (4.5)$$

$\Delta\chi$ is the phase change gathered along ∂H . Since $u_{n,k}^{I/II}$ was chosen uniquely, the phase change can only be

$$\Delta\chi = 2\pi n, \quad n \in \mathbb{Z}. \quad (4.6)$$

The Chern number of an isolated band is therefore always an integer. The total Chern number of an insulator is calculated as [65]

$$C = \sum_n c_n. \quad (4.7)$$

The sum in equation (4.7) is over all bands below the Fermi energy, which is located in the band gap in the case of an insulator. The total Chern number can also be calculated using the non-Abelian Berry curvature \mathcal{F} [66] containing the adiabatic properties of all occupied bands:

$$C = \frac{1}{2\pi} \int_{\text{BZ}} [\text{Tr}[\mathcal{F}(\mathbf{k})]]_z d^2k. \quad (4.8)$$

At this point it is worth noting the effect of TRS on the Chern number. The effect on the Berry curvature is [67]

$$\Omega_n(\mathbf{k}) = -\Omega_n(-\mathbf{k}). \quad (4.9)$$

Since the Chern number is given as a BZ integral over the Berry curvature, the contributions at the wave vectors \mathbf{k} and $-\mathbf{k}$ cancel each other, resulting in a vanishing Chern number. Therefore, to realize a non-zero Chern insulator, TRS has to be broken, for example by an external magnetic field or by a magnetization.

Exactly as in the QHE case, the number of surface states in Chern insulators is given by the Chern number, which is the bulk-boundary correspondence [53]. A mathematical proof was given by Hatsugai in 1993 [68]. For the Haldane model, this correspondence was demonstrated by Thonhauser and Vanderbilt who investigated the surface electronic structure of the model [69]. A typical dispersion of a surface state emerging in Chern insulators is shown in Fig. 4.1.

4.4 2D TIME-REVERSAL INVARIANT TOPOLOGICAL INSULATORS

Similar to the QHE, being the quantized equivalent of the Hall effect, the quantum spin Hall effect (QSHE) is the quantized equivalent of the spin Hall effect (SHE). In the SHE, the electrons with opposite spin orientations are deflected in opposite directions due to the SOC which works as a \mathbf{k} and spin dependent effective magnetic field [70], similar to the Mott scattering [71]. The Hall voltage is zero, but there is a finite spin Hall conductivity. This quantity cannot be measured directly but via the inverse SHE [72]. In the topological quantized variant of the SHE, the transverse spin conductivity is quantized and robust against impurities.

Time-reversal invariant TIs or TIs of the QSHE type in 2D were first proposed by Kane and Mele in 2005 [73]. They investigated the basic properties in a TB model of a honeycomb lattice with SOC. The Kane-Mele model can be seen as two copies of the Haldane model, one copy for each spin orientation. The SOC then acts as an effective magnetic field with opposite sign for both spin orientations. The first real system proposed in the same year was graphene, yet it turned out the spin-orbit induced energy gap is too small, approximately $25 \mu\text{eV}$ for room temperature applications [74]. In 2006 a layered system of HgTe quantum wells between CdTe layers was proposed as a suitable system for an experimental realization [75] and it was confirmed one year later by König *et al.* [76].

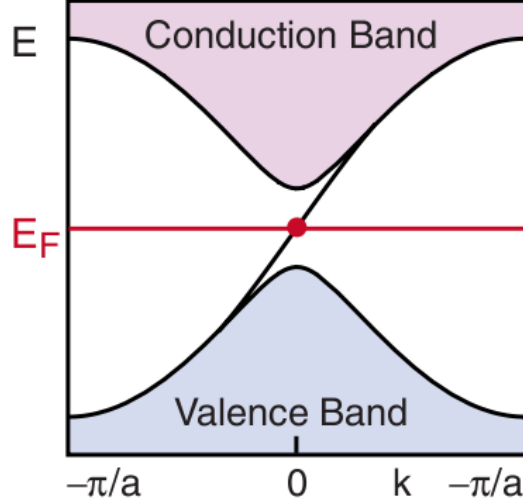


Figure 4.1: Surface BZ of the 1D edge of a Chern insulator featuring one surface state connecting the valence bands with the conduction bands, from [53]. According to the bulk-boundary correspondence, the Chern number of the occupied bulk bands must be $C = 1$.

\mathcal{Z}_2 Invariant

Kane and Mele also settled the \mathcal{Z}_2 invariant ν as the characteristic topological invariant for the 2D TIs of the QSHE type [73]. It can be calculated from the eigenfunctions of the occupied bands, when TRS is present in the system. The only possible values of ν are 0 and 1. If $\nu = 0$, the system is trivial and it is non-trivial for $\nu = 1$.

The \mathcal{Z}_2 invariant characterizes 2D TIs with TRS. This condition is crucial, the invariant cannot be defined when TRS is broken. After the first definition of the \mathcal{Z}_2 invariant [73], many alternative ways of calculating it in real systems were proposed [77–81].

The equation most frequently used to define the invariant was introduced by Fu and Kane [77]:

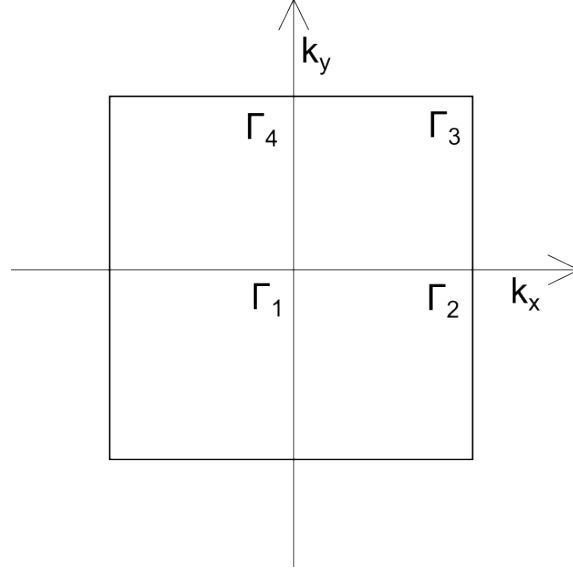
$$(-1)^\nu = \prod_{i=1}^4 \frac{\sqrt{\det[w(\Gamma_i)]}}{\text{Pf}[w(\Gamma_i)]}. \quad (4.10)$$

Each Γ_i is a so-called time-reversal invariant momentum (TRIM), which is a point in the reciprocal space where $\mathbf{k} = -\mathbf{k} + \mathbf{G}$, with \mathbf{G} being a reciprocal lattice vector, see Fig. 4.2. $w(\mathbf{k})$ is a $N \times N$ matrix (N the number of occupied bands) defined as

$$w_{mn}(\mathbf{k}) = \langle u_{m,-\mathbf{k}} | \hat{\theta} | u_{n,\mathbf{k}} \rangle, \quad (4.11)$$

with the periodic wave functions $u_{m,\mathbf{k}}$ and the time-reversal operator $\hat{\theta} = -i\hat{\sigma}_y \hat{K}$ [82]. Here $\hat{\sigma}_y$ and \hat{K} denote the Pauli matrix and the complex conjugation, respectively. The Pf operator is the Pfaffian, which is only defined at the TRIMs.

The crucial point in equation (4.10) is the fact, that the branch of the square root has to be chosen continuously between the TRIMs. Therefore, the evaluation is not trivial and it does not suffice to calculate the wave functions at the TRIMs, but the phase of the states $u_{m,\mathbf{k}}$ has to be chosen continuous between the TRIMs. Therefore, the wave functions have to be calculated for a large number of wave vectors \mathbf{k} located between the TRIMs, complicating the evaluation of the equation.


 Figure 4.2: A quadratic 2D BZ with its TRIMs Γ_i .

An equivalent expression, similar to equation (4.1) for calculating the Chern number, is the Fu-Kane formula [77]:

$$\nu = \frac{1}{2\pi} \left[\sum_n \left\{ \oint_{\partial BZ_{1/2}} dl A_n(\mathbf{k}) - \int_{BZ_{1/2}} d^2k \Omega_n(\mathbf{k}) \right\} \right] \text{ mod } 2. \quad (4.12)$$

Here, the \mathcal{Z}_2 invariant is expressed as a difference of two integrals over one half of the BZ with the integrands being the Berry connection and the Berry curvature. The wave functions have to fulfil the time reversal constraint

$$\left| u_n^I(-\mathbf{k}) \right\rangle = \hat{\theta} \left| u_n^{II}(\mathbf{k}) \right\rangle, \quad \left| u_n^{II}(-\mathbf{k}) \right\rangle = -\hat{\theta} \left| u_n^I(\mathbf{k}) \right\rangle. \quad (4.13)$$

The Fu-Kane formula, equation (4.12), can be further discretized according to Fukui and Hatsugai [78]. In this approach, the integration area denoted by B^- , green in Fig. 4.3 a), is divided into a relatively small number of plaquettes for which an integer valued quantity is calculated. The resulting \mathcal{Z}_2 invariant ν is given as a sum of these integers, modulo 2.

First, the BZ is divided into three parts: B_s^\pm , the two halves of the BZ which are connected by the TRS, and B_s^0 , which is the set of all TRIMs in the BZ, see Fig. 4.3 a) for more details. The discrete lattice points \mathbf{k}_l belong to one of the three parts. The states at the lattice points have to fulfil the time reversal constraint, equation (4.13):

$$\left| n(-\mathbf{k}_l) \right\rangle = \hat{\theta} \left| n(\mathbf{k}_l) \right\rangle, \quad \mathbf{k}_l \in B_s^- \quad (4.14)$$

and

$$\left| 2n(\mathbf{k}_l) \right\rangle = \hat{\theta} \left| 2n-1(\mathbf{k}_l) \right\rangle, \quad \mathbf{k}_l \in B_s^0. \quad (4.15)$$

In the next step, using the multiplet of the $2N$ occupied states $\psi = (|n_1\rangle, \dots, |n_{2N}\rangle)$, the link variable

$$U_\mu(\mathbf{k}_l) = N_\mu^{-1}(\mathbf{k}_l) \det \left[\Psi^\dagger(\mathbf{k}_l) \Psi(\mathbf{k}_l + \mathbf{s}_\mu) \right] \quad (4.16)$$

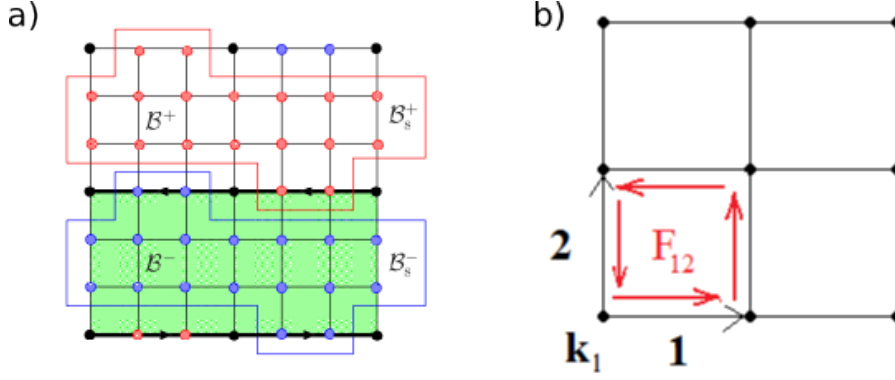


Figure 4.3: a) The division of the BZ into the three parts B_s^\pm (red and blue dots) and B_s^0 (black dots). B^\pm are the upper and lower halves of the BZ. Figure from [78].
 b) Field strength F_{12} through a plaquette variable.

with the normalization $N_\mu(\mathbf{k}_l) = |\det [\Psi^\dagger(\mathbf{k}_l) \Psi(\mathbf{k}_l + \mathbf{s}_\mu)]|$ can be defined. \mathbf{s}_μ is a vector connecting two neighbouring lattice points, $\mu = 1, 2$. The phase of the link variable, the gauge potential

$$A_\mu(\mathbf{k}_l) = \ln U_\mu(\mathbf{k}_l), \quad -\pi < -iA_\mu(\mathbf{k}_l) \leq \pi, \quad (4.17)$$

can be seen as a phase change of the states when going from \mathbf{k}_l to $\mathbf{k}_l + \mathbf{s}_\mu$. The field strength F_{12} through a plaquette variable when going along a closed rectangle spanned by the vectors \mathbf{s}_1 and \mathbf{s}_2 , see Fig. 4.3 b), is defined as

$$F_{12}(\mathbf{k}_l) = \ln \left[U_1(\mathbf{k}_l) U_2(\mathbf{k}_l + \mathbf{s}_1) U_1^{-1}(\mathbf{k}_l + \mathbf{s}_2) U_2^{-1}(\mathbf{k}_l) \right] \quad (4.18)$$

The values of F_{12}/i have to be in the $(-\pi, \pi)$ branch of the logarithm. Using the gauge potential, the field strength can be redefined as

$$F_{12}(\mathbf{k}_l) = \Delta_1 A_2(\mathbf{k}_l) - \Delta_2 A_1(\mathbf{k}_l) + 2\pi i n_{12}(\mathbf{k}_l), \quad (4.19)$$

with Δ_μ being the discretized differential operator with the following effect on the function f : $\Delta_\mu f(\mathbf{k}_l) = f(\mathbf{k}_l + \mathbf{s}_\mu) - f(\mathbf{k}_l)$ [83]. The integral field $n_{12}(\mathbf{k}_l)$ was introduced to ensure that the field strength stays in the correct branch.

Equation (4.19) establishes a relationship similar to that between the Berry connection and curvature: the field strength F_{12} and the gauge potential A_μ are the discretized Berry curvature and connection [84]. Thus, the Fu-Kane formula (4.12) can be rewritten in discretized form,

$$\nu = \frac{1}{2\pi i} \left[\sum_{\mathbf{k}_l \in \partial B^-} A_1(\mathbf{k}_l) - \sum_{\mathbf{k}_l \in B^-} F_{12}(\mathbf{k}_l) \right] \text{ mod } 2. \quad (4.20)$$

The sum of the field strength in all plaquettes in the lower half of the BZ B^- can be rewritten by using equation (4.19):

$$\sum_{\mathbf{k}_l \in B^-} F_{12}(\mathbf{k}_l) = \sum_{\mathbf{k}_l \in \partial B^-} A_1(\mathbf{k}_l) + 2\pi i \sum_{\mathbf{k}_l \in B^-} n_{12}(\mathbf{k}_l). \quad (4.21)$$

Most of the contributions to the sum of the field strength vanish, because the phase differences between two neighbouring lattice points occur always twice but with opposite

sign, owing to the opposite orientation of the vector \mathbf{s}_μ . Only contributions from the horizontal boundaries of B^- do not cancel.

Plugging equation (4.21) into equation (4.20) leads to the final result for the \mathcal{Z}_2 invariant via the discretized Fu-Kane formula:

$$\nu = \left[- \sum_{\mathbf{k}_l \in B^-} n_{12}(\mathbf{k}_l) \right] \text{ mod } 2. \quad (4.22)$$

Equation (4.22) was directly implemented in the TB code and used for calculating the \mathcal{Z}_2 invariants of TIs. The advantage of this approach is the possibility to calculate the integrals in equation (4.12) on a coarse mesh, since the result is always an integer and the result is exact for a dense enough mesh. One still has to be careful and check for convergence, since it is a priori not clear when the Fu-Kane-Formula is reproduced correctly by its discretized version, equation (4.20).

Evolution of Wannier-Function Centers

A second method to calculate the \mathcal{Z}_2 invariants used in this work is tracking the evolution of Wannier function centers, also called the maximally localized Wannier function (MLWF) method. The approach was proposed by Yu *et al.* [85] and is based on the idea of calculating the evolution of the Wannier function centers during a time-reversal pumping process [77].

Wannier functions in cell \mathbf{R} are Fourier transforms of the Bloch functions $\Psi_{n,k}(\mathbf{r})$ [86],

$$\langle \mathbf{r} | \mathbf{R}, n \rangle = W_n(\mathbf{r} - \mathbf{R}) = \frac{A}{(2\pi)^2} \int_{\text{BZ}} d\mathbf{k} e^{-i\mathbf{k} \cdot \mathbf{R}} \Psi_{n,k}(\mathbf{r}). \quad (4.23)$$

A is the area of the 2D unit cell.

A system at a TRIM is doubly Kramers degenerate and therefore, there exist pairs of Wannier functions with the same center $\langle \mathbf{R}, n | \hat{X} | \mathbf{R}, n \rangle$, \hat{X} is the position operator. During an adiabatic evolution in \mathbf{k} , the degeneracy of the centers is lifted until another TRIM is reached. Then the centers are degenerate again, but it can happen that the partners sharing the same center are different from the pair at the original TRIM. In this case a partner-switching process occurred and the system is topologically non-trivial with $\nu = 1$; see [77] for details.

The centers and their evolution between $k_y = 0$ and $k_y = \pi/a_y$ are calculated directly for effective 1D systems with fixed k_y . The position operator is defined as

$$\hat{X} = \sum_{i,\alpha} e^{-i\delta k_x R_i^x} |\alpha, i\rangle \langle \alpha, i| \quad (4.24)$$

with the basis set of atomic orbitals $|\alpha, i\rangle = \phi_\sigma(\mathbf{r} - \mathbf{R}_i - \mathbf{t}_l)$. $\delta k_x = 2\pi/N_x a_x$ with the number of cells along the x direction N_x and the lattice constant a_x . The eigenvalues of \hat{X} are $e^{-i\delta k_x R_i^x}$ with the phase representing a position. They are the centers of MLWFs.

Since the \mathcal{Z}_2 is a property of occupied states only, the position operator has to be projected onto the occupied bands by

$$\hat{P}_{k_y} = \sum_{n \in \text{occ}, k_x} |\Psi_{n,k}\rangle \langle \Psi_{n,k}|, \quad (4.25)$$

giving

$$\hat{X}_P(k_y) = \hat{P}_{k_y} \hat{X} \hat{P}_{k_y}. \quad (4.26)$$

Plugging in the TB ansatz, equation (3.1), leads to its matrix form

$$\hat{X}_P(k_y) = \left\{ \begin{array}{cccccc} 0 & F_{0,1} & 0 & \dots & 0 & 0 \\ 0 & 0 & F_{1,2} & \dots & 0 & 0 \\ 0 & 0 & 0 & \dots & 0 & 0 \\ \vdots & \vdots & \vdots & \ddots & \vdots & \vdots \\ 0 & 0 & 0 & \dots & 0 & F_{N_x-2, N_x-1} \\ F_{N_x-1,0} & 0 & 0 & \dots & 0 & 0 \end{array} \right\}. \quad (4.27)$$

$F_{i,i+1}$ are $2N \times 2N$ matrices with the elements

$$F_{i,i+1}^{n,m}(k_y) = \sum_{\alpha} c_{n,\alpha}^* (k_x^i, k_y) c_{n,\alpha} (k_x^{i+1}, k_y) \quad (4.28)$$

expressing overlaps of states at neighbouring discrete k points along the x axis, $k_x^i = 2\pi/N_x a_x$.

In the next step the product of the overlap matrices

$$D(k_y) = F_{0,1} F_{1,2} F_{2,3} \dots F_{N_x-2, N_x-1} F_{N_x-1,0} \quad (4.29)$$

can be defined, which is a $2N \times 2N$ matrix with the eigenvalues

$$\lambda_m^D(k_y) = |\lambda_m^D| e^{i\theta_m^D(k_y)}, \quad m = 1, \dots, 2N. \quad (4.30)$$

The phases of the eigenvalues,

$$\theta_m^D(k_y) = \Im \left[\log \lambda_m^D(k_y) \right], \quad (4.31)$$

are the centers of the Wannier functions, whose evolution along k_y gives the \mathcal{Z}_2 invariant.

In [85] and [87] it is further shown that $D(k_y)$ is equal to a $U(2N)$ Wilson loop for the non-Abelian Berry connection

$$D(k_y) = P \exp \left[\int_{C_{k_y}} -iA(k) dk \right] \quad (4.32)$$

with a fixed contour parallel to the k_x axis.

Finally, as stated above, pairs of Wannier function centers are degenerate at the TRIMs $k_y = 0$ and $k_y = \pi$, but they are independent for k_y values between the TRIMs. Two centers can differ by a multiple of 2π when coming together at the second TRIM. By folding the θ - k_y plane to form a cylinder with the $\theta = -\pi$ and $\theta = \pi$ lines glued together, a pair of Wannier function centers can be viewed to enclose the cylinder an integer number of times. The \mathcal{Z}_2 invariant is given as the total number of times the pairs of centers wind around the cylinder, modulo two. A graphical evaluation of the invariant is to plot the Wannier function centers θ_m^D against k_y . At an arbitrary θ a horizontal line is drawn. The \mathcal{Z}_2 invariant can then be calculated by counting the number of crossings between the centers and the reference line, modulo two. For an example see Fig. 4.4.

When this procedure for calculating the topological invariants should be implemented in the TB model, an additional gauge fixing has to be applied to the eigenvectors $c_{n,\alpha}$ of the TB matrix, in order to assure the continuity of the states in the BZ. This is achieved by the so-called parallel transport gauge, described by A. Soluyanov [88]. Considering a single band, the states at k and $k + \Delta k$ differ by a $U(1)$ phase

$$\phi = \Im \log \langle u_n(k) | u_n(k + \Delta k) \rangle. \quad (4.33)$$

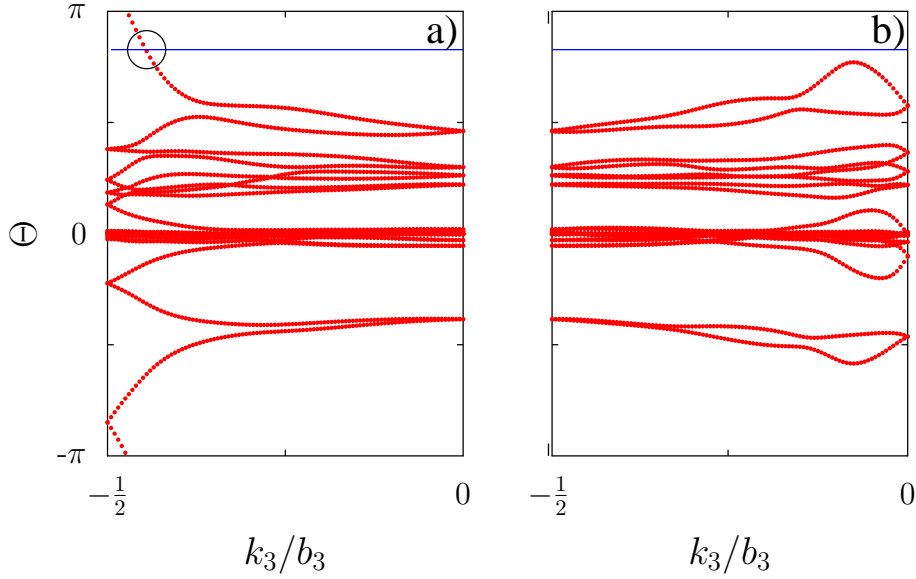


Figure 4.4: Calculated Wannier function centers for two distinct time-reversal invariant planes of Bi_2Te_3 . a) The blue reference line is crossed once between two TRIMs, indicating $\nu = 1$. b) The reference line has no crossings with the Wannier function centers, the \mathcal{Z}_2 invariant $\nu = 0$.

To ensure the parallel transport, the overlap $\langle u_n(\mathbf{k}) | u_n(\mathbf{k} + \Delta\mathbf{k}) \rangle$ should be positive real, assuring the change of the state is perpendicular to the state itself. This can be fixed by the transformation

$$u'_n(\mathbf{k}) = e^{-i\phi} u_n(\mathbf{k}). \quad (4.34)$$

In the non-Abelian case of a set of $2N$ occupied states, the requirement is that the overlap matrix $F_{i,i+1}^{n,m}$ in equation (4.28) is Hermitian with positive eigenvalues. This can be achieved by singular value decomposition, in which a matrix M is decomposed to $M = V\Sigma W^\dagger$ with V and W unitary and Σ positive real diagonal. Rotating the states at $\mathbf{k} + \Delta\mathbf{k}$ by $U = WV^\dagger$ ensures the desired properties.

In the TB model, both methods for calculating the \mathcal{Z}_2 invariants were implemented successfully. For the systems studied, both procedures give identical results, thus proving their reliability in predicting the topological character of real insulating materials.

Surface States

When the investigated system is a non-trivial TI, then by bulk-boundary correspondence there has to be an odd number of surface state pairs connecting the valence and the conduction bands at any edge of the 2D system. Due to the Kramers theorem [89] each pair of the surface states has to fulfil $E_{n,k} = E_{n,-k}$. In addition, both surface states have a crossing at a surface TRIM. A typical shape of the surface band structure is presented in Fig. 4.5. This can be also seen as a pair of 1D states propagating along the edge of the 2D system. The states forming the pair move in opposite directions and carry oppositely oriented spin, obeying the TRS.

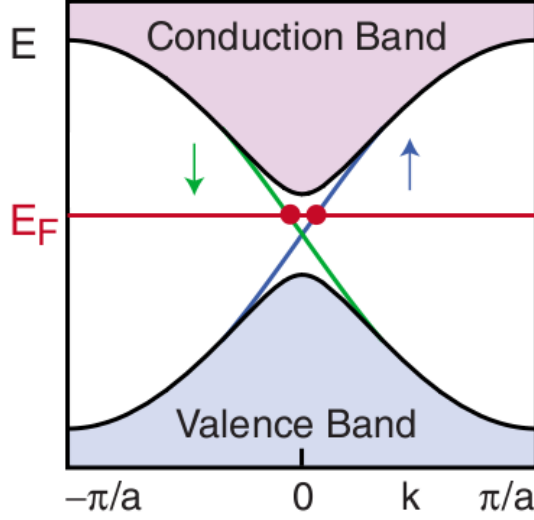


Figure 4.5: A pair of surface states connecting the valence and conduction bands at the edge of a 2D topological insulator of the QSHE type, from [53].

One of the most important properties of the topological surface states is their stability and robustness against impurities. By bulk-boundary correspondence, there have to be surface states at the edge of a non-trivial system. Since the invariant remains unchanged as long as the fundamental band gap does not close and the TRS is preserved, the existence of the surface states is secured unless an external perturbation breaking the previous conditions is applied to the system.

In addition, even backscattering of the edge states, which could be caused by impurities, is forbidden, as long as TRS is present. This means the impurities have to possess zero magnetic moments. A proof of this fact is given in reference [90]. Consider n surface states propagating at the edge in one direction are described by $|\Phi\rangle$ and other n states propagating in the opposite direction by $|\Psi\rangle$, connected by the time-reversal operator $\hat{\theta}$: $|\Psi\rangle = \hat{\theta}|\Phi\rangle$. Since the time-reversal operator consists of a product of a unitary transformation U and the complex conjugation \hat{K} [82],

$$\langle \hat{\theta}\alpha | \hat{\theta}\beta \rangle = \langle \hat{K}\alpha | \hat{K}\beta \rangle = \langle \beta | \alpha \rangle \quad (4.35)$$

holds for arbitrary states $|\alpha\rangle$ and $|\beta\rangle$. Assuming now a time-reversal invariant perturbation \hat{V} satisfying $[\hat{V}, \hat{\theta}] = 0$, e.g., an impurity, then the matrix element $\langle \Psi | \hat{V} | \Phi \rangle$ describing the backscattering of the surface states reads

$$\langle \Psi | \hat{V} | \Phi \rangle = (-1)^n \langle \Psi | \hat{V} | \Phi \rangle. \quad (4.36)$$

Here, equation (4.35) and $\hat{\theta}^2 = -1$ for an odd number of fermions and $\hat{\theta}^2 = 1$ for an even number of fermions were used. Equation (4.36) establishes that backscattering is forbidden by TRS for an odd number n of surface state pairs, especially $n = 1$. This exactly corresponds to the prediction based on the value of the \mathcal{Z}_2 invariant: if non-trivial, then there is an odd number of surface state pairs at the edge with forbidden backscattering, leading to a constant resistance independent of the perturbation of the system. This proof relies on one-particle scattering without electron-electron interaction. Effects of more complicated many-particle scattering processes are discussed e.g., in reference [90].

4.5 3D TIME-REVERSAL INVARIANT TOPOLOGICAL INSULATORS

Soon after the discovery of time-reversal invariant TIs in 2D systems, in 2007 a generalization to three dimensions was published [79, 91, 92]. As in the 2D case, the time-reversal invariance is the key symmetry for this type of TIs. The first realistic material, $\text{Bi}_{1-x}\text{Sb}_x$ was proposed to be a 3D TI in 2007 [93] and it was confirmed by ARPES in 2008 [94]. Soon, many more systems were proposed to be TIs, in particular the chalcogenides Bi_2Te_3 , Bi_2Se_3 and Sb_2Te_3 [95, 96], which are now the mostly investigated 3D TIs.

 \mathcal{Z}_2 Invariants for 3D Topological Insulators

The mathematical classification of 3D TIs is similar to the 2D case, but with need for four distinct \mathcal{Z}_2 invariants in 3D. A derivation of the invariants was given by Roy [92]. Assuming a cubic BZ $\{-\pi \leq k_x, k_y, k_z \leq \pi\}$ for simplicity, there are six independent time-reversal invariant planes $k_x = 0, k_x = \pi, k_y = 0, k_y = \pi, k_z = 0, k_z = \pi$ which are mapped on themselves under time-reversal. For each of these planes \mathcal{Z}_2 invariants $\nu_1, \tilde{\nu}_1, \nu_2, \tilde{\nu}_2, \nu_3$ and $\tilde{\nu}_3$ can be calculated exactly as in the 2D case, since each of the planes possesses the same torus topology as a 2D BZ.

For further derivation it is useful to discuss an alternative way of calculating the \mathcal{Z}_2 invariant [92, 97]. In time-reversal invariant systems, it is possible to decompose the eigenstates of the Hamiltonian into two groups *I* and *II*, connected with each other by the time-reversal operator. For each of these groups a Chern number $C_{I/II}$ can be calculated. The sum $C_I + C_{II}$ is zero because of TRS but the difference gives the \mathcal{Z}_2 invariant as

$$\nu = \frac{1}{2} (C_I - C_{II}) \pmod{2}. \quad (4.37)$$

This approach is similar to that in section 4.6. In this case, the quantity $\frac{1}{2} (C_I - C_{II})$ would be the spin Chern number when the states in the groups *I* and *II* differ in the sign of their spin eigenvalue.

After introducing a way of calculating the \mathcal{Z}_2 invariant via the Chern numbers, it can be shown that $\nu_1, \tilde{\nu}_1, \nu_2, \tilde{\nu}_2, \nu_3$ and $\tilde{\nu}_3$ are not independent. First, consider a composite plane $S = S' \cup S'' \cup S'''$ with $S' = \{\mathbf{k} : k_y = 0\}$, $S'' = \{\mathbf{k} : k_y > 0, k_z = \pi\}$ and $S''' = \{\mathbf{k} : k_y < 0, k_z = -\pi\}$, as in Fig. 4.6 (a). The plane S is time-reversal invariant and therefore a \mathcal{Z}_2 invariant $\nu(S)$ can be associated with it. Furthermore, because of the periodicity of the BZ, the composition $S'' \cup S'''$ is equivalent to the $k_z = \pi$ plane. From equation (4.37) it follows that

$$\nu(S) = \nu_2 + \tilde{\nu}_3, \quad (4.38)$$

the sum of the invariants of the two time-reversal invariant planes.

In the following step, the composite plane S can be deformed continuously in a way that it is always time-reversal invariant (see Fig. 4.6 (b)), until it takes the form $\tilde{S} = \tilde{S}' \cup \tilde{S}'' \cup \tilde{S}'''$ with $\tilde{S}' = \{\mathbf{k} : k_z = 0\}$, $\tilde{S}'' = \{\mathbf{k} : k_y = \pi, k_z > 0\}$ and $\tilde{S}''' = \{\mathbf{k} : k_y = -\pi, k_z < 0\}$, i.e. the composition of the $k_z = 0$ and $k_y = \pi$ planes (Fig. 4.6 (c)). Therefore,

$$\nu(\tilde{S}) = \tilde{\nu}_2 + \nu_3. \quad (4.39)$$

Since the deformation is continuous, the \mathcal{Z}_2 invariant cannot change its value: $\nu(S) = \nu(\tilde{S})$. The same procedure for the other time-reversal invariant planes in the BZ leads to

$$\nu_1 - \tilde{\nu}_1 = \nu_2 - \tilde{\nu}_2 = \nu_3 - \tilde{\nu}_3, \quad (4.40)$$

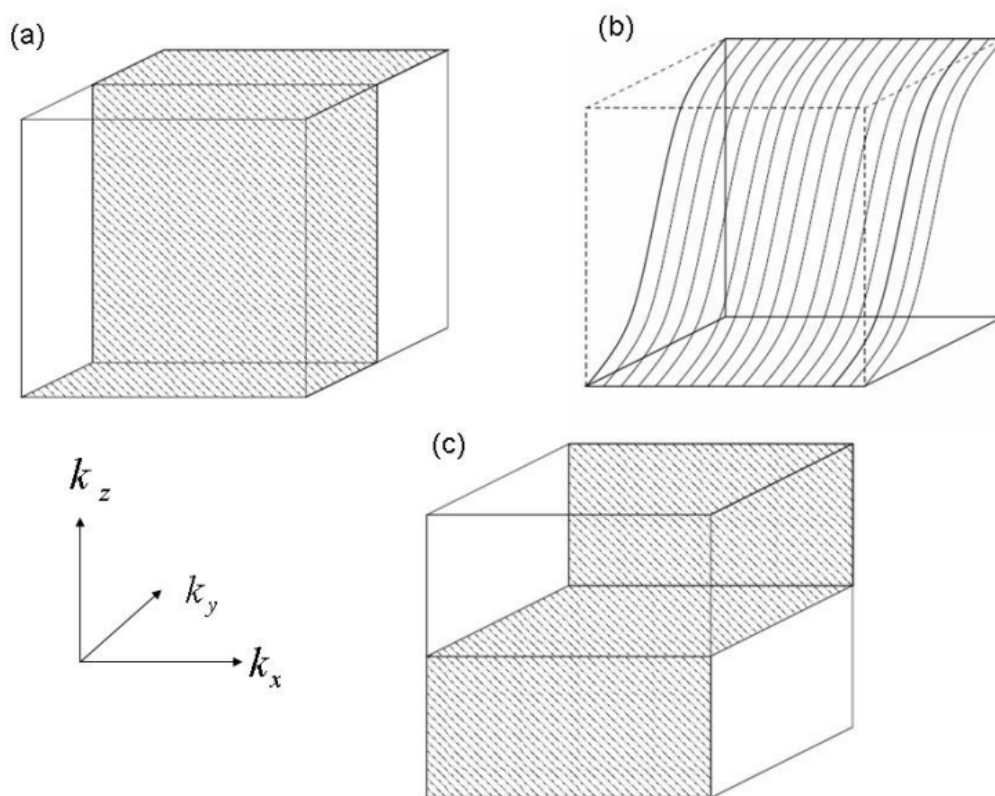


Figure 4.6: Composite time-reversal invariant plane S . (a) Before, (b) during and (c) after the continuous deformation, from [92].

demonstrating the dependence of the invariants. Therefore, from the original six invariants four independent \mathcal{Z}_2 invariants $|\nu_1 - \tilde{\nu}_1|$, $\tilde{\nu}_1$, $\tilde{\nu}_2$ and $\tilde{\nu}_3$ suffice to describe 3D time-reversal invariant TIs. Usually, the notation

$$\nu_0(\nu_1, \nu_2, \nu_3)$$

is used for the quadruple of invariants.

The system is topologically non-trivial, when one of the invariants has a non-zero value. When $\nu_0 = 1$, the system is a strong topological insulator (STI), otherwise it is a weak topological insulator (WTI). The invariant ν_0 is therefore often called the strong invariant.

Surface States

The surface states of 3D time-reversal invariant TIs connect the bulk valence and conduction bands, similar to the 2D case [91]. Since TRS is present, the surface states have to be Kramers degenerate with a double degeneracy at the surface TRIMs. These degeneracy points are called Dirac points and the surface states the Dirac cones, owing to the conical shape of the surface state, see Fig. 4.7 a), and to the fact that the dispersion of the surface state is similar to the dispersion of massless fermions which can be described by a massless Dirac equation near the Dirac point [98]. In this low-energy picture, spin-momentum locking shows up, which means the spin is oriented in-plane, tangential to the Dirac cone, rotating clockwise or anti-clockwise along a constant energy cut of the Dirac cone [4]. In real systems, due to additional symmetries (e.g., rotations), the spin-momentum locking occurs perfectly only along high-symmetry lines (e.g., in mirror-planes). As can be seen in e.g., Bi_2Te_3 , even a non-vanishing out-of plane spin component is possible [99].

Surfaces of TIs can feature more than one Dirac cone in the surface BZ. In STIs, there is an odd number of Dirac cones in the surface BZ at each crystal surface. The double degeneracy at the surface TRIM is protected, as long as TRS is not broken. Therefore, the surface states of TIs are robust to time-reversal invariant disorder, as was already discussed for the 2D case. However, there is a difference between the 1D edge states of 2D TIs and 2D surface states of 3D TIs. Backscattering is forbidden by TRS for both 1D and 2D surface states but in the 2D case surface states scattering from the wave vector k into $k' \neq -k$ is allowed, leading to a lesser robustness against impurities compared with the 1D edge states, for which only the wave vectors k and $-k$ are possible.

In contrast to STIs, the protection of the surface states in WTIs is reduced. WTIs can be seen as a stacking of planes of 2D time-reversal invariant TIs having no surface states at the surface perpendicular to the stacking direction, see Fig. 4.7 b). In the surfaces parallel to the stacking direction, an even number of Dirac cones is located at the surface TRIMs in each surface BZ. The surface states have to cross at non-TRIM points, at which the degeneracy is not protected by TRS. Weak disorder can split this degeneracy, which would lead to an insulating behaviour, even at the surface.

4.6 3D TOPOLOGICAL CRYSTALLINE INSULATORS

In TIs, time-reversal is not the only symmetry operation which can produce topological phases. Spatial symmetries of the crystal lattice can be also used to define topological

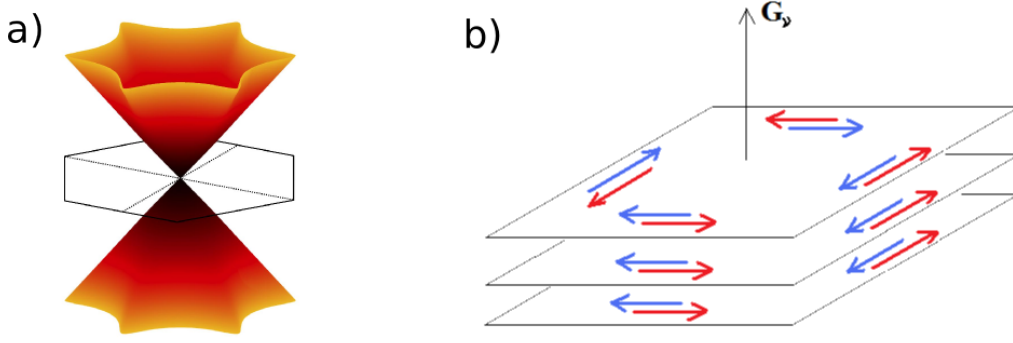


Figure 4.7: a) A typical shape of a surface state in TIs. Near the crossing (Dirac point) the shape is conical and can become warped at energies above or below the Dirac point. Figure from [TR2]. b) WTI, seen as a stacking of 2D time-reversal invariant TIs. Blue and red arrows sketch the propagation of the surface states into opposite directions, depending on the spin orientation.

classes with surface states protected by the given symmetry. In the original paper of Fu [100] from 2011 mostly rotational symmetries are discussed. Yet since the discovery of the first realistic material being a topologically crystalline insulator (TCI) – SnTe, both predicted theoretically [101] and confirmed experimentally [102] in 2012 – with surface states protected by the mirror symmetry of the crystal, predominantly mirror symmetry protected TCIs were investigated. In the following, TCIs will always mean mirror-symmetric TCIs.

Mirror Chern Number

The mirror Chern number is a topological invariant used to characterize TCIs. It was introduced by Teo, Fu and Kane [103] to characterize the surface states in $\text{Bi}_{1-x}\text{Sb}_x$.

Similar to 3D time-reversal symmetric TIs, only special planes in the BZ are considered. In this case these are the cuts of the mirror planes with the BZ. The states with wave vectors in the mirror plane are the eigenstates of the mirror operator, having eigenvalues of $\pm i$. Following the idea of the spin Chern number [97], the states can be divided into two groups according to their mirror eigenvalue. For each group the Chern number is calculated, considering only the states with the same mirror eigenvalue. In the presence of TRS, $C_{+i} + C_{-i} = 0$, but the mirror Chern number

$$n_M = \frac{1}{2} (C_{+i} - C_{-i}) \quad (4.41)$$

can be non-zero.

Since there are often multiple non-equivalent mirror planes present in the crystal lattice, the mirror Chern numbers for all these mirror planes should be calculated to fully characterize the topological phase of the system and to get the full information about the surface states, pointed out by Kim *et al.* in 2015 [104].

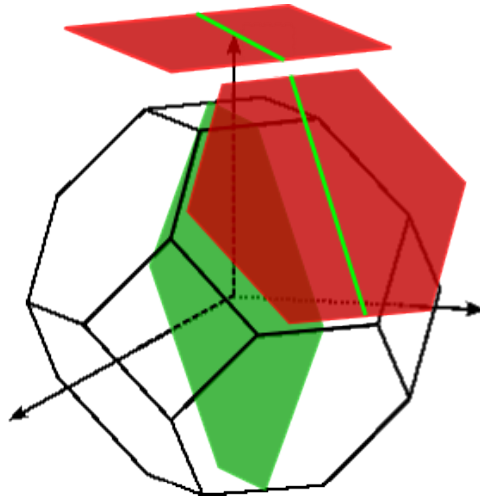


Figure 4.8: BZ of a face-centred cubic lattice. The green plane – a cut of the mirror plane with the BZ – is the integration area for calculating the mirror Chern number. The surface states occur at the mirror line (green) in the surface BZ (red) of each surface perpendicular to the mirror plane.

Surface States

In analogy to Chern insulators the number of surface states in TCIs is given by the mirror Chern number (bulk-boundary correspondence). Here, the prediction holds only for the surfaces perpendicular to the mirror plane of interest. The modulus of the mirror Chern number is equal to the number of surface state pairs located at mirror lines, which are the projections of the mirror plane onto the surface BZ, see Fig. 4.8. On these lines, all crossings of the surface states are protected by the mirror symmetry, which is the reason for the surface of TCIs being metallic, as long as the mirror symmetry is preserved.

 TOPOLOGICAL SEMIMETALS

5.1 INTRODUCTION

Besides insulating materials, the interest in topological characterization of metals is growing rapidly. In the following, metal will be understood as a material in which – in the investigated energy region – for each energy value bulk states exist at this energy. This means that there is no global band gap in the investigated part of the band structure.

The most important members of the topological metals group are topological Dirac semimetals (TDSs) (section 5.2) and WSMs (section 5.3). These topological phases possess robust Dirac cones in their bulk band structure and can be characterized by topological invariants. In addition to the unusual bulk states, they also feature surface states which show unique transport properties.

5.2 TOPOLOGICAL DIRAC SEMIMETALS

The key feature of TDSs is the existence of topologically protected Dirac cones within the 3D bulk. Therefore, this class of materials is often called “3D graphene”, reminding of the 2D Dirac cones in graphene [105]. Similar to it, also TDSs should possess novel interesting transport properties, calculated e.g. for Cd_3As_2 [106]. A comprehensive classification of TDSs depending on the crystal symmetry was given by Yang and Nagaosa in 2014 [107] as well as by Yang, Morimoto and Furusaki in 2015 [108].

A Dirac cone can be observed in bulk of 3D TIs, when the system is tuned exactly to the quantum critical point where the transition between a TI and a normal insulator occurs [109]. At this point, the valence and conduction bands touch and form a 3D Dirac cone. Unfortunately, this point in the topological phase diagram can be achieved experimentally only by very accurate tuning and it would then still be vulnerable to weak perturbations. In contrast, the Dirac cones in TDSs are protected by crystal symmetries and their splitting by symmetry-conserving perturbations is prohibited.

Yang and Nagaosa [107] studied general systems with TRS and inversion symmetry (IS). These two symmetries require $E_{n,\sigma}(\mathbf{k}) = E_{n,-\sigma}(-\mathbf{k})$ and $E_{n,\sigma}(\mathbf{k}) = E_{n,\sigma}(-\mathbf{k})$. Combined they give $E_{n,\sigma}(\mathbf{k}) = E_{n,-\sigma}(\mathbf{k})$, therefore the bands are doubly degenerate at each k . An accidental band crossing (ABC) would lead to a four-fold degeneracy at the crossing point. Assuming additional rotational symmetries, the ABCs can exist for a finite range of system-controlling parameters. The authors discuss two types of Dirac semimetals. In the first case, a single Dirac cone is located at a TRIM. In the second case a pair of Dirac cones exists on a rotational axis (e.g. k_z), see Fig. 5.1 left. Then the $k_z = 0$ plane features no crossings of the conduction and valence bands and various topological

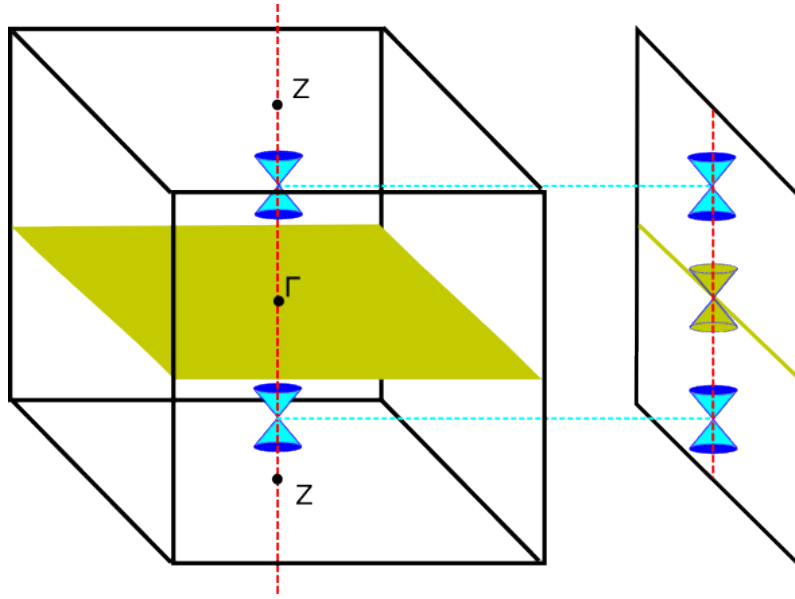


Figure 5.1: Left: Cubic bulk BZ with a pair of Dirac cones (blue) located at the k_z axis. Topological invariants can be calculated for the $k_z = 0$ plane (green). Right: Surface BZ of the (100) surface with projected bulk k_z axis (red), bulk Dirac cones (blue) and the $k_z = 0$ plane (green). If the topological invariants calculated for the bulk $k_z = 0$ plane possess non-trivial values, then there would be surface states located at its projection onto the surface BZ (green line).

invariants can be calculated, when the plane possesses the required symmetries. Since a TR-symmetric system is considered, a \mathcal{Z}_2 invariant can be defined. When $k_z = 0$ is a mirror plane, then the mirror Chern number can be calculated.

The Dirac cones in TDSs are always doubly degenerate (with a four-fold degenerate Dirac point), in contrast to e.g. WSMs with non-degenerate bands (except at crossings, i.e., at Weyl points), see section 5.3. In the literature [107, 108], by assuming the presence of both TRS and IS, the twofold degeneracy of all bands is assured. This does not mean that the presence of IS is necessary for TDSs. Twofold degenerate bands in special regions in the BZ can be achieved by the presence of other crystalline symmetries, for example screw axes or glide planes, even if IS is violated. Therefore, TDSs can exist also in systems without an inversion center, e.g., in strained HgTe, see section 6.5.

Surface States

Topologically non-trivial TDSs possess very interesting surface properties. From the bulk-boundary correspondence it follows, that surface states protected by symmetry should exist at surfaces which are perpendicular to the plane for which the invariants were calculated. For an example see Fig. 5.1. For a system in which a mirror Chern number can be calculated, the behaviour of the surface states is exactly the same as in TCIs, section 4.6. If only the \mathcal{Z}_2 invariant can be calculated and is equal 1, then there is one pair of surface states with opposite spin orientation at the projection line with the Dirac point located at a TRIM, exactly as it is the case for 2D time-reversal invariant TIs.

The protection of the surface states by symmetry is in both cases valid only at the projection line. The surface states exist also in regions out of this line, but their crossings are not protected because the protecting symmetry is not present in these regions.

5.3 WEYL SEMIMETALS

Another type of metallic materials which can be characterized by topological invariants are the Weyl semimetals (WSMs). The name was first put by Wan *et al.* in 2011 [110]. While the bulk Dirac cones of TDSs can be in a low-energy limit described by the four-component Dirac equation, the properties of the Weyl fermions can be described by the Weyl equation, which is a two-component analogue of the Dirac equation for massless particles. Therefore, the key difference between TDSs and WSMs is that the Dirac cones are twofold degenerate with a fourfold degenerate crossing in the case of a TDS and non-degenerate with a twofold degenerate crossing in the case of a WSM. Since all bulk bands are doubly degenerate in a crystal with both TRS and IS, at least one of these symmetries has to be broken in order to realize a WSM.

The emergence of WSMs can be well understood by looking at the phase transition from a TI phase to a topologically trivial insulating phase. Assuming that the system is controlled by an external parameter m , then the WSM phase exists for a finite range $m_1 < m < m_2$. m_1 and m_2 are the critical points at which the valence and conduction bands touch. For $m < m_1$ the system is in one insulating phase and for $m > m_2$ in another, see Fig. 5.2 (a). Such phase transitions between topologically distinct insulating and metallic phases existent for a finite parameter range as phase boundary were discussed by Murakami in 2007 [111], later described in more detail [112, 113].

After the first proposal of WSMs in pyrochlore iridates [110], other systems were investigated theoretically, e.g., noncentrosymmetric TIs [114] or $\text{Hg}_{1-x-y}\text{Cd}_x\text{Mn}_y\text{Te}$ [115], with broken IS in the former case and TRS broken by doping with Mn atoms which carry a finite magnetic moment in the latter. The first WSM confirmed experimentally by ARPES is TaAs [116, 117], which was proposed theoretically by different groups [118, 119].

Topological Charge

The reason for the existence of the WSM phase in a finite region of the topological phase diagram is the fact that the Weyl points carry a topological charge to which a Chern number can be assigned. An effective Hamiltonian for a Weyl fermion has the form [120]

$$H_{\mathbf{k}} = v_{ij}k_i\sigma_j, \quad i, j = x, y, z, \quad (5.1)$$

with v_{ij} being velocities, \mathbf{k} the wave vector and σ_j Pauli matrices, satisfying the condition $\det[v_{ij}] \neq 0$. This effective Hamiltonian is the Weyl Hamiltonian and describes two bands with a linear dispersion crossing each other at $\mathbf{k} = 0$. A special case with $v_{ij} = \frac{1}{2}\delta_{ij}$ was discussed already by Berry [11] in 1984. He showed that the Berry curvature of the two bands is

$$\Omega_{\pm}(\mathbf{k}) = \pm \frac{\mathbf{k}}{2k^3}, \quad (5.2)$$

which has the same structure as the magnetic field of a magnetic monopole with a magnetic charge of $\mp \frac{1}{2}$ [121]. Therefore, by analogy it can be stated that the Weyl points

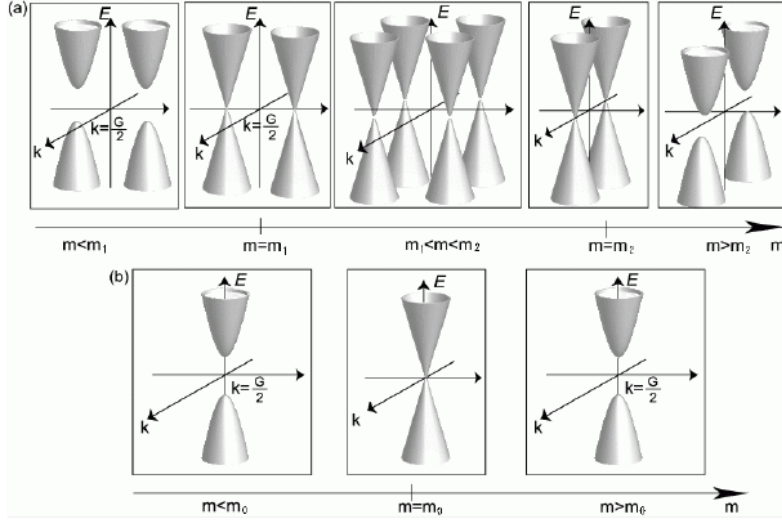


Figure 5.2: Phase transition between two topologically non-equivalent insulating phases controlled by the parameter m . a) The system is not invariant under IS. At $m = m_1$ the bulk bands form Dirac points with a four-fold degeneracy. Increasing m leads to a splitting of each Dirac point into two-fold degenerate Weyl points. Other pairs of Weyl points meet for $m = m_2$ and they annihilate again. The system enters an insulating phase for $m > m_2$. b) The system is invariant under IS and the bands are always two-fold degenerate, WSM phase cannot exist in a finite range of parameter values. Figure taken from [111].

are the monopoles of the Berry curvature field. In equation (5.2) $+$ ($-$) denotes the band energetically above (below) the Weyl point located at $E = 0$ and $\mathbf{k} = 0$.

A sphere in \mathbf{k} space with a finite radius surrounding the Weyl point has a closed surface S . Integrating the projection of the Berry curvature Ω_- of the occupied (lower) band onto the surface normal \mathbf{n} over the whole surface S gives the Chern number

$$c = \frac{1}{2} \int_S d^2k \Omega_-(\mathbf{k}) \cdot \mathbf{n}. \quad (5.3)$$

By this procedure, Weyl points can be found as in equation (4.1) also in bulk band structures of real materials. It is necessary to ensure that the sphere is small enough to surround a single Weyl point. Otherwise, the result would be the sum of the topological charges of the enclosed Weyl points.

The fact that each Weyl point possesses a Chern number explains their robustness, since the Chern number can only change in discrete steps. In a WSM this is only possible when two Weyl points with an opposite topological charge (Chern number) meet. Then the pair of Weyl points annihilates and the bands can acquire a mass, i.e. a band gap opens up [113, 114] ($m = m_1$ or $m = m_2$ in Fig. 5.2 (a)).

Surface States

Similar to TDSs, also WSMs possess surface states attributed to the existence of a non-zero Chern number. The following explanation is based on that given in [110] and can be understood by means of Fig. 5.3. For simplicity, a cubic bulk BZ with two Weyl points

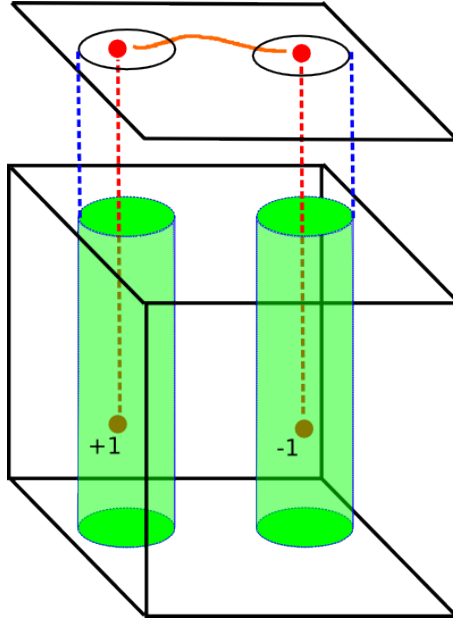


Figure 5.3: Bottom: A cubic BZ with two Weyl points (red dots) enclosed by cylinders (green) with a calculated Chern numbers ± 1 . Top: (001) surface Fermi surface with the projections of the Weyl points (red dots), cylinders (black loops) and a Fermi arc (orange) connecting the both Weyl point projections.

is considered. A cylinder oriented along the k_z direction encloses one Weyl point. The surface of the cylinder is a closed surface because of the periodicity of the BZ. Therefore, the Chern number can be calculated on this surface via equation (5.3), which is also the topological charge of the enclosed Weyl point. Introducing a (001) surface leads to a surface BZ, onto which the Weyl points and the cylinder are projected. The projection of the cylinder is a closed loop C with the projection of the Weyl point inside. By bulk-boundary-correspondence, if the Chern number is ± 1 , then a surface state has to cross the bulk band gap somewhere along the loop C . This surface state will cross any constant energy E in the bulk band gap. Therefore, when plotting a constant energy cut for any bulk band gap energy, the loop C will always cut a surface state at one point, as long as the cylinder is small enough to encircle only one Weyl point. If both Weyl points with opposite topological charges would lie inside the cylinder, then the Chern number would be zero and no surface states would cut the loop C in the constant energy cut. From this follows that, when the Fermi energy is equal to the Weyl point energy, the surface states are open lines connecting the projections of the Weyl points with opposite topological charges, hence called Fermi arcs.

Such a form of a Fermi surface is unique in the field of condensed matter physics and promises interesting new properties, such as anisotropic surface charge and spin transport. Furthermore, when a time-reversal symmetric system is considered, then for each Weyl point located at a wave vector k there is a Weyl point located at $-k$ having the same topological charge. Therefore, there are at least four Weyl points in the BZ when TRS is present. In reality, there are mostly even more Weyl points in the bulk BZ of a WSM [110, 114, 117] produced by additional crystal symmetries (e.g., reflections or rotations). As stated earlier, the Weyl point projections onto the surface BZ with different topological charges have to be connected by Fermi arcs when the Fermi energy

equals the Weyl point energy. Interestingly, it is not obvious which pairs of Weyl point projections have to be connected by the arcs. This can depend strongly on the choice of crystal termination, as was shown e.g., for TaP in [119]. In this compound, different pairs of Weyl point projections are connected by Fermi arcs for different crystal terminations (Ta or P). This fact can even restore the picture of Fermi lines being closed, when a crystal with both top and bottom surface is considered (as it is the case in slabs or thin films). Assuming two pairs of Weyl points, there are four Fermi arcs in total, two from the top and two from the bottom surface. Since different pairs of Weyl point projections are connected at the different surfaces, the four Fermi arcs establish a closed Fermi line. This will be discussed in more detail in section 6.5.

PUBLICATIONS

6.1 INTRODUCTION

In this chapter, selected publications are presented, which provide main results of the cumulative thesis. The investigated topics roughly follow the evolution of general interest of the topological materials community, beginning with the TIs and TCIs and ending – for the time being – with topological semimetals which are in the focus of the recent investigations.

6.2 PRESSURE-INDUCED TOPOLOGICAL PHASE TRANSITIONS IN ROCKSALT CHALCOGENIDES

This work [TR3], which was done in collaboration with the group of Silvia Picozzi from the University of L'Aquila in Italy, was motivated by the discovery of the first TCI, SnTe, in 2012 [101]. The main goal of the project was to investigate the electronic properties of other rocksalt chalcogenides similar to SnTe (PbTe, PbSe, PbS, and GeTe) and to understand the microscopical reasons for some of the materials being TCIs and others being normal insulators. Furthermore, the transition from a normal insulator to a TCI could be achieved by simulating hydrostatic pressure.

The first result of the work was that strong SOC is not the only reason for a system being topologically non-trivial, as is often stated in the literature. In the case of rocksalt chalcogenides also an asymmetry in the s - p hybridization plays an important role: the s_{CPA} and s_{APC} hybridizations differ sizeably. C and A denote the cation and anion, respectively.

The magnitude of the influence of the asymmetry on the electronic band structure can be further increased by hydrostatic strain, which was simulated by both DFT- and TB-based calculations. In the TB scheme, the bulk band structure was calculated for different lattice constants, identifying the phase transition point where the valence and conduction bands touch at the L point in the BZ, see Fig. 6.1, not shown in the publication. In addition, the mirror Chern number was calculated for all materials and lattice constant values, indicating that after passing the critical point the systems (with the exception of GeTe) become TCIs with mirror Chern number $n_M = -2$, same as SnTe under ambient conditions.

To further confirm the results, also the surface electronic structure was calculated for different values of the lattice constant, showing surface states crossing the whole band gap only in the TCI phase. The crossings occur only in the mirror lines (\bar{X} - $\bar{\Gamma}$) of the surface BZ, as is typical for TCIs, see Fig. 2 of the publication [TR3].

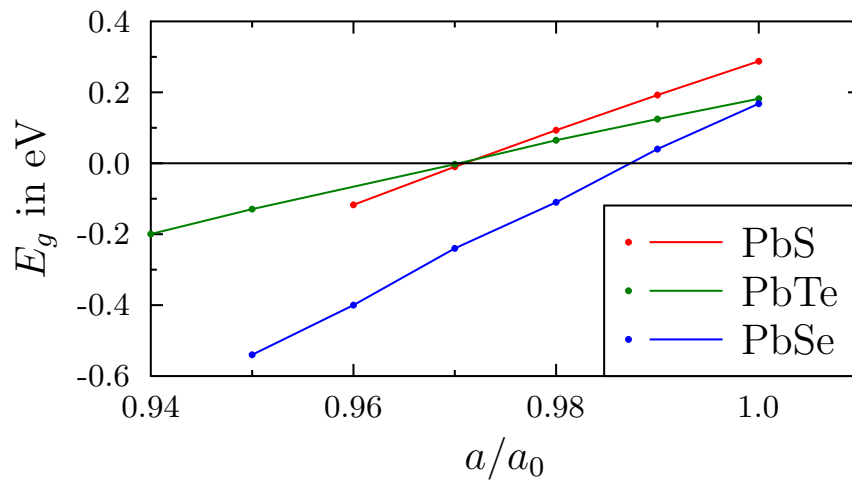


Figure 6.1: The band gap E_g of $\text{Pb}A$, $A = \text{S, Se, Te}$, calculated as the difference of the $\text{Pb-}p$ band and the $A-p$ band at the L point of the BZ, for different values of the lattice constant a . a_0 is the equilibrium lattice constant.

Pressure-induced topological phase transitions in rocksalt chalcogenides

Paolo Barone,¹ Tomáš Rauch,² Domenico Di Sante,^{1,3} Jürgen Henk,² Ingrid Mertig,² and Silvia Picozzi¹

¹Consiglio Nazionale delle Ricerche (CNR-SPIN), I-67100 L'Aquila, Italy

²Institut für Physik, Martin-Luther-Universität Halle-Wittenberg, D-06099 Halle (Saale), Germany

³Department of Physical and Chemical Sciences, University of L'Aquila, Via Vetoio 10, I-67010 L'Aquila, Italy

(Received 30 April 2013; published 31 July 2013)

By means of a comprehensive theoretical investigation, we show that external pressure can induce topological phase transitions in IV–VI semiconducting chalcogenides with a rocksalt structure. These materials satisfy mirror symmetries that are needed to sustain topologically protected surface states, at variance with time-reversal symmetry that is responsible for gapless edge states in \mathcal{Z}_2 topological insulators. The band inversions at high-symmetry points in the Brillouin zone that are related by mirror symmetry are brought about by an “asymmetric” hybridization between cation and anion *sp* orbitals. By working out the microscopic conditions to be fulfilled in order to maximize this hybridization, we identify materials in the rocksalt chalcogenide class that are prone to undergo a topological phase transition induced by pressure and/or alloying. Our model analysis is fully confirmed by complementary advanced *first-principles* calculations and *ab initio*-based tight-binding simulations.

DOI: [10.1103/PhysRevB.88.045207](https://doi.org/10.1103/PhysRevB.88.045207)

PACS number(s): 73.20.At, 71.20.Nr, 71.70.Ej

I. INTRODUCTION

Semiconducting IV–VI chalcogenides CA ($C = \text{Ge, Sn, Pb}$ and $A = \text{S, Se, Te}$) represent an attractive class of materials, due to their unique structural and electronic properties. The most interesting compounds—SnTe, GeTe, and the lead chalcogenides PbA—display a rocksalt structure.¹ Both SnTe and GeTe have been long known for their ferroelectric properties in the low-temperature distorted structure,² whereas PbA possess potential relevance for thermoelectric and optoelectronic applications³. Their outstanding properties have been characterized by a variety of experimental techniques.^{3,4} In parallel, a large number of theoretical investigations, carried out with different methods ranging from tight-binding (TB) to density-functional theory (DFT) calculations, have addressed their peculiar electronic structure.^{5–10} Interest in this material class has been renewed because of relativistic effects that are relevant for future spintronic devices. For example, a giant Rashba effect has been predicted in the ferroelectric phase of bulk GeTe,¹¹ while SnTe is a topological crystalline insulator (TCI) with spin-polarized surface states.^{12,13} These observations motivated us to investigate the possibility of topological phase transitions in this class of narrow-gap semiconductors.

In the \mathcal{Z}_2 class of topological insulators (TIs), time-reversal symmetry ensures topologically protected edge states.^{14,15} An odd number of Dirac cones pinned at time-reversal-invariant momenta (TRIM), as found, e.g., in $\text{Bi}_{1-x}\text{Sb}_x$ and Bi_2Se_3 ,^{14,15} distinguishes a \mathcal{Z}_2 TI from a conventional band insulator. In contrast, crystal symmetries play a central role in the class of TCIs.^{16,17} Beside symmetry requirements, band inversions in the bulk insulating electronic structure and strong spin-orbit coupling (SOC) are needed for metallic surface states to appear. In face-centered-cubic (fcc) TCIs, a mirror symmetry causes the appearance of an even number of Dirac cones on surfaces preserving the symmetry [see Figs. 1(a) and 1(b)]. These cones are situated off the TRIM \bar{X} within the $\bar{\Gamma}$ - \bar{X} line of the surface Brillouin zone.¹² Since all members of the cubic IV–VI class share the same crystal symmetries, all of them and their alloys may be prone to topological phase transitions. Such transitions, characterized by a nonzero mirror Chern number,^{12,18} have been proposed for PbTe and

PbSe under pressure,^{10,12} and were experimentally observed in ternary alloys $\text{Pb}_{1-x}\text{Sn}_x(\text{Se, Te})$ as a function of doping.^{19–22} These findings are not simply explained by the SOC strength: Although SOC in Pb ($Z = 82$) is larger than in Sn ($Z = 50$), PbTe is nonetheless a conventional band insulator, as opposed to the TCI SnTe. This clearly calls for a deeper understanding of the microscopic origin of the band inversions.

In this paper we show that in principle all members of the rocksalt chalcogenide class can be turned into TCIs under pressure, with the only exception of GeTe. The methods used comprise advanced *first-principles* simulations and *ab initio*-based TB calculations. Consistent with sophisticated *GW* computations,¹⁰ we find that the fundamental gap of lead chalcogenides shrinks upon applying external pressure, closes at a critical pressure, and subsequently reopens with an inverted band character. This behavior is typical of a topological phase transition and is exemplified for PbTe in Fig. 2, where a relativistic TB scheme⁶ for the semi-infinite system was used.^{23,24} As long as the fcc structure is preserved, these band inversions cause metallic surface states [Fig. 2(c)].

To benchmark the reliability of our predictions, we performed accurate DFT calculations with hybrid functionals,²⁵ as implemented in VASP.^{26–28} These improve significantly with respect to local-density or generalized-gradient approximations, especially for narrow-gap semiconductors.^{9,29} For PbTe, we find the fundamental band gap at L to close at a volume ratio of $V/V_0 = 0.91$ [V_0 is the equilibrium volume; see also Fig. 2(b)] that is accompanied by band inversion (Fig. 3). This finding corroborates the topological phase transition deduced from TB calculations (cf. Fig. 2). At variance with PbTe, hole pockets appear in the electronic structure of GeTe, concomitantly with the pressure-induced closure of the fundamental gap, thus triggering a semimetallic state instead of a TCI. These essential differences require clarification in a microscopic picture.

II. SEMI-EMPIRICAL DISCUSSION

Many peculiar electronic properties of PbA were resolved by noting that the Pb-6s band lies below the top of the valence band. The existence of an occupied cation-*s* band

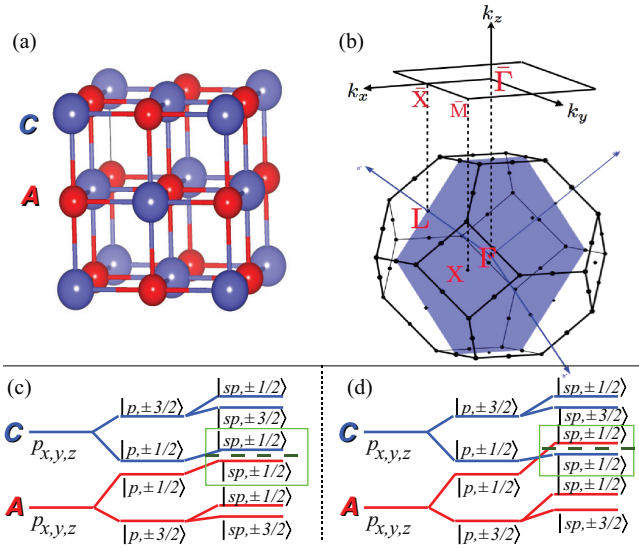


FIG. 1. (Color online) (a) Crystal structure and (b) Brillouin zone of rocksalt chalcogenides, showing one mirror plane (green) containing the high-symmetry points $\bar{\Gamma}$, \bar{L} , and \bar{X} as well as their projection onto the [001] surface. Schematic representation of the band structure at the L point in the topologically trivial phase (c) and upon pressure-induced enhancement of sp hybridization (d). Dashed lines separate occupied from unoccupied energy levels.

leads to strong level repulsion at L , explaining the narrow band gap E_g and its unusual ordering within the series.^{8,9} The central role of s electrons can be deduced within the framework of linear combinations of atomic orbitals.³⁰ The only nonzero matrix elements at L in the nearest-neighbor approximation are those describing the hybridization between cation (anion) s and anion (cation) p states. Because of SOC, this hybridization close to the Fermi energy involves mainly a combination of atomlike p states on C and A sites, with a total angular momentum $j = 1/2$, namely, $|\pm 1/2\rangle = (|p_x, \mp 1/2\rangle \pm i |p_y, \mp 1/2\rangle + |p_z, \pm 1/2\rangle)/\sqrt{3}$, and energies $\bar{\epsilon}_{p,A(C)} = \epsilon_{p,A(C)} \pm 2\lambda_{A(C)}$; here, $\epsilon_{p,A(C)}$ and $\lambda_{A(C)}$ are the orbital energy and the SOC constant of the C (A) ion, respectively. In the atomic limit, corresponding to the topologically trivial phase, $\Delta_0 \equiv \bar{\epsilon}_{p,C} - \bar{\epsilon}_{p,A} > 0$ means occupied A and unoccupied C p shells [Fig. 1(c)]. The hybridization with the s states pushes both C and A p levels to higher energies; this energy shift is roughly proportional to the squared effective hopping interaction t_{sp} and inversely proportional to the energy differences $\Delta_1 \equiv \bar{\epsilon}_{p,C} - \epsilon_{s,A}$ and $\Delta_2 \equiv \bar{\epsilon}_{p,A} - \epsilon_{s,C}$. The energy gap at L can then be approximated as $E_g \approx \Delta_0 + 10t_{sp}^2(\Delta_1^{-1} - \Delta_2^{-1})/3$. Hence, for band inversion to occur, two conditions have to be satisfied: (1) The energy separation Δ_0 between p states must be sufficiently small, and (2) the sp hybridization should be strongly “asymmetric.” This asymmetry is realized if $\Delta_1 \gg \Delta_2$, i.e., if the cation (anion) s level is energetically close to (far from) the anion (cation) p states.

The band gap is directly related to the $\vec{k} \cdot \vec{p}$ Hamiltonian at L , $\hat{H} = m\sigma_z$; $\sigma_z = \pm 1$ corresponds to the p character on C and A sites, respectively. A negative $m \equiv E_g/2$ implies that conduction and valence bands at L derive respectively from A

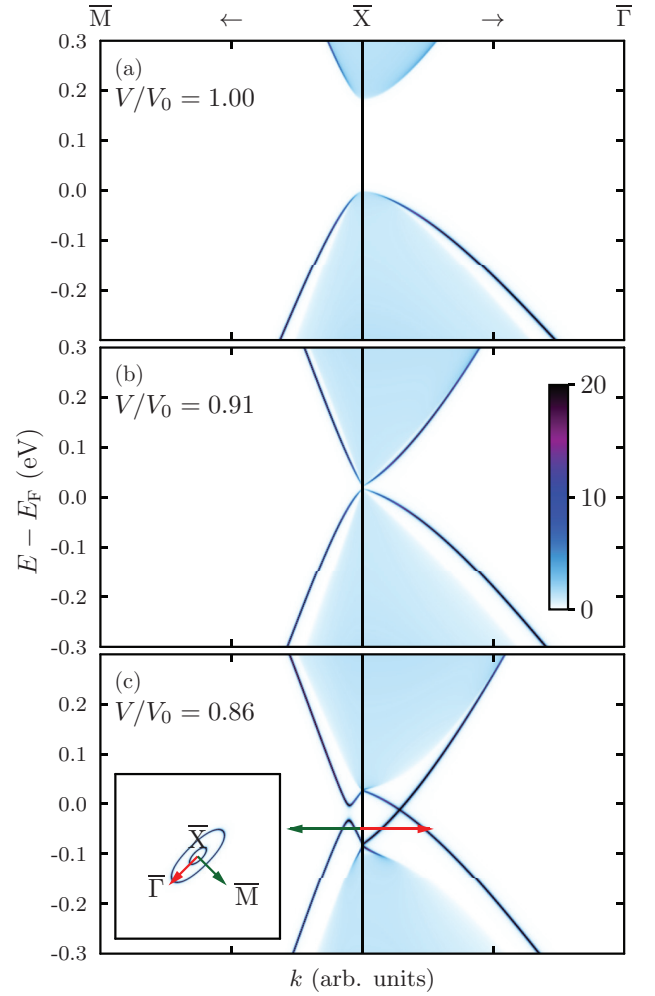


FIG. 2. (Color online) Topological phase transition in PbTe upon pressure, calculated by a TB method. For selected volume ratios V/V_0 , the spectral density of the topmost layer of the (001) surface is represented in a color scale [(b), in states/eV]. Topological trivial phases with mirror Chern number 0 appear for the equilibrium volume (a) and close to the critical pressure (b). A topological nontrivial phase (c) shows a mirror Chern number of -2 . Its Dirac surface state is depicted in a constant-energy cut around \bar{X} at $E_F - 0.05$ eV [inset in (c)]. A k path shown also in (c) is marked by arrowed lines. The k axis common to (a)–(c) shows $2/5$ of the \bar{M} – \bar{X} and \bar{X} – $\bar{\Gamma}$ lines around \bar{X} [cf. Fig. 1(b)].

and C ions. A reversal of m in the presence of the fcc-structure mirror symmetries implies a topological phase transition with an associated change of the mirror Chern number.¹² A large SOC is required to fulfill the first condition. The second condition, on the other hand, could in principle be controlled by alloying ternary solid solutions $C_xC'_{1-x}A$ (along the path pursued in Refs. 19–22) or $CA_xA'_{1-x}$.³¹ Because the band inversion is proportional to the strength of the sp hybridization, $t_{sp} \propto d^{-2}$, a straightforward way to induce a topological phase transition is to apply external pressure.^{10,12,30}

Guided by these considerations, we performed an empirical screening within the rocksalt chalcogenide class, using different TB and *ab initio*-based TB parametrizations^{6,30,32} (Table I). Trends are consistent and allow to loosely identify three

TABLE I. Estimated relevant quantities from Harrison's (Ref. 30) and Lent's (Ref. 6, in brackets) parametrizations. Values in square brackets were obtained from first principles by projecting DFT bands on a TB model using maximally localized Wannier-functions (Ref. 32). SOC and lattice constants a_0 are taken from Refs. 33 and 1, respectively.

	PbTe	SnTe	PbS	PbSe	GeTe
Δ_0 (eV)	0.71 (1.72) [2.68]	1.35 (0.95) [1.8]	3.15 (3.92) [4.72]	2.09 (3.29) [4.00]	1.19 (0.28) [1.64]
Δ_1 (eV)	10.08 (12.70) [12.16]	10.71 (13.13) [11.31]	13.77 (16.25) [15.21]	13.29 (15.75) [15.10]	10.55 (11.92) [10.29]
Δ_2 (eV)	4.32 (7.16) [5.80]	4.75 (6.69) [5.44]	1.89 (5.59) [4.37]	2.95 (5.18) [4.84]	6.63 (8.51) [5.68]
a_0 (Å)	6.462	6.327	5.936	6.124	6.009

subclasses: (i) The first subclass, comprising PbTe and SnTe, is characterized by a relatively small Δ_0 (mainly due to the large λ_{Te}) and similar differences $\Delta_1^{-1} - \Delta_2^{-1}$. In this respect, the main reason why SnTe is a TCI but PbTe is not could be the smaller equilibrium volume of the former with respect to the latter. In turn, a relatively small pressure could tune the topological transition in PbTe,¹² and the doping-dependent topological transition in $\text{Pb}_{1-x}\text{Sn}_x\text{Te}$ could be ascribed to a

(chemical) pressure effect. (ii) The second subclass comprises PbS and PbSe and shows Δ_0 's approximately twice as large as those of the first subclass, due to smaller λ_A . However, Δ_2 is much smaller than Δ_1 ; it is thus very likely that a reduction of the lattice constant and the associated increase of t_{sp} could result in band inversion (due to the strongly asymmetric sp hybridization) and, hence, in a topological phase transition. (iii) GeTe, belonging to the third class, even though displaying

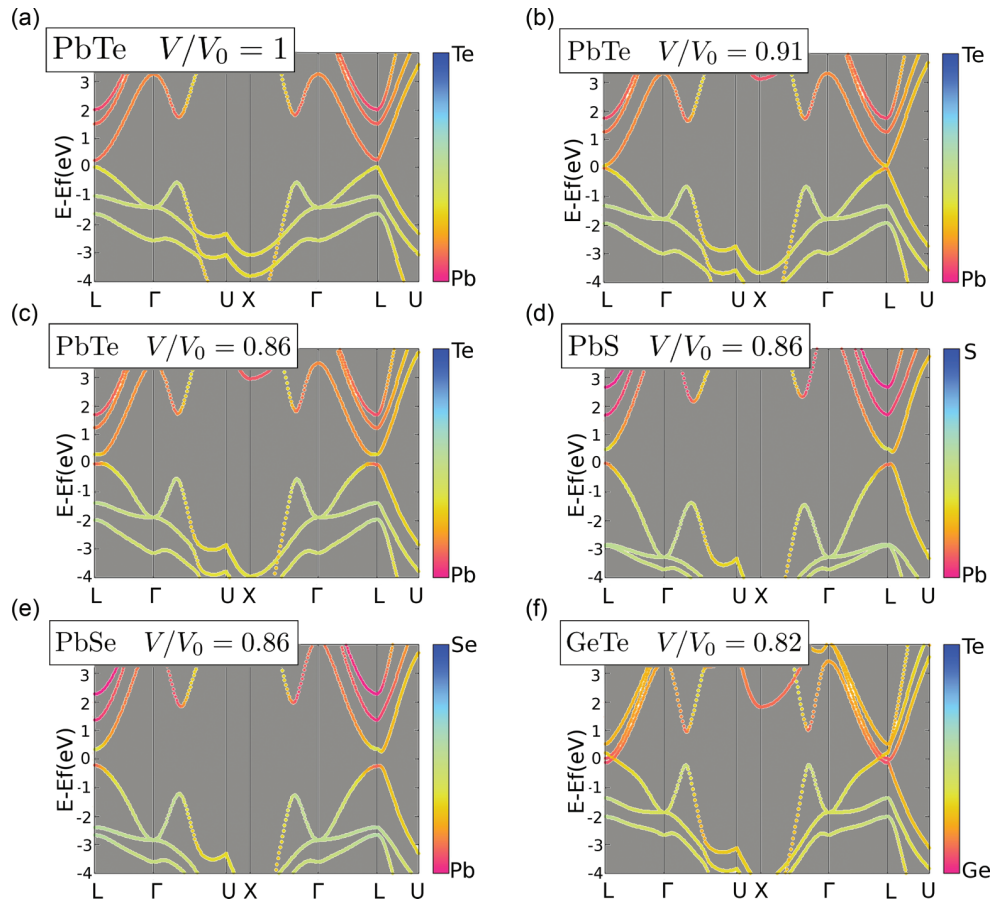


FIG. 3. (Color online) DFT electronic structures of selected rocksalt chalcogenides for different volume ratios V/V_0 , with band characters highlighted by a color scale (anions: blue; cations: red).

a small Δ_0 , does not seem to fulfill condition (2) above. Thus, a reopening of the gap is unlikely and a transition to a metallic state is expected upon applying pressure (Fig. 3).

III. RESULTS

Our DFT calculations confirm this scenario. The band inversion is highlighted for PbA at selected volumes (Fig. 3). For PbTe, the closure of the band gap shows up at a critical volume of $0.92V_0$; hence, the band inversion has already occurred at a volume ratio $V/V_0 = 0.91$ (pressure ~ 4 GPa), with a predominant Te character in the conduction band at L . The negative gap increases upon further decreasing the volume ($V/V_0 = 0.86$ in Fig. 3). Indeed, the atomic and orbital resolved character of the valence (conduction) band at L shows a predominant Pb- s and Te- p (Pb- p and Te- s) contribution at V_0 , whereas an opposite character appears below the critical volume.³⁴ The same trend with pressure holds for both PbS and PbSe, with critical volumes of about $0.94V_0$ and $0.96V_0$ (TB: $0.91V_0$ and $0.96V_0$; pressure 4.2–6.3 and ~ 2.4 GPa), respectively. The predicted critical pressures can be compared with those at which PbA undergo structural transitions, hence losing the fcc-structure symmetry required for the TCI transition; these are 2.98 GPa,³⁵ 6.01 GPa,³⁶ and 6.05 GPa (Ref. 37) for $A = S, Se, Te$, respectively. Hence, in principle, the topological transition may be observed in high-pressure experiments on PbSe and PbTe, for which structural transitions happen at higher pressures than the predicted critical ones. For GeTe, on the other hand, the gap closes at a critical volume of $0.9V_0$ (pressure ~ 5 GPa). This finding is consistent with the smaller hybridization asymmetry. Furthermore, since the $j = 1/2$ and $j = 3/2$ manifolds in the conduction bands are close in energy due to small λ_{Ge} , a further increase of pressure pushes them both below the anion p states, thus turning GeTe into a semimetal (Table I and Fig. 3).

To provide further support for the pressure-induced topological phase transitions, we performed relativistic TB calculations for bulk PbTA and GeTe. The mirror Chern number is computed in the spirit of the spin Chern number.³⁸ Since the Bloch states are eigenstates of both the Hamiltonian and the mirror operator,³⁹ we separate them into two categories

with mirror eigenvalues $\pm i$ and calculate the Berry curvature for both. The integral of the Berry curvature over the intersection of the mirror plane with the Brillouin zone yields Chern numbers $n_{\pm i}$, from which the mirror Chern number $c_m \equiv (n_{+i} - n_{-i})/2$ is obtained.¹⁸ While GeTe is always topologically trivial, we find a mirror Chern number of -2 for band-inverted PbA. In summary, the numerical calculations corroborate the microscopic picture derived above.

IV. CONCLUSIONS

In conclusion, we have shown that a strongly asymmetric sp hybridization and a sizable SOC are necessary conditions for band inversions to occur at the L points and the related TCI state to arise in rocksalt chalcogenides. By performing a thorough analysis of pressure effects in the entire family of fcc chalcogenides, we verify the topological nature of the transition, as shown by nonzero mirror Chern numbers and gapless edge states at (001) surfaces. In principle, the predicted TCI transition may be experimentally investigated in PbTe and PbSe by using infrared or Raman spectroscopy, as recently proposed for pressure-induced transitions of \mathbb{Z}_2 topological order.^{40,41} Furthermore, we suggest that topologically trivial lead chalcogenides could be turned into a topologically nontrivial state upon a combination of applied pressure and alloying *through anion substitution*, a yet unexplored path to engineer a TCI.⁴² This scenario may be relevant for the experimental search of conducting edge states, as the carrier concentration, largely determined by the presence of cation or anion vacancies, can be easily controlled in lead chalcogenides during the crystal growth,³ as opposed to SnTe, where a high concentration of cation vacancies is frequently found, resulting in an undesirable p -type degenerate conducting behavior.

ACKNOWLEDGMENTS

This work is supported by the Priority Program 1666 “Topological Insulators” of the DFG. We acknowledge PRACE for awarding us access to resource MareNostrum based in Spain at Barcelona Supercomputing Center (BSC-CNS).

¹*Semiconducting II–VI, IV–VI, and V–VI Compounds*, edited by N. K. Abrikosov, V. F. Bankina, L. V. Poretskaya, L. E. Sheliniova, and E. V. Shudnova (Plenum, New York, 1968).

²M. E. Lines and A. M. Glass, *Principles and Applications of Ferroelectrics and Related Materials* (Clarendon, Oxford, UK, 1977).

³*Lead Chalcogenides: Physics and Applications*, edited by D. Khokhlov (Taylor & Francis, New York, 2003).

⁴R. Dornhaus and G. Nimitz, in *Narrow-Gap Semiconductors*, Springer Tracts in Modern Physics Vol. 98, edited by G. Höhler (Springer-Verlag, Berlin, 1983), pp. 119–300.

⁵D. L. Mitchell and R. F. Wallis, *Phys. Rev.* **151**, 581 (1966).

⁶C. S. Lent, M. A. Bowen, J. D. Dow, and R. S. Allgaier, *Superlattices Microstruct.* **2**, 491499 (1986).

⁷M. Lach-hab, D. A. Papaconstantopoulos, and M. J. Mehl, *J. Phys. Chem. Solids* **63**, 833 (2002).

⁸S.-H. Wei and A. Zunger, *Phys. Rev. B* **55**, 13605 (1997).

⁹K. Hummer, A. Grüneis, and G. Kresse, *Phys. Rev. B* **75**, 195211 (2007).

¹⁰A. Svane, N. E. Christensen, M. Cardona, A. N. Chantis, M. van Schilfhaar, and T. Kotani, *Phys. Rev. B* **81**, 245120 (2010).

¹¹D. Di Sante, P. Barone, R. Bertacco, and S. Picozzi, *Adv. Mater.* **25**, 509 (2013).

¹²T. H. Hsieh, H. Lin, J. Liu, W. Duan, A. Bansil, and L. Fu, *Nat. Commun.* **3**, 982 (2012).

¹³Y. Tanaka, Z. Ren, K. Nakayama, S. Souma, T. Takahashi, K. Segawa, and Y. Ando, *Nat. Phys.* **8**, 800 (2012).

¹⁴H. Hasan and C. Kane, *Rev. Mod. Phys.* **82**, 3045 (2010).

- ¹⁵M. Z. Hasan and J. E. Moore, *Annu. Rev. Condens. Matter Phys.* **2**, 55 (2011).
- ¹⁶L. Fu, *Phys. Rev. Lett.* **106**, 106802 (2011).
- ¹⁷R. J. Slager, A. Mesaros, V. Juričić, and J. Zaanen, *Nat. Phys.* **9**, 98 (2013).
- ¹⁸J. C. Y. Teo, L. Fu, and C. L. Kane, *Phys. Rev. B* **78**, 045426 (2008).
- ¹⁹P. Dziawa, B. J. Kowalski, K. Dybko, R. Buczko, A. Szczerbakow, M. Szot, E. Łusakowska, T. Balasubramanian, B. M. Wojek, M. H. Berntsen *et al.*, *Nat. Mater.* **11**, 1023 (2012).
- ²⁰B. M. Wojek, R. Buczko, S. Safaei, P. Dziawa, B. J. Kowalski, M. H. Berntsen, T. Balasubramanian, M. Leandersson, A. Szczerbakow, P. Kacman *et al.*, *Phys. Rev. B* **87**, 115106 (2013).
- ²¹S.-Y. Xu, C. Liu, N. Alidoust, M. Neupane, D. Qian, I. Belopolski, J. D. Denlinger, Y. J. Wang, H. Lin, L. A. Wray *et al.*, *Nat. Commun.* **3**, 1192 (2012).
- ²²Y. Tanaka, T. Sato, K. Nakayama, S. Souma, T. Takahashi, Z. Ren, M. Novak, K. Segawa, and Y. Ando, *Phys. Rev. B* **87**, 155105 (2013).
- ²³J. Henk and W. Schattke, *Comput. Phys. Commun.* **77**, 69 (1993).
- ²⁴A. Bödicker, W. Schattke, J. Henk, and R. Feder, *J. Phys.: Condens. Matter* **6**, 1927 (1994).
- ²⁵J. Heyd, G. E. Scuseria, and M. Ernzerhof, *J. Chem. Phys.* **121**, 1187 (2004).
- ²⁶G. Kresse and J. Furthmüller, *Phys. Rev. B* **54**, 11169 (1996).
- ²⁷G. Kresse and J. Furthmüller, *Comput. Mater. Sci.* **6**, 15 (1996).
- ²⁸Kohn-Sham equations were solved using the projector augmented-wave method. The energy cutoff for the plane-wave expansion was 600 eV; an $8 \times 8 \times 8$ Monkhorst-Pack k -point grid was used. Calculations with the hybrid Heyd-Scuseria-Ernzerhof (HSE) functional (Ref. 25) are computationally very demanding and thus were used for bulk states only.
- ²⁹For instance, LDA calculations predicted a negative pressure dependence of the lead chalcogenide band gap, which would suggest an inverted band structure at L . However, GW calculations have shown that this inversion is a spurious outcome of the local approximation for the exchange-correlation potential, which is known to place the conduction band too low in energy (that is, too small a band gap) (Ref. 10).
- ³⁰W. Harrison, *Electronic Structure and the Properties of Solids* (Freeman, San Francisco, 1980).
- ³¹In fact, all energy differences are expected to change; within the virtual-crystal approximation (VCA) one has $\Delta_i = x\Delta_i^{CA} + (1-x)\Delta_i^{C'A(C'A')}$.
- ³²A. A. Mostofi, J. R. Yates, Y.-S. Lee, I. Souza, D. Vanderbilt, and N. Marzari, *Comput. Phys. Commun.* **178**, 685 (2008).
- ³³M. Montalti, A. Credi, L. Prodi, and M. T. Gandolfi, *Handbook of Photochemistry*, 3rd ed. (CRC, Boca Raton, FL, 2006).
- ³⁴When projecting wave functions at L within muffin-tin spheres with radius = 1.73 Å and 1.54 Å for Pb and Te, respectively, the weights on Pb- s , Pb- p , Te- s , and Te- p are 0.24, 0.0, 0.0, and 0.36 for the valence band maximum (VBM), and 0.0, 0.36, 0.06, and 0.0 for the conduction band minimum (CBM) at the equilibrium volume for PbTe, whereas we find 0, 0.36, 0.06, and 0 for the VBM and 0.29, 0.0, 0.0, and 0.11 for the CBM at $V/V_0 = 0.86$.
- ³⁵X. Zhou, D. He, S. Wang, H. Wang, J. Zhang *et al.*, *J. Appl. Phys.* **113**, 043509 (2013).
- ³⁶S. V. Ovsyannikov, V. V. Shchennikov, A. Y. Manakov, A. Y. Likhacheva, I. F. Berger *et al.*, *Phys. Status Solidi B* **244**, 279 (2007).
- ³⁷V. V. Shchennikov, S. V. Ovsyannikov, Yu. A. Manakov, Yu. A. Likhacheva, A. I. Ancharov *et al.*, *JETP Lett.* **83**, 228 (2006).
- ³⁸E. Prodan, *Phys. Rev. B* **80**, 125327 (2009).
- ³⁹T. Inui, Y. Tanabe, and Y. Onodera, *Group Theory and Its Applications in Physics*, Springer Series in Solid State Sciences Vol. 78 (Springer, Berlin, 1990).
- ⁴⁰A. Bera, K. Pal, D. V. S. Muthu, S. Sen, P. Guptasarma, U. V. Waghmare, and A. K. Sood, *Phys. Rev. Lett.* **110**, 107401 (2013).
- ⁴¹X. Xi, C. Ma, Z. Liu, Z. Chen, W. Ku *et al.*, [arXiv:1305.0959](https://arxiv.org/abs/1305.0959); M. K. Tran, J. Levallois, P. Lerch, J. Teyssier, A. B. Kuzmenko *et al.*, [arXiv:1305.5485](https://arxiv.org/abs/1305.5485).
- ⁴²For instance, in the $\text{PbSe}_x\text{Te}_{1-x}$ alloy, one expects an effect of chemical pressure [$a_0(\text{PbSe}) \ll a_0(\text{PbTe})$] and of the band shifts. The latter “asymmetrize” the hopping interactions, so that for a doping of $x = 0.2$ one would get $\Delta_0 = 1$ eV, $\Delta_1 = 10.72$ eV, $\Delta_2 = 4.04$ eV, and $a_0 = 6.39$ Å in the VCA. Also on the basis of the smaller critical pressure predicted for PbSe with respect to PbTe, a topological transition is therefore likely to occur at reasonable values of applied pressure.

6.3 DUAL TOPOLOGICAL CHARACTER OF CHALCOGENIDES: THEORY FOR Bi_2Te_3

The next publication [TR2] was motivated by unclear results of different groups concerning the splitting of the Dirac point of a \mathcal{Z}_2 TI when doped by magnetic impurities. For example, Chen *et al.* [122] presented a clear evidence of Dirac cone splitting in Fe doped Bi_2Se_3 , but Schlenk *et al.* [123] found no splitting in the ARPES spectra measured on their probes of the same material. In our work we have shown that the magnetic ordering of the impurities is crucial for the behaviour of the surface state band structure, the possible effects ranging from splitting of the Dirac cone to an unsplit but shifted Dirac point, thus possibly explaining both of the experimental results.

Instead of modelling magnetic impurities with the CPA or in a supercell, the effect of magnetism was simulated by an exchange term in the TB model, having the same effect as an effective external magnetic field. The TI studied was Bi_2Te_3 and the effective magnetic field was chosen to be oriented in different directions, especially parallel and perpendicular to the considered mirror planes of Bi_2Te_3 .

In a clean system, not only TRS but also other symmetries of the point group of the crystal are present. This consideration leads to the fact that time-reversal symmetric TIs do not belong only to one topological \mathcal{Z}_2 class but they can also be TCIs. Bi_2Te_3 possesses three non-equivalent mirror planes perpendicular to the (111) surface. The mirror Chern number for these planes reads $n_M = -1$, in consonance with the fact that there is one surface state at the $\bar{\Gamma}$ point of the surface BZ of the (111) surface. We called such TIs *dual* because of their affiliation to the two distinct groups of TIs.

Applying a magnetic field to the TI breaks the TRS and makes it impossible to calculate the \mathcal{Z}_2 invariant, which is not even defined in this case. But in a special case, in which the magnetic field is oriented perpendicular to a mirror plane, it is possible to calculate the mirror Chern number, since the mirror symmetry is preserved in this case. The result is again $n_M = -1$, indicating that there should be no splitting of the Dirac point for this magnetic field orientation. This was also shown by calculating the surface electronic structure.

A splitting of the Dirac point is possible when both the mirror symmetry and TRS are broken, e.g. by a magnetic field oriented not perpendicular to the mirror plane. These findings lead to the conclusion that it is important to investigate the possible ordering of the magnetic impurities in order to understand their influence on the surface states of the TI.

Dual Topological Character of Chalcogenides: Theory for Bi_2Te_3

Tomáš Rauch,¹ Markus Flieger,¹ Jürgen Henk,¹ Ingrid Mertig,^{1,2} and Arthur Ernst²
¹*Department of Physics, Martin Luther University Halle-Wittenberg, 06099 Halle, Germany*
²*Max Planck Institute of Microstructure Physics, 06120 Halle, Germany*

(Received 23 July 2013; published 7 January 2014)

A topological insulator is realized via band inversions driven by the spin-orbit interaction. In the case of \mathcal{Z}_2 topological phases, the number of band inversions is odd and time-reversal invariance is a further unalterable ingredient. For topological crystalline insulators, the number of band inversions may be even but mirror symmetry is required. Here, we prove that the chalcogenide Bi_2Te_3 is a dual topological insulator: it is simultaneously in a \mathcal{Z}_2 topological phase with \mathcal{Z}_2 invariants $(\nu_0; \nu_1\nu_2\nu_3) = (1; 000)$ and in a topological crystalline phase with mirror Chern number -1 . In our theoretical investigation we show in addition that the \mathcal{Z}_2 phase can be broken by magnetism while keeping the topological crystalline phase. As a consequence, the Dirac state at the (111) surface is shifted off the time-reversal invariant momentum $\bar{\Gamma}$; being protected by mirror symmetry, there is no band gap opening. Our observations provide theoretical groundwork for opening the research on magnetic control of topological phases in quantum devices.

DOI: 10.1103/PhysRevLett.112.016802

PACS numbers: 73.20.At, 71.70.Ej, 75.70.Rf

Introduction.— \mathcal{Z}_2 topological insulators are band insulators featuring surface states that are spin polarized and cross the fundamental band gap [1,2]. This is a consequence of an odd number of inversions of bulk bands that are driven by the spin-orbit interaction alone or in combination with crystal lattice distortions [3–5] or chemical disorder [6,7]. The odd number of bulk-band inversions distinguishes a \mathcal{Z}_2 topological insulator phase from a conventional band insulator phase, as has been proven for the \mathcal{Z}_2 topological insulators $\text{Bi}_x\text{Sb}_{1-x}$ and the chalcogenides Bi_2Se_3 , Sb_2Te_3 and Bi_2Te_3 [6,8,9]. The Dirac surface state of a \mathcal{Z}_2 topological insulator is located at a time-reversal invariant momentum (TRIM) of the two-dimensional Brillouin zone. Since it is protected by time-reversal symmetry, the surface state is robust against time-reversal-invariant perturbations (e.g., nonmagnetic adatoms).

Narrow band gap semiconductors, like SnTe, show an even number of band inversions [10] and, thus, do not belong to the \mathcal{Z}_2 topological class ($\nu_0 = 0$). However, they show a Dirac surface state that is protected by crystal symmetry, rather than by time-reversal symmetry. Hence, they belong to the class of topological crystalline insulators [11]; their mirror Chern number is -2 [10,12]. The two Dirac surface states are located within a mirror plane perpendicular to the surface but not necessarily at a TRIM of the two-dimensional Brillouin zone.

An insulator that belongs simultaneously to the \mathcal{Z}_2 phase and to the topological crystalline phase—a *dual* topological insulator—would allow us to manipulate its topological phase, and consequently its conducting Dirac surface state, by magnetism, either by an external magnetic field or by doping with magnetic atoms. Applying a magnetic field perpendicular to a mirror plane of the crystal lattice would on one hand break time-reversal symmetry and, as a

consequence, destroy the \mathcal{Z}_2 topological phase. On the other hand, the mirror symmetry is maintained and the topological crystalline phase is kept. The Dirac surface state that is still protected by mirror symmetry would be shifted off the TRIM, without opening of a band gap (Fig. 1). Applying a magnetic field with a component within the mirror plane would destroy both the \mathcal{Z}_2 phase and the topological crystalline phase; a band gap will open up in the Dirac state, leading to a conventional insulator phase [13].

In this Letter, we prove that the exemplary chalcogenide Bi_2Te_3 is such a *dual* topological insulator: besides being in its well-established \mathcal{Z}_2 phase, it is simultaneously in the topological crystalline phase. Teo *et al.* have predicted that $\text{Bi}_{1-x}\text{Sb}_x$ is a dual topological insulator [6]. On top of this, we show by theoretical electronic structure calculations that the above sketched scenario of magnetic control of topological phases holds. Furthermore, Bi_2Te_3 has \mathcal{Z}_2 invariants of $(\nu_0; \nu_1\nu_2\nu_3) = (1; 000)$; consequently, a Dirac surface state would exist on any crystal truncation plane. In other words, a sphere made of Bi_2Te_3 would show a Dirac state anywhere on its surface. In contrast, a topological crystalline insulator would show a Dirac state only in surface planes normal to the mirror plane. Hence, a Bi_2Te_3 sphere in a magnetic field perpendicular to the mirror plane would host Dirac states only on circles that lie within the mirror plane.

\mathcal{Z}_2 invariant and mirror Chern number.—To prove that Bi_2Te_3 is a dual topological insulator we first calculate the \mathcal{Z}_2 invariant and the mirror Chern number for the bulk system, using a first-principles-based tight-binding method (see the Supplemental Material [14]). The \mathcal{Z}_2 invariants are computed to $(\nu_0; \nu_1\nu_2\nu_3) = (1; 000)$, in agreement with earlier calculations [8,15]. For the computation of the mirror Chern number [6], we consider a mirror plane

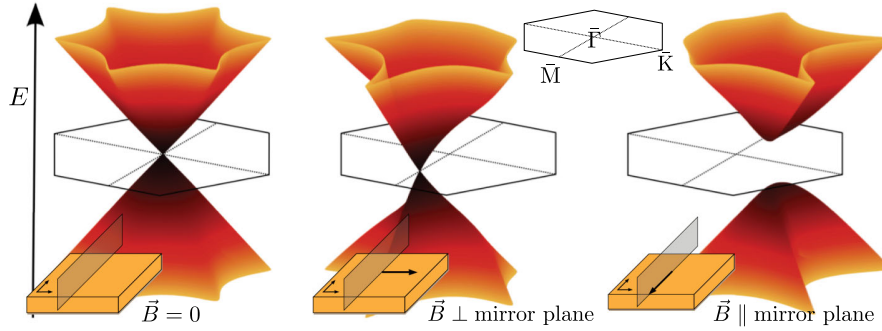


FIG. 1 (color online). Variation of a Dirac surface state's dispersion with respect to the topological phase (schematic): without magnetic field (left, $\vec{B} = 0$: dual topological insulator), with magnetic field perpendicular to a mirror plane (center, $\vec{B} \perp$ mirror plane: topological crystalline insulator), and with magnetic field within the mirror plane (right, $\vec{B} \parallel$ mirror plane: conventional insulator). The dispersions calculated from Fu's model [20] are shown in perspective view. The inset displays the surface Brillouin zone. The \bar{M} - $\bar{\Gamma}$ - \bar{M} direction lies within a mirror plane.

perpendicular to the (111) surface [like for the (001) surface of SnTe [10,16]; left in Fig. 2]. The mirror Chern number equals -1 and is interpreted as follows. On one hand, its modulus gives the number of nonequivalent Dirac surface states, as has been established in Ref. [6]; indeed, $\text{Bi}_2\text{Te}_3(111)$ hosts a single Dirac state. On the other hand, its sign gives the chirality of the spin texture of the Dirac surface state: the spin polarization of the Dirac states rotates clockwise about the surface normal at energies above the Dirac point. Already these findings prove that Bi_2Te_3 is a dual topological insulator, that is both a \mathcal{Z}_2 topological insulator and a topological crystalline insulator.

Now we show that the \mathcal{Z}_2 topological phase can be broken while keeping the topological crystalline phase. For

this purpose we mimicked an external magnetic field by adding a Zeeman term to the tight-binding Hamiltonian. In this case, time-reversal symmetry is broken [17] and a \mathcal{Z}_2 invariant cannot be defined. If the magnetic field (i.e., an axial vector) is perpendicular to the mirror plane, the reflection symmetry is maintained and the mirror Chern number is still computed to -1 , proving the topological crystalline phase. If the magnetic field lies within the mirror plane, both time-reversal and mirror symmetry are broken: neither the \mathcal{Z}_2 invariant nor the mirror Chern number can be defined in this case.

These findings suggest that the topological character of Bi_2Te_3 can be controlled by magnetism: from a dual topological insulator (no magnetic field) via a solely topological crystalline insulator (magnetic field perpendicular to mirror plane) to a conventional insulator (magnetic field within mirror plane).

Surface electronic structure.—The next step is to show how the Dirac surface state of Bi_2Te_3 is affected by the topological character. We computed the electronic structure of $\text{Bi}_2\text{Te}_3(111)$, using the tight-binding method and a renormalization scheme for semi-infinite systems [18]. Without magnetic field, the well-known Dirac surface state with its unique spin texture [15,19] has its Dirac point located very close to the valence band in the pocket at $\bar{\Gamma}$, the center of the surface Brillouin zone (right in Fig. 2). This electronic state is mostly affected by magnetism in an (E, k) region close to its Dirac point; hence, a zoom into this region is indispensable (rectangle in Fig. 2). In the following, we present exemplary results for a magnetic field with 0.03 eV Zeeman energy.

For a magnetic field \vec{B} perpendicular to the mirror plane, the surface state is shifted off the TRIM by $\delta k = 0.01 \text{ \AA}^{-1}$ (Fig. 3); this displacement lies within the mirror plane (here: k_y). There is no band gap opening [compare (e) and (f) in Fig. 3]; the Dirac point “survives,” which indicates a topological nontrivial phase. In contrast, the dispersion along the magnetic field (here: k_x , i. e., normal to the

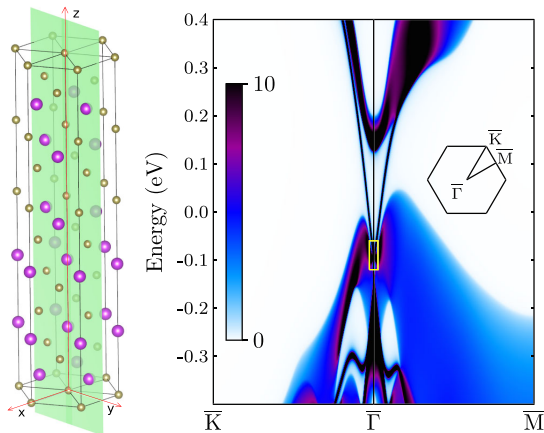


FIG. 2 (color online). Left: perspective view of Bi_2Te_3 . Each of the quintuple layers shown consists of two Bi atoms (large magenta spheres) and three Te atoms (small brown spheres). The shaded green area depicts the yz mirror plane of the crystal (z along [111]). Right: Dirac surface state in $\text{Bi}_2\text{Te}_3(111)$, obtained from tight-binding calculations. The spectral density of the topmost quintuple layer is shown as color scale (in states per eV) along a \bar{K} - $\bar{\Gamma}$ - \bar{M} path of the two-dimensional Brillouin zone (inset). The yellow rectangle highlights the (E, k) area addressed in Fig. 3.

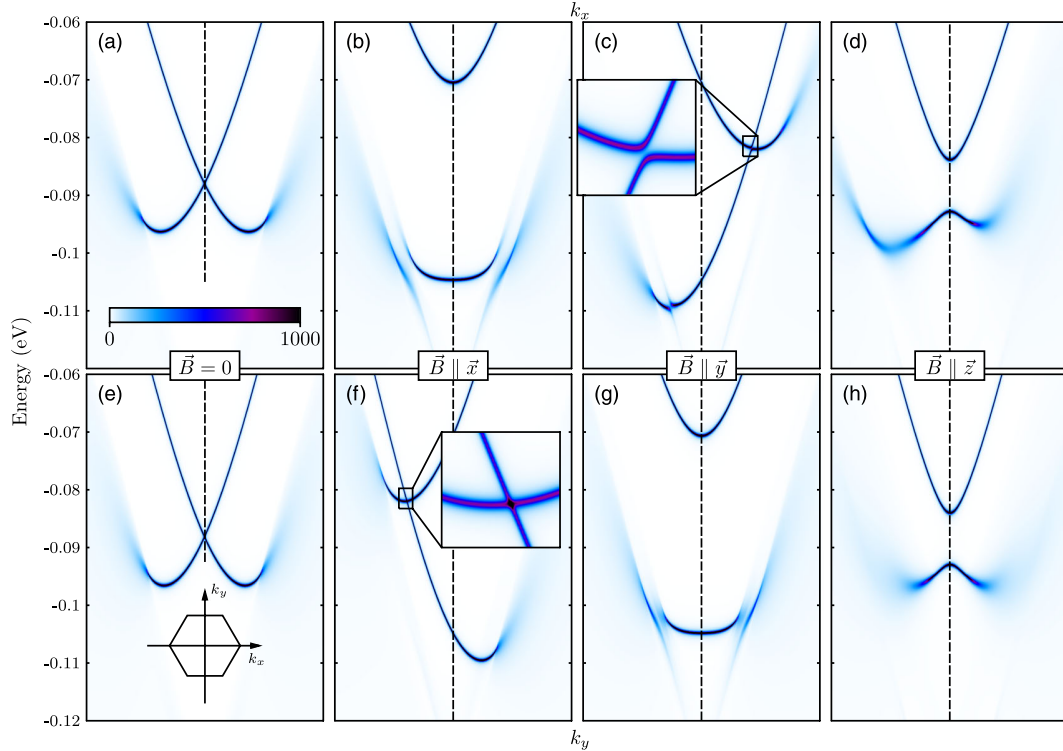


FIG. 3 (color online). Dispersion of the Dirac state at Bi_2Te_3 (111) for different magnetic configurations. Only a small part of the two-dimensional Brillouin zone (indicated in Fig. 2) is displayed (top row: k_x ; bottom row: k_y ; the respective zeroes are indicated by vertical dash-dotted lines). Without magnetic field [$\vec{B} = 0$, (a) and (e)], Bi_2Te_3 is in its dual topological phase (Dirac point at $\vec{k}_{\parallel} = 0$). For an in-plane magnetic field $\vec{B} \parallel \vec{x}$ [(b) and (f)] it stays in its topological crystalline phase; the inset in (f) zooms into the Dirac point shifted along k_y . For both $\vec{B} \parallel \vec{y}$ [(c) and (g)] and $\vec{B} \parallel \vec{z}$ [(d) and (h)] the topological phase is trivial: there is no Dirac point [cf. the zoom into the tiny band gap in (c)]. The color scale, in states per eV, displays the spectral density of the topmost quintuple layer. In regions in which the Dirac state hybridizes with bulk electronic states, the spectral density becomes blurred.

mirror plane) is gapped, with an energy splitting of about 34 meV [(b) in Fig. 3].

For \vec{B} within the mirror plane (here: normal to the surface, i.e., along the z direction), Bi_2Te_3 becomes a conventional insulator: a band gap opens in the entire Brillouin zone [panels (d) and (h) in Fig. 3]. The gap width is smallest at the “avoided Dirac point” at $\bar{\Gamma}$, with a magnitude of 9 meV.

For \vec{B} along the y direction (i.e., within both the surface plane and the mirror plane), a tiny gap shows up, with a width of 0.3 meV [panel (c) in Fig. 3]. Hence, also in this setup, Bi_2Te_3 is in principle a conventional insulator; however, the gap width is much smaller than the thermal energy of 25 meV at room temperature. Thus, this band gap is not relevant in device applications. A closer analysis reveals that this gap is due to spin-orbit coupling, while that for $\vec{B} \parallel \vec{z}$ is attributed to exchange splitting.

These electronic structure calculations for the (111) surface fully confirm the considerations based on the topological invariants. We provide further qualitative support by a model Hamilton operator for a two-dimensional electron gas [20] that has been extended to account for magnetism.

Model calculations.—To investigate the effect of the topological character on the Dirac state we derived a $\vec{k} \cdot \vec{p}$ model Hamilton operator [21]; magnetism is mimicked by a Zeeman term (see Supplemental Material [14]). This operator without the Zeeman term agrees within third order of the wave vector components with that derived by Fu [20].

The model Hamilton operator illustrates in the case of zero magnetic field the different dispersions of the Dirac state along the two different high symmetry lines $\bar{\Gamma}-\bar{M}$ and $\bar{\Gamma}-\bar{K}$ in the surface Brillouin zone, cf., the warping in Figs. 1 and 2. The spin structure of the Dirac state, especially the out-of-plane component, fits to experimental findings [9,22]. If magnetism is taken into account, the Hamilton operator is not invariant under time-reversal and one expects a gap to open up at the Dirac point (Fig. 1). However, for a magnetic field pointing perpendicular to a mirror plane, there is no gap but the Dirac point is shifted within the mirror plane. These findings are in line with the tight-binding calculations and corroborate the dual topological character of Bi_2Te_3 .

Because the magnetism-induced band gaps are small, the contours of the Dirac surface state in constant energy cuts

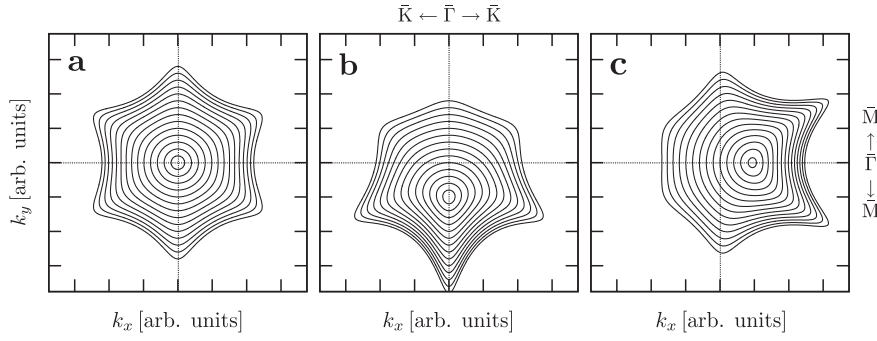


FIG. 4. Effect of a magnetic field on the dispersion of a Dirac state, obtained from a model calculation (schematic; see text). Constant energy contours are calculated (a) without magnetic field ($\vec{B} = 0$), (b) with magnetic field perpendicular to a mirror plane ($\vec{B} \parallel \vec{x}$), and (c) with magnetic field within the mirror plane ($\vec{B} \parallel \vec{y}$). The k_x (k_y) axis is along $\bar{K}-\bar{\Gamma}-\bar{K}$ ($\bar{M}-\bar{\Gamma}-\bar{M}$).

may be used as a signature for a shift of the Dirac point. These contours can be investigated in very high resolution photoelectron spectroscopy [23]. For $\vec{B} = 0$, the circular contours at energies close to the Dirac point become hexagonally warped at increased energies (Fig. 4a). These ‘snowflake’ shapes are distorted for in-plane magnetic fields [(b) and (c)] and show in addition centers shifted in direction perpendicular to \vec{B} .

Concluding remarks.—Our investigations prove theoretically that the topological character of dual topological insulators can be manipulated by magnetism: from the dual “ \mathcal{Z}_2 plus crystalline” phase via the topological crystalline phase to the conventional insulating phase. The associated opening of a band gap in the Dirac state could be exploited in device applications. Although our study provides strong support for this scenario—by means of model calculations and semi-empirical calculations for the realistic system Bi_2Te_3 —experimental verification is necessary, for example by means of photoelectron spectroscopy [24]. An alternative is Landau level spectroscopy [25] which has been applied to the Dirac surface state of Bi_2Se_3 [26] and to BiTeI [27].

Considering transport measurements, the dual topological character of $\text{Bi}_2\text{Te}_3(111)$ thin films suggests a new setup for the quantum anomalous Hall effect, as has been proposed by Liu *et al.* [28]. So far, it was believed the quantum anomalous Hall effect requires an external magnetic field perpendicular to the film to achieve an insulating state [29,30]. As shown by Liu and co-workers, an in-plane magnetic field also results in a nonzero Hall conductance, provided the field is not perpendicular to a mirror plane. If the field is in-plane and perpendicular to a mirror plane, Bi_2Te_3 is a topological crystalline insulator—shown in this Letter—and, as a consequence, the Dirac surface state is not gapped and the Hall conductance vanishes.

In this Letter, we consider magnetism brought about by an external magnetic field, resulting in small band gaps in the Dirac surface state (Fig. 3). In view of applications, larger gap widths are obtained by doping the topological

insulator with magnetic constituents [31,32]. By controlling the directions of the magnetic moments by an external magnetic field, the topological character can be varied from topologically crystalline to trivial, provided the doping maintains the mirror symmetry.

This work focuses on Bi_2Te_3 ; calculations of the topological invariants for the other chalcogenides— Sb_2Te_3 and Bi_2Se_3 —prove that these are also dual topological insulators. This is expected for they show the same crystal symmetry and the same topology of the bulk electronic structure (e.g., the band inversion at the Brillouin zone center).

A question arises whether there exist, besides the chalcogenides, other dual topological insulators. One might expect that each \mathcal{Z}_2 topological insulator with band inversions in a mirror plane could be a dual topological insulator. In a detailed theoretical investigation, Teo *et al.* have shown that $\text{Bi}_{1-x}\text{Sb}_x$ ($x > 0.03$) is a strong topological insulator with \mathcal{Z}_2 invariants (1;1 1 1) and mirror Chern number -1 [6].

This work is supported by the Priority Program 1666 of DFG.

-
- [1] H. Hasan and C. Kane, *Rev. Mod. Phys.* **82**, 3045 (2010).
 - [2] M. Z. Hasan and J. E. Moore, *Annu. Rev. Condens. Matter Phys.* **2**, 55 (2011).
 - [3] W. Feng, D. Xiao, J. Ding, and Y. Yao, *Phys. Rev. Lett.* **106**, 016402 (2011).
 - [4] Z. Zhu, Y. Cheng, and U. Schwingenschlögl, *Phys. Rev. B* **85**, 235401 (2012).
 - [5] H. Han, Y. Zhang, G. Y. Gao, and K. L. Yao, *Solid State Commun.* **153**, 31 (2013).
 - [6] J. C. Y. Teo, L. Fu, and C. L. Kane, *Phys. Rev. B* **78**, 045426 (2008).
 - [7] S. Chadov, J. Kiss, C. Felser, K. Chadova, D. Ködderitzsch, J. Minár, and H. Ebert, [arXiv:1207.3463v1](https://arxiv.org/abs/1207.3463v1).
 - [8] H. Zhang, C.-X. Liu, X.-L. Qi, Z. Fang, and S.-C. Zhang, *Nat. Phys.* **5**, 438 (2009).

- [9] D. Hsieh, Y. Xia, L. Qian, L. Wray, J. H. Dil, F. Meier, J. Osterwalder, L. Patthey, J. G. Checkelsy, N. P. Ong, A. V. Fedorov, H. Lin, A. Bansil, D. Grauer, Y. S. Hor, R. J. Cava, and M. Z. Hazan, *Nature (London)* **460**, 1101 (2009).
- [10] T. H. Hsieh, H. Lin, J. Liu, W. Duan, A. Bansil, and L. Fu, *Nat. Commun.* **3**, 982 (2012).
- [11] L. Fu, *Phys. Rev. Lett.* **106**, 106802 (2011).
- [12] The term “topological crystalline insulator” has been introduced by L. Fu in Ref. [11]. In that publication general crystal symmetries are discussed and the theory is applied to rotational symmetries. A realization of a topological crystalline insulators is SnTe [10] which shows mirror symmetry and is characterized by an even mirror Chern number. In the course of this Letter, we use the term “topological crystalline insulator” for systems with nonzero mirror Chern number.
- [13] F. Zhang, C. L. Kane, and E. J. Mele, *Phys. Rev. Lett.* **110**, 046404 (2013).
- [14] See Supplemental Material at <http://link.aps.org/supplemental/10.1103/PhysRevLett.112.016802> for details of the computational approach.
- [15] W. Zhang, R. Yu, H.-J. Zhang, X. Dai, and Z. Fang, *New J. Phys.* **12**, 065013 (2010).
- [16] Y. Tanaka, Z. Ren, K. Nakayama, S. Souma, T. Takahashi, K. Segawa, and Y. Ando, *Nat. Phys.* **8**, 800 (2012).
- [17] Y. Okada, C. Dhital, W. Zhou, E. D. Huemiller, H. Lin, S. Basak, A. Bansil, Y.-B. Huang, H. Ding, Z. Wang, S. D. Wilson, and V. Madhavan, *Phys. Rev. Lett.* **106**, 206805 (2011).
- [18] J. Henk and W. Schattke, *Comput. Phys. Commun.* **77**, 69 (1993).
- [19] J. Henk, A. Ernst, S. V. Eremeev, E. V. Chulkov, I. V. Maznichenko, and I. Mertig, *Phys. Rev. Lett.* **108**, 206801 (2012).
- [20] L. Fu, *Phys. Rev. Lett.* **103**, 266801 (2009).
- [21] E. Simon, A. Szilva, B. Ujfalussy, B. Lazarovits, G. Zarand, and L. Szunyogh, *Phys. Rev. B* **81**, 235438 (2010).
- [22] A. Herdt, L. Plucinski, G. Bihlmayer, G. Mussler, S. Döring, J. Krumrain, D. Grützmacher, S. Blügel, and C. M. Schneider, *Phys. Rev. B* **87**, 035127 (2013).
- [23] *Very High Resolution Photoelectron Spectroscopy*, Lecture Notes in Physics, ed. by S. Hüfner (Springer, Berlin, 2007), Vol. 715.
- [24] D. Hsieh, Y. Xia, D. Qian, L. Wray, F. Meier, J. H. Dil, J. Osterwalder, L. Patthey, A. V. Fedorov, H. Lin, A. Bansil, D. Grauer, Y. S. Hor, R. J. Cava, and M. Z. Hasan, *Phys. Rev. Lett.* **103**, 146401 (2009).
- [25] G. Landwehr and E. I. Rashba, eds., *Landau Level Spectroscopy* (North Holland, Amsterdam, 1991).
- [26] T. Hanaguri, K. Igarashi, M. Kawamura, H. Takagi, and T. Sasagawa, *Phys. Rev. B* **82**, 081305(R) (2010).
- [27] S. Bordács, J. G. Checkelsky, H. Murakawa, H. Y. Hwang, and Y. Tokura, *Phys. Rev. Lett.* **111**, 166403 (2013).
- [28] X. Liu, H.-C. Hsu, and C.-X. Liu, *Phys. Rev. Lett.* **111**, 086802 (2013).
- [29] R. Yu, W. Zhang, H.-J. Zhang, S.-C. Zhang, X. Dai, and Z. Fang, *Science* **329**, 61 (2010).
- [30] C. Z. Chang, J. Zhang, X. Feng, J. Shen, Z. Zhang, M. Guo, K. Li, Y. Ou, P. Wei, L. L. Wang, Z. Q. Ji, Y. Feng, S. Ji, X. Chen, J. Jia, X. Dai, Z. Fang, S. C. Zhang, K. He, Y. Wang, L. Lu, X. C. Ma, and Q. K. Xue, *Science* **340**, 167 (2013).
- [31] C. Niu, Y. Dai, M. Guo, W. Wei, Y. Ma, and B. Huang, *Appl. Phys. Lett.* **98**, 252502 (2011).
- [32] J. Henk, M. Flieger, I. V. Maznichenko, I. Mertig, A. Ernst, S. V. Eremeev, and E. V. Chulkov, *Phys. Rev. Lett.* **109**, 076801 (2012).

Dual Topological Character of Chalcogenides: Theory for Bi₂Te₃

— Supplementary Information —

Tomáš Rauch,¹ Markus Flieger,¹ Jürgen Henk,¹ Ingrid Mertig,^{1,2} and Arthur Ernst²

¹*Department of Physics, Martin Luther University Halle-Wittenberg, Halle, Germany*

²*Max Planck Institute of Microstructure Physics, Halle, Germany*

TIGHT-BINDING CALCULATIONS

The empirical tight-binding method interpolates the band structure that has been determined by advanced first-principles methods. We adopted Slater-Koster parameters from Ref. [1], including spin-orbit coupling, and checked the band structure against our first-principles Korringa-Kohn-Rostoker and VASP calculations [2–4]. The agreement puts our tight-binding approach on a firm and reliable basis. The bulk bands are obtained by diagonalization of the Hamilton operator matrix in the basis of Bloch states $\Phi_\alpha(\vec{k})$, with α a compound index of orbital and atom; \vec{k} is the wavevector.

An external magnetic field \vec{B} is mimicked by adding a Zeeman term $\propto \vec{\sigma} \cdot \vec{B}$ to the otherwise ‘nonmagnetic’ Hamilton matrix. We varied both strength and direction of \vec{B} to change the topological phase of Bi₂Te₃.

The electronic structure of the (111) surface has been obtained for the semi-infinite system, using a renormalization scheme for the Green function [5, 6]. This scheme gives the layer-resolved block $G_{\alpha l, \beta m}(E, \vec{k}_\parallel)$ of the Green function matrix (l and m layer indices; \vec{k}_\parallel surface-parallel wavevector). The spectral density is then computed from

$$N_{\alpha l}(E, \vec{k}_\parallel) = -\frac{1}{\pi} \lim_{\eta \rightarrow 0^+} \text{Im tr } G_{\alpha l, \alpha l}(E + i\eta, \vec{k}_\parallel). \quad (1)$$

Appropriate partial traces allow to decompose the spectral density with respect to spin projection, orbital, etc. The limit $\eta \rightarrow 0^+$ is not taken but typically $\eta = 0.1$ meV. The dispersion of the Dirac state shows up as maxima in $N_{\alpha l}(E, \vec{k}_\parallel)$ of surface layers and agrees well with those obtained from our first-principles KKR (semi-infinite system) and VASP (slab of at least 6 quintuple layers) calculations. The tight-binding parameters of the quintuple layer were not changed with respect to those of the bulk. In the calculations of the surface state dispersion we used extremely fine E and \vec{k} meshes to reveal or exclude openings of tiny band gaps.

The spin texture of the Dirac state is investigated by means of spin-resolved spectral densities, with spin projections along the Cartesian axes and for an external magnetic field along x (within the surface but perpendicular to the mirror plane), y (within the surface and within the mirror plane) and z (normal to the surface and within the mirror plane). In Figure 1 we show spin

differences S_j ,

$$S_j(E, \vec{k}_\parallel) = -\frac{1}{\pi} \lim_{\eta \rightarrow 0^+} \text{Im tr } [\sigma_j G(E + i\eta, \vec{k}_\parallel)], j = x, y, z, \quad (2)$$

where G is the surface block of the Green function matrix. We focus on the region close to the Dirac point of pure Bi₂Te₃ where warping is of minor importance and the spin texture is essentially determined by the Rashba Hamilton operator $H_0 + H_1^{\text{soc}}$, defined in the Section on model calculations.

Without magnetic field we find the standard Rashba spin texture, with clockwise rotation of the spin. The degree of spin polarization in the upper Dirac cone is 68 % in the vicinity of the Dirac point (at $k_x = 0.024 \text{ \AA}^{-1}$).

CALCULATION OF THE \mathcal{Z}_2 INVARIANT AND THE MIRROR CHERN NUMBER

The tight-binding method allows a fast and reliable computation of topological invariants [7]. The \mathcal{Z}_2 invariant is calculated from the Fu-Kane formula [8] discretized according to Fukui and Hatsugai [9]. For sufficiently dense \vec{k} meshes we compute the \mathcal{Z}_2 invariants $(\nu_0; \nu_1 \nu_2 \nu_3) = (1; 000)$ for Bi₂Te₃ without magnetic field. Note that a \mathcal{Z}_2 invariant can only be defined if time-reversal symmetry is not broken.

In the calculation of the mirror Chern number, we follow the idea of the spin Chern number [10]. The Bloch states with wavevector \vec{k} within the considered mirror plane are eigenstates of both the Hamiltonian and the mirror operator [11]. This allows us to divide the Bloch states into two categories: one with mirror eigenvalue $+i$, the other with eigenvalue $-i$. The \vec{k} -dependent Berry curvature is calculated for both of them. The weighted sum of the Berry curvature over a discrete \vec{k} set in the intersection of the mirror plane with the Brillouin zone gives the Chern number $n_{\pm i}$ for each category. The mirror Chern number is then defined as [12]

$$c_m \equiv \frac{n_{+i} - n_{-i}}{2}. \quad (3)$$

We calculate the mirror Chern number for a mesh of 100×100 k -points, getting $c_m = -1$ for Bi₂Te₃ both without and with magnetic field perpendicular to the mirror plane (relative error less than 10^{-4}). From this we conclude that the surface state is protected by the mirror

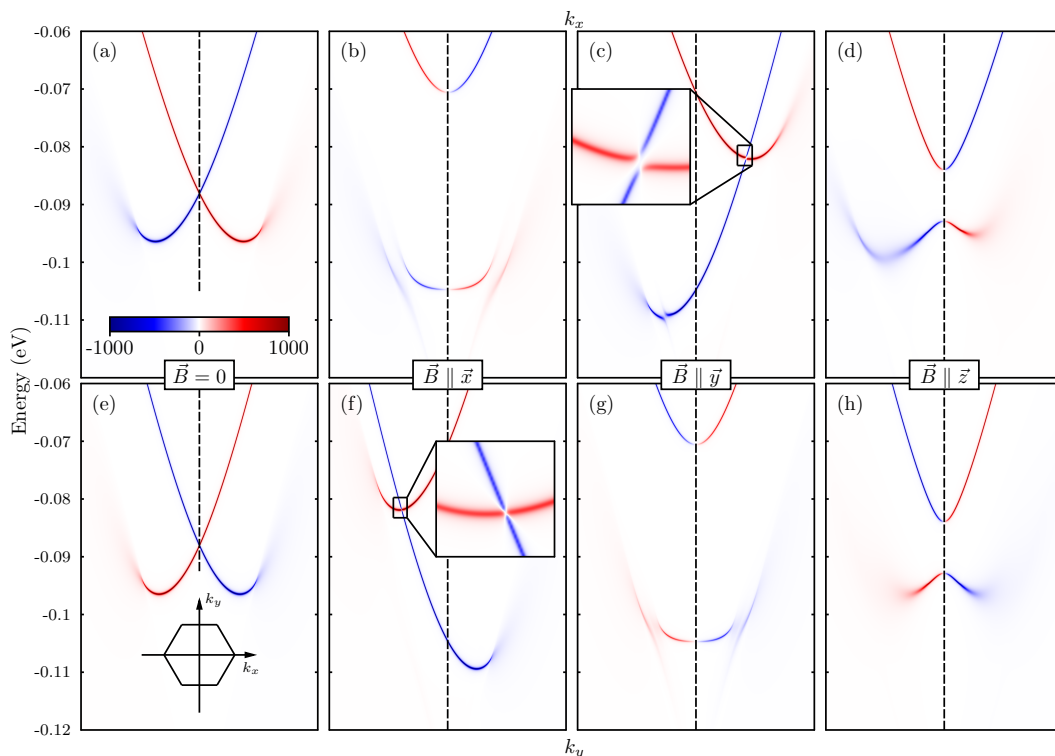


FIG. 1. (Color) As Figure 3 of the paper but for the spin-resolved dispersion of the Dirac state at the (111) surface of Bi_2Te_3 . The color scale (in units of states/eV) displays the ‘Rashba’ component of the spin textures, that is the y component S_y for k_x (upper row) and the x component S_x for k_y (lower row) of the spin differences, eq. (2). The rectangles display zooms into the (E, k) region at the Dirac point.

symmetry even with finite magnetic field. Note that a mirror Chern number can be defined only if the mirror symmetry is not broken.

MODEL CALCULATIONS

The model Hamiltonian H , derived within $\vec{k} \cdot \vec{p}$ theory, consists of four terms,

$$H = H_0 + H_1^{\text{SOC}} + H_3^{\text{SOC}} + H^{\text{mag}}. \quad (4)$$

H_0 mimics the dispersion of the electron gas without spin-orbit coupling (SOC). H_1^{SOC} is the spin-orbit interaction in first order in the wavevector $\vec{k}_{\parallel} = (k_x, k_y)$,

$$H_1^{\text{SOC}} = \alpha_1(k_x\sigma_y - k_y\sigma_x) \quad (5)$$

($\sigma_x, \sigma_y, \sigma_z$ Pauli matrices). α_1 is the Rashba parameter.

The third-order term of the SOC reads

$$H_3^{\text{SOC}} = \alpha_2[(k_x^2 + k_y^2)k_x\sigma_y - (k_y^2 - k_x^2)k_y\sigma_x] + \alpha_3(k_x^2 - 3k_y^2)k_x\sigma_z \quad (6)$$

The terms with σ_x and σ_y are isotropic. If merged with H_1^{SOC} , they yield a quadratic k -dependence of the effective

Rashba parameter [13, 14]. The term with σ_z introduces the warping of the Dirac cone and tilts the electron spin out of the xy plane [3, 15].

The coupling of the electron spin to an external magnetic field \vec{B} or to magnetic impurities is accounted for by a Zeeman term,

$$H^{\text{mag}} \propto \vec{\sigma} \cdot \vec{B}. \quad (7)$$

The parameters α_1 etc. for Bi_2Te_3 were taken from Ref. [13], with the purpose to reproduce reasonably the dispersion of the Dirac state and providing general insights rather than perfectly reproducing experimental data.

REFERENCES

-
- [1] P. Pecheur and G. Toussaint, *J. Phys. Chem. Sol.* **55**, 327 (1994).
 - [2] S. V. Eremeev, G. Landolt, T. V. Menshchikova, B. Slomski, Y. M. Koroteev, Z. S. Aliev, D. M. Babanly, J. Henk, A. Ernst, L. Patthey, A. Eich, A. A. Khajetoorians,

- J. Hagemester, O. Pietsch, J. Wiebe, R. Wiesendanger, P. M. Echenique, S. S. Tsirkin, I. R. Amiraslanov, J. H. Dil, and E. V. Chulkov, *Nature Comms.* **3**, 635 (2012).
- [3] J. Henk, A. Ernst, S. V. Eremeev, E. C. Chulkov, I. V. Maznichenko, and I. Mertig, *Phys. Rev. Lett.* **109**, 036803 (2012).
- [4] J. Henk, M. Flieger, I. V. Maznichenko, I. Mertig, A. Ernst, S. V. Eremeev, and E. V. Chulkov, *Phys. Rev. Lett.* **109**, 076801 (2012).
- [5] J. Henk and W. Schattke, *Comp. Phys. Commun.* **77**, 69 (1993).
- [6] A. Bödicker, W. Schattke, J. Henk, and R. Feder, *J. Phys.: Condens. Matt.* **6**, 1927 (1994).
- [7] J. E. Moore and L. Balents, *Phys. Rev. B* **75**, 121306 (2007).
- [8] L. Fu and C. L. Kane, *Phys. Rev. B* **74**, 195312 (2006).
- [9] T. Fukui and Y. Hatsugai, *J. Phys. Soc. Jpn.* **76**, 053702 (2007).
- [10] E. Prodan, *Phys. Rev. B* **80**, 125327 (2009).
- [11] T. Inui, Y. Tanabe, and Y. Onodera, *Group Theory and Its Applications in Physics*, Springer Series in Solid State Sciences, Vol. 78 (Springer, Berlin, 1990).
- [12] J. C. Y. Teo, L. Fu, and C. L. Kane, *Phys. Rev. B* **78**, 045426 (2008).
- [13] L. Fu, *Phys. Rev. Lett.* **103**, 266801 (2009).
- [14] E. Simon, A. Szilva, B. Ujfalussy, B. Lazarovits, G. Zarand, and L. Szunyogh, *Phys. Rev. B* **81**, 235438 (2010).
- [15] S. Souma, K. Kosaka, T. Sato, M. Komatsu, A. Takayama, T. Takahashi, M. Kriener, K. Segawa, and Y. Ando, *Phys. Rev. Lett.* **106**, 216803 (2011).

6.4 NONTRIVIAL INTERFACE STATES CONFINED BETWEEN TWO TOPOLOGICAL INSULATORS

After having investigated some common properties of \mathcal{Z}_2 TIs and TCIs, in the next project [TR4] we concentrated on their common interfaces. Already in 2011 Takahashi and Murakami [124] have shown that at a common interface of two TIs the interface states can still cross the band gap without splitting when they possess opposite spin chiralities, i.e. the rotation directions of spin polarization along the Fermi line of the Dirac cones. When the spin chiralities are identical, then the surface states split and their topological character is lost. This behaviour was explained by the mirror Chern number whose sign is connected to the spin chirality. Assuming a common mirror plane for both systems, the difference of the mirror Chern numbers gives the number of interface states connecting the valence and conduction bands without any splitting.

Following the ideas of Takahashi and Murakami we modelled an interface of a \mathcal{Z}_2 TI Bi_2Te_3 with the TCI SnTe . Both compounds were brought together with their (111) surfaces. The topological invariants were calculated for both materials, confirming previous findings. For Bi_2Te_3 $(\nu_0; \nu_1\nu_2\nu_3) = (1; 000)$, $n_M = -1$ and for SnTe $(\nu_0; \nu_1\nu_2\nu_3) = (0; 000)$, $n_M = -2$, indicating that there are two surface states at the free (111) surface of SnTe , having the same spin chirality as the one surface state of Bi_2Te_3 . By the sum rule for mirror Chern numbers of Takahashi and Murakami there should be one interface state crossing the band gap at the $\text{Bi}_2\text{Te}_3/\text{SnTe}$ interface.

These considerations based on the calculations of bulk topological invariants were confirmed by the calculation of the interface electronic structure. The strength of the coupling between the two systems was continuously increased from zero to the full coupling, in order to visualize the process of annihilation of the surface states located at $\bar{\Gamma}$, showing that for small coupling strength there is an avoided-crossing-like signature, whereas for a fully coupled systems the surface states are completely shifted out of the band gap. There is one interface state left, localized at the \bar{M} point of the interface BZ.

In addition, the same calculation was performed for a $\text{Bi}_2\text{Te}_3/\text{Sb}_2\text{Te}_3$ interface, showing that both surface states annihilate leaving no interface state left because the subsystems possess the same mirror Chern number. This confirms the results of reference [124].

Nontrivial interface states confined between two topological insulators

Tomáš Rauch,¹ Markus Flieger,¹ Jürgen Henk,¹ and Ingrid Mertig^{1,2}¹*Institut für Physik, Martin-Luther-Universität Halle-Wittenberg, D-06099 Halle (Saale), Germany*²*Max-Planck-Institut für Mikrostrukturphysik, D-06120 Halle (Saale), Germany*

(Received 19 July 2013; revised manuscript received 25 October 2013; published 17 December 2013)

By *ab initio* based tight-binding calculations, we show that nontrivial electronic states exist at an interface of a \mathcal{Z}_2 topological insulator and a topological crystalline insulator. At the exemplary (111) interface between Bi_2Te_3 and SnTe , the two Dirac surface states at the Brillouin zone center $\bar{\Gamma}$ annihilate upon approaching the semi-infinite subsystems but one topologically protected Dirac surface state remains at each time-reversal invariant momentum \bar{M} . This leads to a highly conducting spin-momentum-locked channel at the interface but insulating bulk regions. For the $\text{Sb}_2\text{Te}_3/\text{Bi}_2\text{Te}_3$ interface, we find complete annihilation of Dirac states because both subsystems belong to the same topology class. Our proof of principle may have impact on planar electric transport in future spintronics devices with topologically protected conducting channels.

DOI: [10.1103/PhysRevB.88.245120](https://doi.org/10.1103/PhysRevB.88.245120)

PACS number(s): 73.20.At, 71.70.Ej

I. INTRODUCTION

Three-dimensional topological insulators are a new class of materials that are characterized by an insulating bulk but highly conducting surface states.¹ These surface states bridge the fundamental band gap and are topologically protected against perturbations. Two classes of three-dimensional topological insulators (TIs) are currently investigated with great effort: \mathcal{Z}_2 TIs rely on time-reversal symmetry and an odd number of band inversions in the bulk Brillouin zone; topological crystalline insulators (TCIs)² require a crystal symmetry, in particular, mirror symmetry, but may possess an even number of band inversions. Brought about by the spin-orbit interaction, the fundamental band gaps of TIs are small compared to those of typical band insulators (100–250 meV).

Prominent examples for \mathcal{Z}_2 TIs are the chalcogenides Bi_2Se_3 , Bi_2Te_3 , and Sb_2Te_3 , each showing a band inversion at the center Γ of the bulk Brillouin zone. They are characterized by \mathcal{Z}_2 topological invariants $(\nu_0; \nu_1 \nu_2 \nu_3) = (1; 000)$ (see Ref. 3) and have a single Dirac surface state at the center $\bar{\Gamma}$ of their (111) surface's Brillouin zone. The spin chirality of these surface states is dictated by those p orbitals that make up the inverted band gap; thus, it is identical among the chalcogenides.^{4–6} As a consequence, the two Dirac surface states at a common interface of two chalcogenide TIs annihilate because the two subsystems are in the same topological phase. They would not annihilate if their spin chirality would be opposite;⁷ however, such a \mathcal{Z}_2 TI is yet unknown.

One representative of a TCI with mirror symmetry is SnTe ,^{8,9} showing band inversions at the L points of the bulk Brillouin zone. For a mirror plane that is spanned by four L points, the relevant topological invariant—the mirror Chern number—equals -2 . Thus there are two Dirac points associated with that plane. For the (001) surface, these are close to the time-reversal invariant momentum (TRIM) \bar{X} . This crystal orientation does not fit to the commonly investigated (111) orientation of the chalcogenides which is naturally induced by their quintuple-layer geometry. Therefore, to form a common interface of SnTe and Bi_2Te_3 , one should choose the (111) surface of SnTe that also shows two Dirac surface states, one at $\bar{\Gamma}$ (as, e. g., Bi_2Te_3), another at \bar{M} ; these states have

identical spin chirality. Because the chalcogenides are also topological crystalline insulators, with a mirror Chern number of -1 (see Ref. 10), the spin chiralities of the surface states of SnTe and Bi_2Te_3 are identical as well. As a consequence, surface states annihilate at a common interface of SnTe and Bi_2Te_3 .

From these considerations, the question arises whether all Dirac surface states of Bi_2Te_3 (111) and SnTe (111) annihilate at a common interface. Or do only two of them obliterate each other and does one nontrivial surface state remain (see Fig. 1)? In this Paper, we provide a proof of principle by means of *ab initio* based tight-binding calculations that the pair of Dirac surface states at $\bar{\Gamma}$ indeed annihilates but the Dirac surface state at \bar{M} “survives.” This remaining electronic state is topologically protected by mirror symmetry and results in a highly conducting channel at the interface of two bulk topological insulators. This conductance channel with spin-momentum locking could be utilized in future electronics. For comparison, the $\text{Sb}_2\text{Te}_3/\text{Bi}_2\text{Te}_3$ interface shows complete annihilation of Dirac states because both subsystems belong to the same topology class, resulting in an entirely insulating system.

The paper is organized as follows. Theoretical aspects are addressed in Sec. II, in which we provide details of the electronic structure calculations (Sec. II A) and topological-invariant calculations (Sec. II B). Results are discussed in Sec. III. For the topological heterophase system $\text{SnTe}/\text{Bi}_2\text{Te}_3$, we address the annihilation and survival of the Dirac states (Sec. III A 1), a model Hamiltonian (Sec. III A 2), and the localization of the Dirac states (Sec. III A 3). The complete annihilation of Dirac states in the topological iso-phase system $\text{Sb}_2\text{Te}_3/\text{Bi}_2\text{Te}_3$ is presented in Sec. III B. A sum rule for the number of Dirac states at an interface is given in Sec. III C, before concluding with Sec. IV.

II. THEORETICAL ASPECTS

A. Tight-binding calculations

The purpose of our approach is to support our main statement of annihilation of a pair of Dirac states and the survival of one Dirac state. To do so, the method accounts for

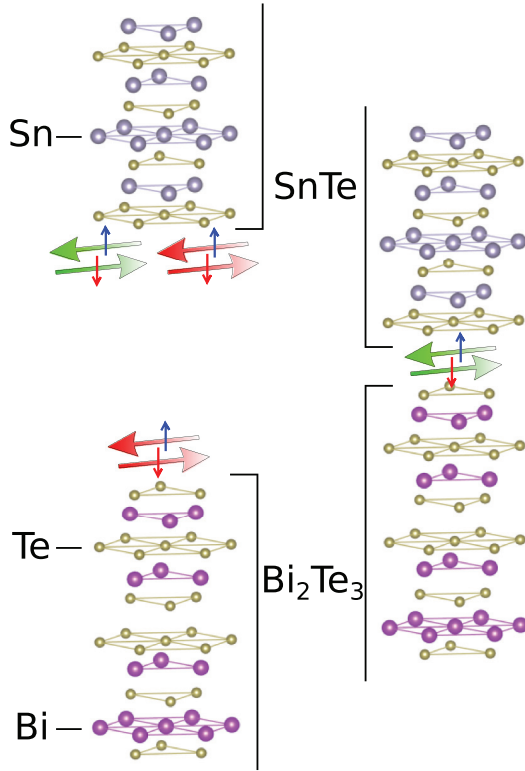


FIG. 1. (Color online) Topologically nontrivial electronic states at the (111) surfaces of the \mathcal{Z}_2 topological insulator Bi_2Te_3 and the topological crystalline insulator SnTe (left) as well as their common interface (right). $\text{Bi}_2\text{Te}_3(111)$ hosts one state (red arrows), while $\text{SnTe}(111)$ hosts two states (red and green arrows). Upon formation of an interface, the “red” surface states annihilate but the “green” SnTe -derived state survives. Spin and momentum are locked: states propagating to the left are spin up (small blue arrows), states propagating to the right are spin down (small red arrows). Te, Bi, and Sn atoms are displayed in brown, magenta, and grey, respectively.

the correct boundary conditions of an interface⁴⁸ and relies on a tight-binding parametrization, which works also well for other chalcogenides and rocksalt insulators.¹¹

The empirical tight-binding method interpolates the band structure that has been determined by advanced first-principles methods. We adopted Slater-Koster parameters, from Ref. 12 for Bi_2Te_3 as well as from Ref. 13 for SnTe . The parameters for Sb_2Te_3 have been fitted to an *ab initio* band structure using a Monte Carlo method.^{14,15} Spin-orbit coupling is treated as in Ref. 16. All parameter sets yield good agreement, in particular for the important energy range near the fundamental band gap.¹⁷

The resulting band structures were checked against our first-principles Korringa-Kohn-Rostoker, VASP, and WIEN2K calculations.^{11,18–20} The agreement puts our tight-binding approach on a firm and reliable basis. The bulk bands are obtained by diagonalization of the Hamilton operator matrix in the basis of Bloch states $\Phi_\alpha(\vec{k})$, with α a compound index of orbital, spin orientation, and atom; \vec{k} is the wave vector.

The electronic structures of the (111) surfaces and interfaces have been obtained for the semi-infinite systems, using a renormalization scheme for the Green function, originally

developed for surfaces^{21,22} and later extended to interfaces.²³ A description of this scheme is rather lengthy; therefore we provide a sketch here. The system is decomposed into principal layers in such a way that only adjacent principal layers interact, making the Hamiltonian matrix \mathbf{H} block-tridiagonal. These interactions are reduced by a renormalization process using the defining matrix equation

$$\mathbf{G}(z, \vec{k}_\parallel)[z\mathbf{1} - \mathbf{H}(\vec{k}_\parallel)] = \mathbf{1}, \quad (1)$$

in which $z = E + i\eta$, $\eta > 0$, is a complex energy argument. For vanishing interlayer interaction, this scheme yields layer-resolved blocks $\mathbf{G}_{lm}(z, \vec{k}_\parallel)$ of the Green function matrix which is indexed by compound indices α and β (l and m principal layer indices; \vec{k}_\parallel surface-parallel wave vector). Surface and interface states appear “naturally” in this procedure, e. g., without additional treatment.²⁴

The layer-resolved spectral density is then computed from

$$N_l(E, \vec{k}_\parallel) = -\frac{1}{\pi} \lim_{\eta \rightarrow 0^+} \text{Im} \text{tr}_\alpha \mathbf{G}_{ll}(E + i\eta, \vec{k}_\parallel). \quad (2)$$

Appropriate partial traces allow to decompose the spectral density with respect to, e. g., spin projection and orbital.

The spin texture of the Dirac states is investigated by means of spin-resolved spectral densities, with spin projections typically along the Cartesian axes. Instead of the spin polarization, we use spin differences:

$$\vec{S}_l(E, \vec{k}_\parallel) = -\frac{1}{\pi} \lim_{\eta \rightarrow 0^+} \text{Im} \text{tr}_\alpha [\vec{\sigma} \mathbf{G}_{ll}(E + i\eta, \vec{k}_\parallel)], \quad (3)$$

where $\vec{\sigma}$ is the vector of Pauli matrices. The limit $\eta \rightarrow 0^+$ in Eqs. (2) and (3) is not taken but typically $\eta = 2$ meV.

The dispersions of the Dirac states show up as maxima in $N_{\alpha l}(E, \vec{k}_\parallel)$ of the interface layers; they agree well with those obtained from our first-principles Korringa-Kohn-Rostoker (semi-infinite system) and VASP (slab of at least six quintuple layers) calculations for Bi_2Te_3 and Sb_2Te_3 . For SnTe , we checked also the electronic structure of the (001) surface and found agreement with that reported in Ref. 8.

The lattice constants of Bi_2Te_3 and SnTe show a mismatch of about 2%. We assume that $\text{SnTe}(111)$ adopts the in-plane lattice constant of Bi_2Te_3 ; the out-of-plane (interlayer) distance is chosen to conserve the volume of the bulk unit cell. The tight-binding parameters of SnTe have, thus, been scaled using Harrison’s d^{-2} law.²⁵ SnTe remains a topological crystalline insulator in this distorted phase but with a reduced width of the fundamental band gap (250 meV \rightarrow 40 meV). Although the Slater-Koster parameters at the surface or interface are taken from bulk values, the surface electronic structures agree with those reported earlier.^{8,19} The valence band maxima of the bulk systems have been aligned to the common Fermi level in the interface system, in accordance with the “common anion rule” (see Ref. 26).

Concerning the $\text{SnTe}/\text{Bi}_2\text{Te}_3$ interface, the outermost SnTe layer is made of Te atoms.⁴⁹ The distance between these atoms and the outermost Te atoms of Bi_2Te_3 is assumed identical to that between the outermost Te atoms of adjacent quintuple layers of Bi_2Te_3 (i. e., the van der Waals gap). Therefore the Slater-Koster parameters at the interface are identical to

those describing the coupling between two quintuple layers of Bi_2Te_3 .

To perform the transition from two separate surfaces to a joint interface, we scale the tight-binding parameters that mediate the hopping between the two half-spaces by a factor κ , with $\kappa = 0$ ($\kappa = 1$) for zero (full) coupling; confer the bond-cutting mechanism in Ref. 27. This procedure can be viewed as letting the surfaces approach in real space (schematically shown Fig. 1): $\kappa = 0$ mimics an infinite distance. NB: we could have used Harrison's d^{-2} scaling (see Ref. 25), with identical results for the most important cases: vanishing and full coupling.

The tight-binding parameters of the surface or interface layers were not changed with respect to those of the bulk. The (111) surfaces of both the chalcogenides and SnTe show band bending due to their polar nature. For Bi_2Se_3 (111), the band bending region extends about 200 Å (see Ref. 28), and we expect a similar width for Bi_2Te_3 . Because the Dirac surface state is strongly located in the first quintuple layer (see below) it is mildly affected by the band bending. In the *ab initio* calculations reported in Ref. 19, in which the potentials of the first five quintuple layers are allowed to differ from those in the bulk, no clear indication for band bending was found. Although these two findings seem to contradict each other, they both support to neglect the band bending in the description of the Dirac surface state of Bi_2Te_3 for the time being.

Concerning SnTe, an appropriate *ab initio* description requires advanced exchange-correlation functionals, e. g., hybrid functionals¹¹ [the self-consistent calculation for SnTe(001) reported in Ref. 8 relies on the generalized gradient approximation]. This makes such advanced density-functional calculations computationally very demanding for the bulk system but nearly impossible for a surface system. Our tight-binding approach is numerically much less demanding and, importantly, it reproduces very well the bulk electronic structure of Ref. 11 and the Dirac surface states of SnTe(001) reported in Refs. 8 and 9.

Hybrid functionals give a better description of the fundamental band gap than the often used local density approximation for the exchange-correlation functional. This is in particular important for small-gap semiconductors (here, SnTe). A too small band gap would result in a distorted dispersion relation of the topologically protected surface states.

Being computationally demanding, a hybrid-functional calculation mimicking a surface system might be performed for a slab with small thickness. Therefore surface states located at either side of the slab would hybridize and show artificial band gaps due to quantum confinement. These gaps could be significantly wide for weakly localized surface states, as would be the case for the surface state in SnTe(111) at \bar{M} , as we will see below. In our study on $\text{Bi}_2\text{Te}_3/\text{SnTe}$ interfaces, the opening up of band gaps is a crucial point; artificial band gaps would make the interpretation difficult and, thus, should be avoided. In our approach, this problem is overcome by the renormalization technique for semi-infinite systems.

For the band alignment, we follow the common anion rule (see Refs. 29–31), discussed in the supplement of Ref. 26. This

rule applies to interfaces of insulators with a common anion. In this case, the valence electronic states are primarily derived from the anion orbitals (Te) whereas the conduction bands are primarily derived from the cation orbitals. Consequently, the valence states should be similar, leading to a smaller offset of the valence bands than of the conduction bands. Taskin *et al.* argue that the band bending shows up mainly in Bi_2Te_3 rather than in SnTe (see Ref. 26).

B. Calculation of \mathcal{Z}_2 invariants and mirror Chern numbers

The tight-binding method allows a fast and reliable computation of topological invariants.³ The \mathcal{Z}_2 invariant is calculated from the Fu-Kane formula³² discretized according to Fukui and Hatsugai.³³ For sufficiently dense \vec{k} meshes we compute the \mathcal{Z}_2 invariants $(\nu_0; \nu_1 \nu_2 \nu_3) = (1; 000)$ for Bi_2Te_3 and Sb_2Te_3 as well as $(0; 000)$ for SnTe.

In the calculation of the mirror Chern number, we follow the idea of the spin Chern number.³⁴ The considered mirror plane is normal to a (111) surface plane; in reciprocal space, it comprises the $\bar{\Gamma}$ and \bar{M} points of the surface Brillouin zone (confer Fig. 1 in both Ref. 8 and 10). The Bloch states with wave vector \vec{k} within this mirror plane are eigenstates of both the Hamiltonian and the mirror operator.³⁵ This allows us to divide the Bloch states into two categories: one with mirror eigenvalue $+i$, the other with eigenvalue $-i$. The \vec{k} -dependent Berry curvature is calculated for both of them. The weighted sum of the Berry curvature over a discrete \vec{k} set in the intersection of the mirror plane with the Brillouin zone gives the Chern number $n_{\pm i}$ for each category. The mirror Chern number is then obtained from⁴

$$c_m \equiv \frac{n_{+i} - n_{-i}}{2}. \quad (4)$$

We calculate the mirror Chern number for a mesh of 100×100 k points, getting $c_m = -1$ for Bi_2Te_3 and Sb_2Te_3 as well as -2 for SnTe, with a relative error less than 10^{-4} .

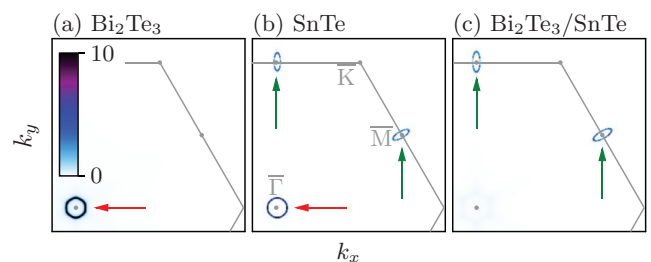


FIG. 2. (Color online) Electronic structure of (a) the Bi_2Te_3 (111) surface, (b) the SnTe(111) surface, and (c) a $\text{Bi}_2\text{Te}_3/\text{SnTe}$ (111) interface. The spectral densities of the outermost surface layers [(a) and (b)] or the SnTe interface layer (c) are shown as color scale (in states/eV) for a constant energy of 0.08 eV (i. e., within the fundamental band gap). In each panel, the same part of the hexagonal Brillouin zone is displayed; high-symmetry points and the Brillouin zone edge are indicated by grey dots and lines, respectively. Arrows mark surface and interface states.

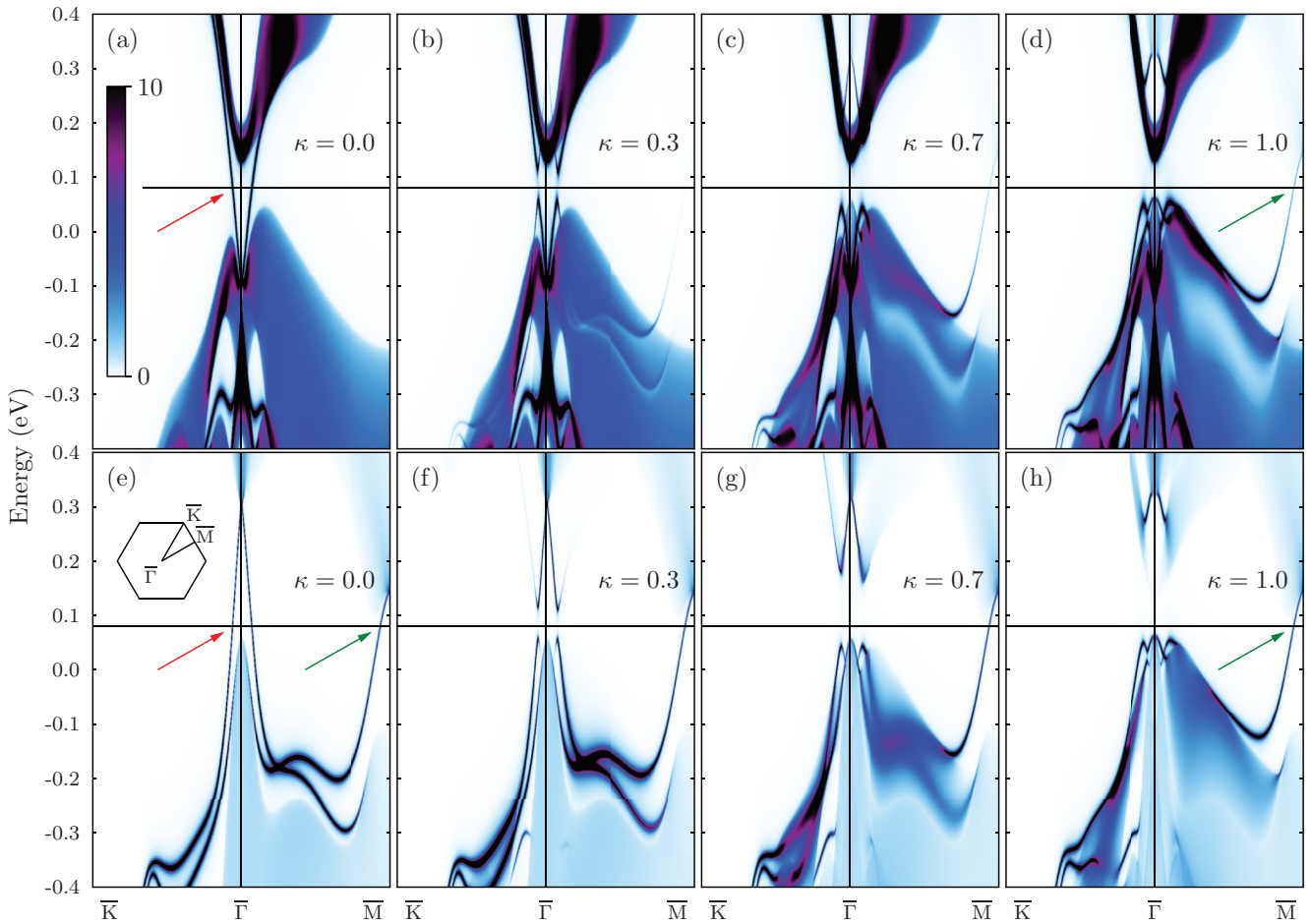


FIG. 3. (Color online) Electronic structure of a $\text{Bi}_2\text{Te}_3/\text{SnTe}(111)$ interface, obtained from tight-binding calculations. The spectral densities of the outermost Bi_2Te_3 [top, (a)–(d)] and SnTe [bottom, (e)–(h)] interface layers are shown as color scale (in units of states/eV) for a $\bar{K}-\bar{\Gamma}-\bar{M}$ path in the two-dimensional Brillouin zone [inset in (e)]. The coupling strength κ of the semi-infinite systems increases from left to right ($\kappa = 0$ uncoupled; $\kappa = 1$ fully coupled). The horizontal lines mark the energy of 0.08 eV used in Fig. 2. Arrows in (a), (d), (e), and (h) point towards Dirac surface or interface states (also indicated in Fig. 2).

III. DISCUSSION AND RESULTS

A. Interface electronic structure of $\text{SnTe}(111)/\text{Bi}_2\text{Te}_3(111)$

1. Annihilation and survival of Dirac states

The surface band structure of $\text{Bi}_2\text{Te}_3(111)$ shows the well-known Dirac surface state, with its Dirac point close to the valence bands at $\bar{\Gamma}$. In a constant energy cut (CEC), this state results in a slightly warped³⁶ circular shape [red arrow in Fig. 2(a)]. The (111) surface of SnTe hosts two Dirac states: the state at $\bar{\Gamma}$ produces a circular shape in a CEC [red arrow in Fig. 2(b)], the equivalent states at \bar{M} show up as ellipses [green arrows in Fig. 2(b)].

Upon approaching the two semi-infinite systems, that is by increasing κ to 1, the two circular contours at $\bar{\Gamma}$ disappear but the structures at \bar{M} remain [green arrows in Fig. 2(c)]. This “annihilation” of the pair of states at $\bar{\Gamma}$ can be interpreted by opening of a band gap in the two respective surface states.

This scenario is illustrated by the interface electronic structure for selected coupling strengths κ (see Fig. 3). For $\kappa = 0$, we find the surface band structures of Bi_2Te_3 and SnTe , both

showing a Dirac surface state at $\bar{\Gamma}$ bridging the fundamental band gap (red arrows in a and e). The Dirac points are close

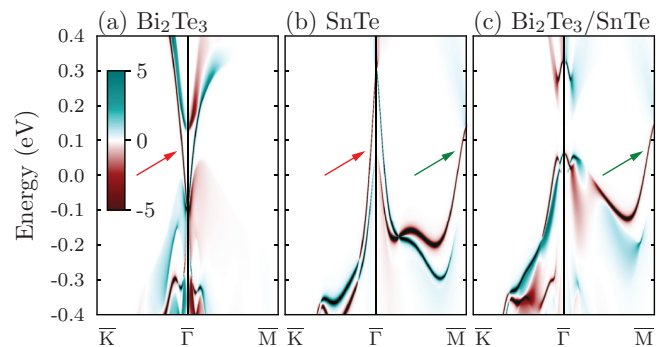


FIG. 4. (Color online) Spin-resolved electronic structure of (a) $\text{Bi}_2\text{Te}_3(111)$, (b) $\text{SnTe}(111)$, and (c) $\text{Bi}_2\text{Te}_3/\text{SnTe}(111)$. The spectral spin differences of the outermost surface layer [(a) and (b); $\kappa = 0$] and the SnTe interface layer [(c), $\kappa = 1$], presented as color scale (in units of states/eV), are resolved with respect to the Rashba component of the spin polarization. Arrows mark Dirac surface or interface states, as in Fig. 3.

to the valence bands, in Bi_2Te_3 , or to the conduction bands, in SnTe . With increasing κ , the Bi_2Te_3 layer “picks up” spectral weight from SnTe , seen by the pale colors, and vice versa.

A first important observation is that a band gap opens up in the $\bar{\Gamma}$ surface states because these states have identical spin chirality; compare Figs. 3(a) and 3(b) as well as Figs. 3(e) and 3(f). The width of this band gap increases with κ [Figs. 3(c) and 3(g)], so that for full coupling these surface states merge with the bulk-state continuum and are entirely shifted out of the fundamental band gap [Figs. 3(d) and 3(h)]. The band gap opening is accompanied by the formation of Rashba-type dispersions, clearly seen in Fig. 3(f). Such a dispersion has been observed for surface states in $\text{Au}(111)$ and $\text{Bi}/\text{Ag}(111)$.^{37,38} The hybridization of the two Dirac states turns their linear dispersion of massless relativistic Fermions into the spin-orbit-split dispersion of massive electrons.

Another striking feature is that the SnTe surface state at \bar{M} [green arrow in Fig. 3(e)] “survives” the formation of the interface [green arrows in Figs. 3(d) and 3(h)]. More precisely, its dispersion does not change significantly with κ [Figs. 3(e)–3(h)], which is readily explained by the considerable local band gap around \bar{M} . It is this Dirac interface state that forms a topologically protected conducting channel in an otherwise insulating system. In contrast, the two Dirac surface states at $\bar{\Gamma}$ in $\text{Bi}_2\text{Te}_3/\text{Sb}_2\text{Te}_3$ annihilate upon increasing the coupling κ because both subsystems are in the same topological phase (see Sec. III B).

In view of applications, the spin textures of the surface and interface states are essential quantities; in particular, spin-momentum locking could be used in spintronics devices.³⁹ The spin polarization of the $\text{Bi}_2\text{Te}_3(111)$ Dirac state is of Rashba type: the spin is mostly in-plane and perpendicular to \bar{k}_\parallel [see Fig. 4(a)]; the degree of spin polarization equals 53 %, in agreement with first-principles calculations.^{19,40} Along $\bar{K}-\bar{\Gamma}$, it is tilted out-of-plane due to warping (not shown here).^{19,36}

The $\bar{\Gamma}$ surface state of $\text{SnTe}(111)$ shows the same spin chirality as its counterpart in Bi_2Te_3 [see Fig. 4(b)], which is indicated by the identical sign of their mirror Chern number.⁵⁰ At the energy of the constant energy cuts of Fig. 2, the spin helicity of all Dirac states is clockwise. Note within this respect that Figs. 4(a) and 4(b) show facing surfaces. The surface states are almost completely spin polarized (93 % close to $\bar{\Gamma}$, 98 % close to \bar{M}); the state at \bar{M} displays an out-of-plane component of 15 % on the $\bar{M}-\bar{K}$ line.

The spin-momentum locking of the surviving interface state at \bar{M} is proven in Fig. 4(c). In the SnTe interface layer, the Rashba spin polarization is 98 % along $\bar{\Gamma}-\bar{M}$; along $\bar{M}-\bar{K}$ it equals 90 %, with an out-of-plane contribution of 21 %. In the adjacent Bi_2Te_3 quintuple layer, these numbers are slightly less (77 %, 81 %, and 10 %, respectively). This large degree of spin polarization lends itself support for spintronics applications.

2. Model Hamiltonian

The Dirac states at \bar{M} are well described by the Hamiltonian (in atomic units; $\hbar = m_e = 1$)

$$\hat{H} = \frac{k_x^2}{2m_x^*} + \frac{k_y^2}{2m_y^*} + \alpha_{xy}k_x\sigma_y + \alpha_{yx}k_y\sigma_x + \alpha_{xz}k_x\sigma_z, \quad (5)$$

which has been derived from $\vec{k} \cdot \vec{p}$ theory for the point group C_s (see Refs. 35 and 41). \vec{k}_\parallel is centered at \bar{M} , the σ 's are Pauli matrices. A fit to the tight-binding bands yields effective masses of $m_x^* = -0.01$ and $m_y^* = -0.03$, which indicate almost linear dispersion. The spin-orbit parameters read $\alpha_{xy} = 0.89 \text{ eV \AA}$, $\alpha_{yx} = 3.31 \text{ eV \AA}$, and $\alpha_{xz} = 0.77 \text{ eV \AA}$. The in-plane α 's are strongly anisotropic, as expected from the elongated CECs. α_{yx} is even larger than the “giant” Rashba parameter of $\text{Bi}/\text{Ag}(111)$ (3.05 eV \AA , Ref. 38).

3. Surface and interface localization of Dirac states

We investigated the localization of the Dirac states for the uncoupled ($\kappa = 0$) and the fully coupled ($\kappa = 1$) systems. For the surface system $\text{SnTe}(111)$, the Dirac surface state with a Dirac point at $\bar{\Gamma}$ is strongly localized at the surface (top row in Fig. 5); this is deduced from the color saturation decreasing from (a) to (c) and almost zero spectral weight in (d) and (e). The other Dirac state, with a Dirac point at \bar{M} , is comparably weakly localized at the surface, as seen by the nonzero but small spectral weight in (d) and (e).

The Dirac surface state in $\text{Bi}_2\text{Te}_3(111)$ is strongly localized within the topmost quintuple layer (bottom row in Fig. 5), in agreement with earlier calculations. This state shows significant spectral weight (large color saturation) only in the first quintuple layer (f) but almost zero spectral weight in the deeper layers [(g)–(j)]. The layers chosen for panels [(a)–(e)], for $\text{SnTe}(111)$, have almost the same distance from the surface atomic layer as the central atomic layers of the quintuple layers of Bi_2Te_3 ; this facilitates comparing the decay of the surface states in both compounds.

For the interface system $\text{SnTe}(111)/\text{Bi}_2\text{Te}_3(111)$ (see Fig. 6, $\kappa = 1$), the Dirac state with Dirac point at \bar{M} , which is derived from the surface state in $\text{SnTe}(111)$, survives, while the other two surface states annihilate. Its weak localization at the $\text{SnTe}(111)$ surface (top row in Fig. 5) is also seen in the Bi_2Te_3 half-space; more precisely, it shows weak but nonzero spectral weight in the deeper layers, for example in (d) and in (i).

The Dirac surface state of Bi_2Te_3 can be “buried,” that is, it is shifted from the outermost into deeper quintuple layers, by surface modification.¹⁸ Attaching a SnTe half-space to the surface of Bi_2Te_3 may be viewed as a drastic surface alteration, which suggests a “burying” of the Dirac state. Inspection of Figs. 6(f)–6(j), however, shows no indication of a shift to deeper layers.

B. Interface electronic structure of $\text{Sb}_2\text{Te}_3(111)/\text{Bi}_2\text{Te}_3(111)$

For comparison with $\text{SnTe}(111)/\text{Bi}_2\text{Te}_3(111)$, we calculated the electronic structure and its evolution with κ for $\text{Sb}_2\text{Te}_3(111)/\text{Bi}_2\text{Te}_3(111)$. Since both subsystems belong to the same class of topological insulators—both their \mathbb{Z}_2 invariants and mirror Chern numbers are identical—the Dirac surface states of the uncoupled systems annihilate upon contact.

For the uncoupled subsystems, we find the established Dirac surface states of $\text{Sb}_2\text{Te}_3(111)$ and $\text{Bi}_2\text{Te}_3(111)$ with their Dirac points at $\bar{\Gamma}$ [$\kappa = 0$, panels (a) and (e) in Fig. 7]. Increasing the coupling strength κ opens up band gaps at the Dirac points [(b) and (f)], whose widths increase with κ [e. g., (c) and (g)]. In other words, the lower and the upper part of the Dirac

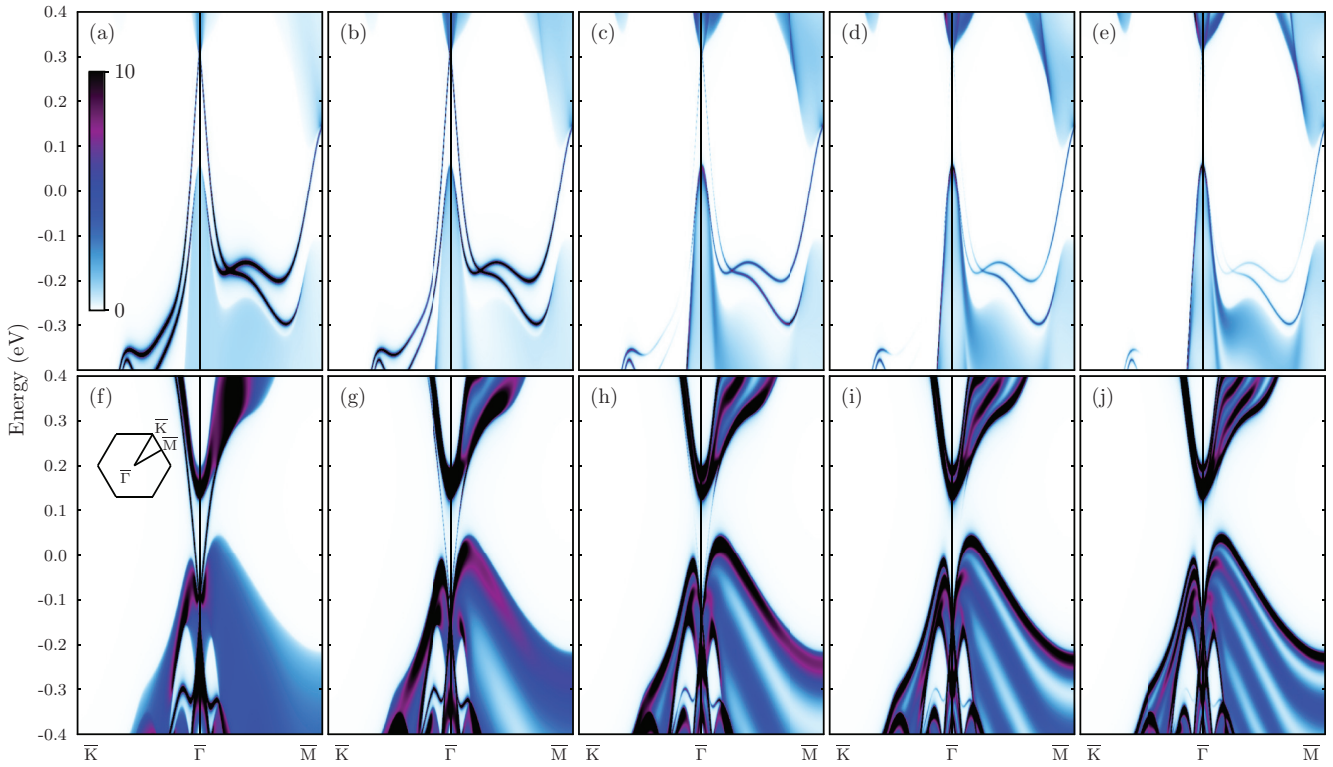


FIG. 5. (Color online) Localization of the surface states of SnTe(111) [top row, (a)–(e)] and Bi₂Te₃(111) [bottom row, (f)–(j)] for $\kappa = 0$ (i. e., uncoupled semi-infinite subsystems). For SnTe, spectral densities are shown for the second (a), the fourth (b), the seventh (c), the ninth (d), and the twelfth (e) double layer, counted from the surface. For Bi₂Te₃, spectral densities are shown for the first five quintuple layers, counted from the surface (f). The color scale in (a) gives the spectral density in states per eV; the two-dimensional Brillouin zone is sketched in (f).

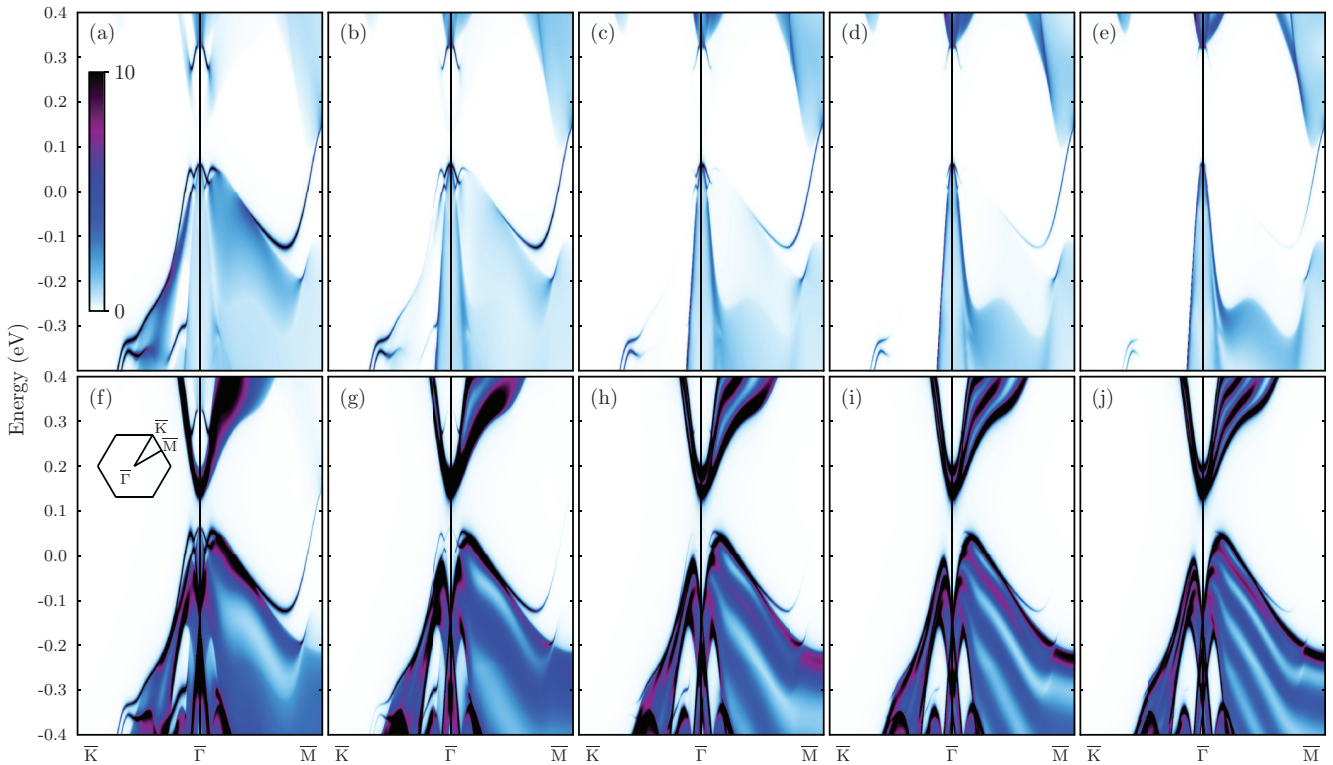


FIG. 6. (Color online) Localization of interface states of SnTe(111)/Bi₂Te₃(111) for $\kappa = 1$ (i. e., fully coupled semi-infinite subsystems). Panels and insets as in Fig. 5.

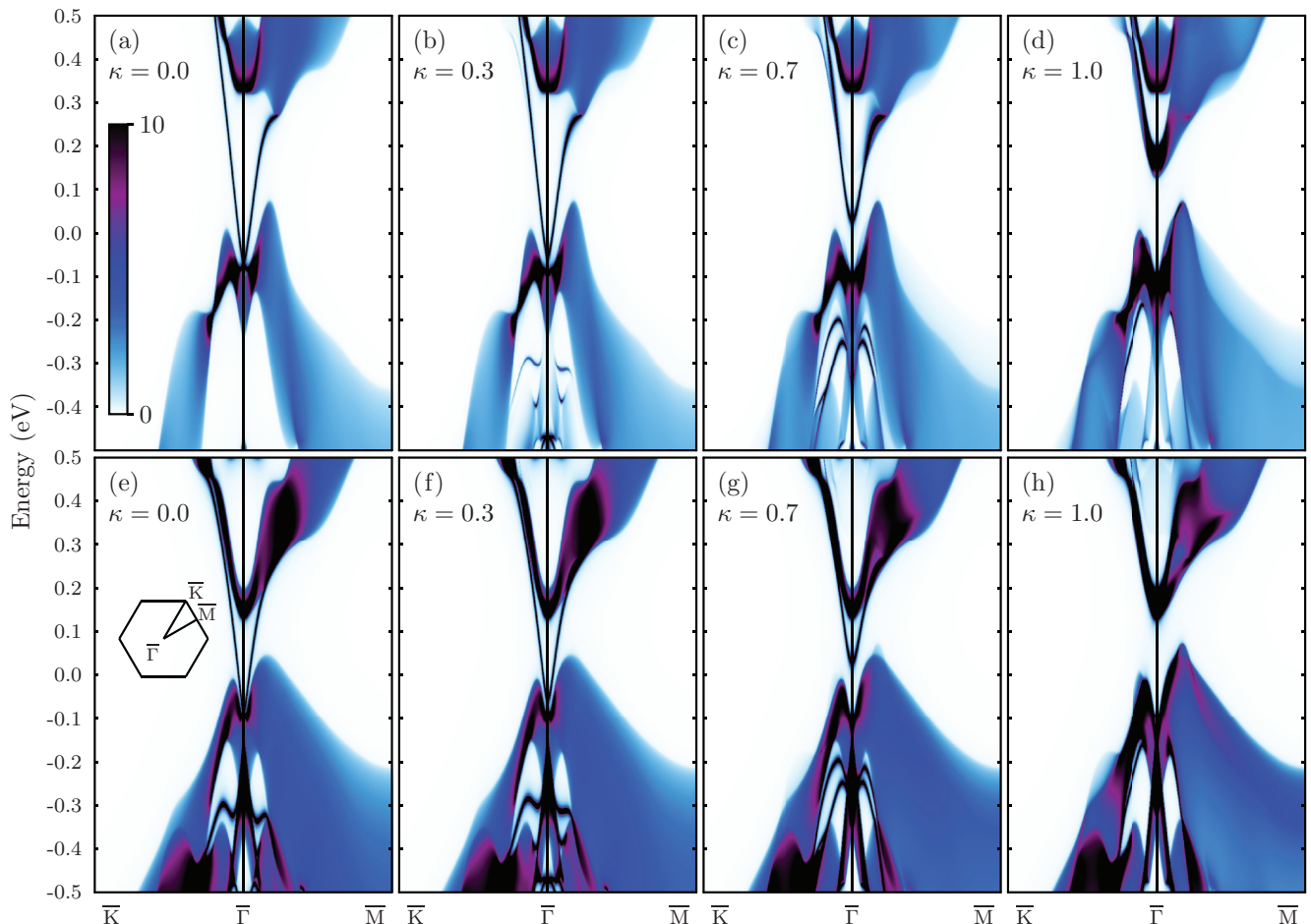


FIG. 7. (Color online) Interface electronic structure of $\text{Sb}_2\text{Te}_3(111)/\text{Bi}_2\text{Te}_3(111)$. Spectral densities of the outermost quintuple layers of Sb_2Te_3 [top row, (a)–(d)] and Bi_2Te_3 [bottom row, (e)–(h)] are shown for selected coupling strength κ , as indicated in each panel ($\kappa = 0$ for no coupling, i. e., separate surfaces; $\kappa = 1$ for fully coupled subsystems). The color scale in (a) gives the spectral density in states per eV; the two-dimensional Brillouin zone is sketched in (e).

cones detach; the lower part is shifted towards the valence bands while the upper part is shifted towards the conduction bands. For full coupling, $\kappa = 1$, the Dirac states are completely removed from the fundamental band gaps and merge with the bulk states, making the entire system insulating.

C. Sum rule for the Dirac states

The annihilation and survival of the Dirac states at a common interface with preserved mirror symmetry can be understood by means of a sum rule for the associated mirror Chern numbers.⁷ For Bi_2Te_3 and SnTe , the Bloch states with mirror eigenvalue $+i$ possess the Chern numbers $n_{\pm i}^{\text{BiTe}} = -1$ and $n_{\pm i}^{\text{SnTe}} = -2$, respectively. At the common interface, $n_{\pm i}^{\text{SnTe}} - n_{\pm i}^{\text{BiTe}} = -1$ holds, which indicates that one interface state with eigenvalue $+i$ survives. The same rule applies for the Bloch states with eigenvalue $-i$; thus, there exists one topologically protected interface state with this mirror eigenvalue, too.

Concerning Sb_2Te_3 and Bi_2Te_3 , $n_{\pm i}^{\text{SbTe}} = n_{\pm i}^{\text{BiTe}} = \mp 1$ holds because both subsystems show identical mirror Chern numbers. For the interface, this leads to $n_{\pm i}^{\text{BiTe}} - n_{\pm i}^{\text{SbTe}} = 0$ which

implies that Dirac states do not “survive,” in agreement with the electronic-structure calculations (Fig. 7).

IV. CONCLUDING REMARKS

The Dirac surface states of \mathcal{Z}_2 topological insulators are protected by time-reversal symmetry which makes them robust against structural disorder. In the present study, the remaining Dirac interface state is topologically protected by mirror symmetry because it is derived from the topological crystalline insulator SnTe . Hence, structural disorder which breaks the reflection symmetry would lead to opening of a band gap at the Dirac point. Since the Dirac point lies within the conduction bands, in-plane transport would be marginally affected by this band gap. Hence, a $\text{Bi}_2\text{Te}_3/\text{SnTe}(111)$ interface is expected suitable for future electronic applications. In a recent transport experiment on a $\text{SnTe}/\text{Bi}_2\text{Te}_3(111)$ pn junction,²⁶ a signature of a conducting interface channel has not been found, which is attributed to electric decoupling of the subsystems due to doping.

To experimentally prove our theoretical findings, one could think of a film geometry investigated by angle-resolved

photoelectron spectroscopy in the soft x-ray regime.⁴² This range of photon energies overcomes the too small electron mean free path in the vacuum ultraviolet range⁴³ and the too small photoionization cross sections in the hard x-ray regime, thus allowing Fermi surface mapping at the buried interface. Depth selectivity could be achieved by soft x-ray standing wave spectroscopy, e. g., Refs. 44 and 45. Considering spin-dependent transport, the interface state could be proven in $(\text{SnTe}/\text{Bi}_2\text{Te}_3)_n$ heterostructures: the conductance parallel to the interfaces increases with the number

of interfaces in steps of the conductance quantum. The spin polarization could be probed by the inverse spin Hall effect.⁴⁶

ACKNOWLEDGMENTS

We thank Silvia Picozzi and her group for fruitful discussions. This work is supported by the SPP 1666 “Topological Insulators” of DFG.

- ¹H. Hasan and C. Kane, *Rev. Mod. Phys.* **82**, 3045 (2010).
- ²L. Fu, *Phys. Rev. Lett.* **106**, 106802 (2011).
- ³J. E. Moore and L. Balents, *Phys. Rev. B* **75**, 121306(R) (2007).
- ⁴J. C. Y. Teo, L. Fu, and C. L. Kane, *Phys. Rev. B* **78**, 045426 (2008).
- ⁵W. Zhang, R. Yu, H.-J. Zhang, X. Dai, and Z. Fang, *New J. Phys.* **12**, 065013 (2010).
- ⁶S. R. Park, J. Han, C. Kim, Y. Y. Koh, C. Kim, H. Lee, H. J. Choi, J. H. Han, K. D. Lee, N. J. Hur *et al.*, *Phys. Rev. Lett.* **108**, 046805 (2012).
- ⁷R. Takahashi and S. Murakami, *Phys. Rev. Lett.* **107**, 166805 (2011).
- ⁸T. H. Hsieh, H. Lin, J. Liu, W. Duan, A. Bansil, and L. Fu, *Nat. Commun.* **3**, 982 (2012).
- ⁹Y. Tanaka, Z. Ren, K. Nakayama, S. Souma, T. Takahashi, K. Segawa, and Y. Ando, *Nat. Phys.* **8**, 800 (2012).
- ¹⁰T. Rauch, M. Flieger, J. Henk, I. Mertig, and A. Ernst, *Phys. Rev. Lett.* (to be published).
- ¹¹P. Barone, T. Rauch, D. Di Sante, J. Henk, I. Mertig, and S. Picozzi, *Phys. Rev. B* **88**, 045207 (2013).
- ¹²P. Pecheur and G. Toussaint, *J. Phys. Chem. Solids* **55**, 327 (1994).
- ¹³C. S. Lent, M. A. Bowen, J. D. Dow, and R. S. Allgaier, *Superlatt. Microstruct.* **2**, 491 (1986).
- ¹⁴N. Metropolis, A. W. Rosenbluth, M. N. Rosenbluth, and E. Teller, *J. Chem. Phys.* **21**, 1087 (1953).
- ¹⁵K. Binder and D. W. Heermann, *Monte Carlo Simulation in Statistical Physics: An Introduction*, 3rd ed. (Springer, Berlin, 1997).
- ¹⁶M. D. Jaffe and J. Singh, *Sol. State Commun.* **62**, 339 (1987).
- ¹⁷D. A. Papaconstantopoulos and M. J. Mehl, *J. Phys.: Condens. Matter* **15**, R413 (2003).
- ¹⁸S. V. Eremeev, G. Landolt, T. V. Menshchikova, B. Slomski, Y. M. Koroteev, Z. S. Aliev, D. M. Babanly, J. Henk, A. Ernst, L. Patthey *et al.*, *Nature Commun.* **3**, 635 (2012).
- ¹⁹J. Henk, A. Ernst, S. V. Eremeev, E. V. Chulkov, I. V. Maznichenko, and I. Mertig, *Phys. Rev. Lett.* **108**, 206801 (2012).
- ²⁰J. Henk, M. Flieger, I. V. Maznichenko, I. Mertig, A. Ernst, S. V. Eremeev, and E. V. Chulkov, *Phys. Rev. Lett.* **109**, 076801 (2012).
- ²¹M. P. López Sancho, J. M. L. Sancho, and J. Rubio, *J. Phys. F: Met. Phys.* **15**, 851 (1985).
- ²²J. Henk and W. Schattke, *Comput. Phys. Commun.* **77**, 69 (1993).
- ²³A. Bödicker, W. Schattke, J. Henk, and R. Feder, *J. Phys.: Condens. Matter* **6**, 1927 (1994).
- ²⁴R. Feder and K. Sturm, *Phys. Rev. B* **12**, 537 (1975).
- ²⁵W. Harrison, *Electronic Structure and the Properties of Solids* (W. H. Freeman, San Francisco, 1980).
- ²⁶A. A. Taskin, S. Sasaki, K. Segawa, and Y. Ando, [arXiv:1305.2470](https://arxiv.org/abs/1305.2470) [cond-mat.mes-hall].
- ²⁷J. Pollmann and S. T. Pantelides, *Phys. Rev. B* **18**, 5524 (1978).
- ²⁸H. M. Benia, A. Yaresko, A. P. Schnyder, J. Henk, C. T. Lin, K. Kern, and C. R. Ast, *Phys. Rev. B* **88**, 081103 (2013).
- ²⁹J. McCaldin, T. McGill, and C. Mead, *Phys. Rev. Lett.* **36**, 56 (1976).
- ³⁰W. R. Frensley and H. Kroemer, *Phys. Rev. B* **16**, 2642 (1977).
- ³¹S. P. Kowalczyk, W. J. Schaffer, E. A. Kraut, and R. W. Grant, *J. Vac. Sci. Tech.* **20**, 705 (1982).
- ³²L. Fu and C. L. Kane, *Phys. Rev. B* **74**, 195312 (2006).
- ³³T. Fukui and Y. Hatsugai, *J. Phys. Soc. Jpn.* **76**, 053702 (2007).
- ³⁴E. Prodan, *Phys. Rev. B* **80**, 125327 (2009).
- ³⁵T. Inui, Y. Tanabe, and Y. Onodera, *Group Theory and Its Applications in Physics*, Springer Series in Solid State Sciences Vol. 78 (Springer, Berlin, 1990).
- ³⁶L. Fu, *Phys. Rev. Lett.* **103**, 266801 (2009).
- ³⁷F. Reinert, *J. Phys.: Condens. Matter* **15**, S693 (2003).
- ³⁸C. R. Ast, J. Henk, A. Ernst, L. Moreschini, M. C. Falub, D. Pacilé, P. Bruno, K. Kern, and M. Grioni, *Phys. Rev. Lett.* **98**, 186807 (2007).
- ³⁹M. König, S. Wiedmann, C. Brüne, A. Roth, H. Buhmann, L. W. Molenkamp, X.-L. Qi, and S.-C. Zhang, *Science* **318**, 766 (2007).
- ⁴⁰O. V. Yazyev, J. E. Moore, and S. G. Louie, *Phys. Rev. Lett.* **105**, 266806 (2010).
- ⁴¹E. Simon, A. Szilva, B. Ujfalussy, B. Lazarovits, G. Zarand, and L. Szunyogh, *Phys. Rev. B* **81**, 235438 (2010).
- ⁴²G. Berner, M. Sing, H. Fujiwara, A. Yasui, Y. Saitoh, A. Yamasaki, Y. Nishitani, A. Sekiyama, N. Pavlenko, T. Kopp *et al.*, *Phys. Rev. Lett.* **110**, 247601 (2013).
- ⁴³M. P. Seah and W. A. Dench, *Surf. Interf. Anal.* **1**, 2 (1979).
- ⁴⁴S.-H. Yang, B. S. Mun, N. Mannella, S.-K. Kim, J. B. Kortright, J. Underwood, F. Salmassi, E. Arenholz, A. Young, Z. Hussain *et al.*, *J. Phys.: Condens. Matter* **14**, L407 (2002).
- ⁴⁵A. X. Gray, J. Minár, L. Plucinski, M. Huijben, A. Bostwick, E. Rotenberg, S.-H. Yang, J. Braun, A. Winkelmann, G. Conti, D. Eiteneer, A. Rattanachata, A. A. Greer, J. Ciston, C. Ophus, G. Rijnders, D. H. A. Blank, D. Doennig, R. Pentcheva, J. B. Kortright, C. M. Schneider, H. Ebert, and C. S. Fadley, *EuroPhys. Lett.* **104**, 17004 (2013).
- ⁴⁶K. Ando and E. Saitoh, *Nat. Commun.* **3**, 629 (2012).
- ⁴⁷J. Liu, W. Duan, and L. Fu, [arXiv:1304.0430](https://arxiv.org/abs/1304.0430) [cond-mat.mtrl-sci].
- ⁴⁸We recall that a slab geometry results in band gaps that are brought about by quantization of the wave vector perpendicular to the layers

(“quantum confinement”). These artificial gaps could falsify the topological character of the surface or interface states.

⁴⁹Termination by Sn atoms instead of Te atoms shifts the Dirac points from the conduction band edge to the valence-band edge;

our calculations for Sn-terminated SnTe(111) confirm the results presented in Fig. 2 of Ref.[47](#).

⁵⁰Due to spin-orbit coupling, the parity of the spatial part of a wave function and its spin polarization are entangled.³⁵

6.5 SPIN CHIRALITY TUNING AND TOPOLOGICAL SEMIMETALS IN STRAINED $\text{HgTe}_x\text{S}_{1-x}$

The last publication [TR1] may be regarded as the central one, in a way it summarizes the contents of the whole thesis. We managed to predict different insulating and metallic topological phases – by calculating their topological invariants and surface state properties – in one system: $\text{HgTe}_x\text{S}_{1-x}$ under strain. Nearly all the features of the TB code developed for the thesis, such as the modelling of strain and disorder, were used in this work.

The starting points were the ideal HgTe and HgS. HgTe is a semimetal but the bands are inverted at the Fermi energy. Therefore, opening up a band gap, e.g., by strain in an appropriate direction, can make HgTe a TI. In contrast, HgS is already a TI, even without strain. This is due to an unusual ordering of the Γ_7 and Γ_8 bands. Γ_7 being energetically above Γ_8 can be described by an effective negative SOC constant for the p bands. This effect comes from a hybridization with the d bands which favour $E(\Gamma_7) > E(\Gamma_8)$.

A very interesting implication from the negative SOC constant is the opposite spin chirality of the surface state of HgS, compared with most of the other TIs, such as the chalcogenides. There are very few TIs with this property found so far.

Based on these ideas, we carried out a series of calculations to simulate the effects of mixing HgTe and HgS. In addition, we applied uniaxial strain α in the (001) direction, accompanied by an opposite strain β in the plane perpendicular to the (001) direction. For the parameters $x \in [0; 1]$ and $\beta \in [0.97; 1.03]$ we calculated the \mathcal{Z}_2 invariant and the mirror Chern number, provided the system showed an insulating band gap. For all parameters the surface electronic structure for both surface terminations (Hg and $\text{Te}_x\text{S}_{1-x}$) of the (001) surface was calculated.

As a first result we confirmed that both HgS and strained HgTe ($\beta > 1.0$) are TIs with \mathcal{Z}_2 invariants (1; 000) but a different mirror Chern number; $n_M = -1$ for HgTe and $n_M = +1$ for HgS. This was further confirmed by the opposite spin chirality of the surface states of both materials. These two topological phases occupy large regions of the phase diagram and they touch at $\beta = 1.0$ and $x \approx 0.15$, where the effective p SOC vanishes, see Fig. 1 in [TR1].

Surprisingly, we also found two different semimetallic topological phases. Applying tensile strain in (001) direction to HgTe ($\beta < 1.0$, $x = 1.0$) opens up a band gap at the Γ point, but there is still a crossing of the bands on the Γ -Z line in the BZ. The system becomes a topological Dirac semimetal (TDS), which is confirmed by the \mathcal{Z}_2 invariant $\nu = 1$ for the $k_z = 0$ plane in the BZ. The corresponding surface states are visible at a surface perpendicular to this plane, e.g., the (100) surface. The results of a surface electronic structure calculation featuring both surface and bulk Dirac states are shown in Fig. 6.2, not shown in the publication.

A second topological semimetallic phase – the Weyl semimetal (WSM) – was found near the $x \approx 0.15$ line (vanishing SOC) for $\beta > 1.0$. Exactly as shown in Fig. 5.2 a), the two distinct TI phases with different mirror Chern numbers are separated by a finite region, the WSM phase. In $\text{HgTe}_x\text{S}_{1-x}$ a total of eight Weyl points were found, all located in the k_x - k_y plane. For each of them the topological charge or Chern number was calculated, by integrating the Berry curvature on a small sphere in k space surrounding the Weyl points, getting +1 or -1 as a result. The surface electronic structure of the (001) surface shows surface states, whose Fermi energy cuts are the Fermi arcs. For both terminations, four Fermi arcs connect the eight Weyl point projections. Each Fermi

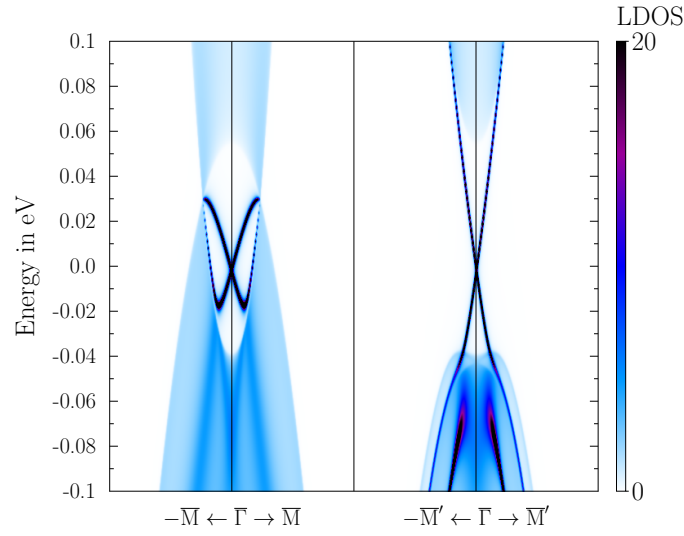


Figure 6.2: Surface electronic structure of the (100) surface ($\text{Te}_x\text{S}_{1-x}$ termination) of strained ($\beta = 0.97$) HgTe along two perpendicular directions in the surface BZ. In both figures a Dirac cone like surface state can be seen. In addition, the projections of the bulk Dirac cones onto the surface are visible in the left figure.

arc connects two Weyl point projections with opposite Chern number. Interestingly, by considering a real material with both top and bottom surface, the Fermi energy cut of the whole material consists of an overlay of the calculations for both surfaces. Then, the usual picture of Fermi lines being closed is restored, as different pairs of Weyl point projections are connected by one Fermi arc at differently terminated surfaces.

Spin Chirality Tuning and Topological Semimetals in Strained $\text{HgTe}_x\text{S}_{1-x}$

Tomáš Rauch,^{1,*} Steven Achilles,¹ Jürgen Henk,¹ and Ingrid Mertig^{1,2}

¹*Institute of Physics, Martin Luther University Halle-Wittenberg, Von-Seckendorff-Platz 1, 06120 Halle (Saale), Germany*

²*Max Planck Institute of Microstructure Physics, Weinberg 2, 06120 Halle (Saale), Germany*

(Received 10 March 2015; published 12 June 2015)

By means of detailed electronic structure calculations, we show that strained $\text{HgTe}_x\text{S}_{1-x}$ alloys show a surprisingly rich topological phase diagram. In the strong topological insulator phase, the spin chirality of the topological nontrivial surface states can be reversed by adjusting the alloy concentration x and the strain. On top of this, we predict two semimetallic topological phases, namely, a Dirac semimetal and a Weyl semimetal. The topological phases are characterized by their \mathcal{Z}_2 invariants and their mirror Chern numbers.

DOI: 10.1103/PhysRevLett.114.236805

PACS numbers: 73.20.At, 71.70.Ej, 71.70.Fk, 73.43.-f

Introduction.—Topological insulators (TIs) are bulk insulators that possess a topologically nontrivial band structure. As a consequence, these materials host spin-polarized and topologically protected surface states that cross the fundamental band gap [1,2]. Experimental and theoretical investigations have focused on \mathcal{Z}_2 TIs and on topological crystalline insulators (TCIs). The former exist if time-reversal symmetry is unbroken; they are characterized by the \mathcal{Z}_2 topological invariant ν and show an odd number of band inversions at time-reversal invariant momenta in the bulk Brillouin zone [3–5]. Probably the most prominent three-dimensional TIs in this class are the Bi chalcogenides, e.g., Bi_2Se_3 and Bi_2Te_3 [6]. Topological crystalline insulators, on the other hand, rely on unbroken crystal symmetries [7], typically a mirror symmetry. A prominent topological crystalline insulator is SnTe [8]. The relevant topological invariant is the mirror Chern number. Topologically nontrivial surface states show up on any surface perpendicular to the mirror plane. Their Dirac points are then located on the line that is the intersection of the mirror plane with the surface Brillouin zone (BZ). It turned out that some compounds fall into both classes; for example, Bi_2Te_3 is both a TI and a TCI [9].

A mirror Chern number provides information on both the number and the spin chirality of the topologically nontrivial surface states. More precisely, its modulus gives the number of topologically nontrivial surface states, whereas its sign tells whether their spin chirality is clockwise or anticlockwise in the upper part of the Dirac cone [5]. Topological insulators investigated so far have a clockwise spin chirality, which is explained by the orbital composition of the surface states: the Dirac cones are composed mostly of orbitals aligned normal to the surface (e.g., p_z orbitals) [10]. In contrast, surface-parallel orbitals (e.g., p_x and p_y) favor anticlockwise chirality. Furthermore, one can attribute a positive (negative) spin-orbit coupling constant with clockwise (anticlockwise) spin chirality to p orbitals. These considerations immediately suggest studying the properties

of TIs with anticlockwise spin chirality [11]. On top of this, it is desirable to tune the spin chirality, which is important for applications.

Among the first systems investigated in this context are HgTe quantum wells sandwiched between CdTe layers [12,13]. Strained HgTe films are three-dimensional TIs with clockwise spin chirality [14–17]. The similar compound HgS is a TI as well [18], even if unstrained, but its spin chirality is opposite to that of HgTe [20–22]; such an effective negative spin-orbit coupling is acquired by hybridization of the p orbitals with energetically close d orbitals [23].

In this Letter, we report on strained alloys with the zinc blende structure. We show theoretically that the spin chirality of $\text{HgTe}_x\text{S}_{1-x}$ compounds can be tuned, that is reversed, by application of moderate strain in the [001] direction, and by changing the composition x . Moreover, these materials exhibit a surprisingly rich topological phase diagram that not only shows TCIs but also topological semimetals: a Weyl semimetal [24] and a Dirac semimetal phase [25]. Thus, the topological properties and, consequently, the spin-dependent transport properties of these systems can be adjusted by two external parameters: strain and composition. These findings are important for both device applications and fundamental condensed-matter physics.

Theoretical.—In an initial step, we performed first-principles electronic structure calculations [26] based on the multiple-scattering theoretical formulation of density functional theory (DFT) [34]. We applied the generalized gradient approximation as introduced by Perdew *et al.* (Ref. [35]). Our homemade Korringa-Kohn-Rostoker computer program package [36–38] accounts for relativistic effects, in particular the essential spin-orbit interaction, by solving the Dirac equation. The lattice constants for HgTe (6.461 Å) and HgS (5.850 Å) are chosen to match the experimental lattice parameters [39,40]. The DFT band structure of HgTe fits very well to the angle-resolved

photoelectron spectroscopy measurements [14,41,42] near the Γ point of the BZ. Since HgS is very similar to HgTe, we believe that we also get the correct band structure for this case.

Subsequently, tight-binding parametrizations in the Slater-Koster framework [43] were obtained using the DFT results as input. The parameters have been optimized by Monte Carlo simulations [44]. These tight-binding Hamiltonians are then used for all further calculations.

The $\text{HgTe}_x\text{S}_{1-x}$ alloys were simulated by the virtual crystal approximation and the coherent potential approximation (CPA) [45,46], both giving similar results. A strain α in the [001] direction accompanied by an opposite strain β in the in-plane directions was applied; the volume of the unit cell is not conserved. The elastic constants for HgTe and HgS taken from Ref. [47] were linearly interpolated with the concentration x .

Both HgTe and HgS crystallize in the zinc blende structure, which lacks inversion symmetry. The (001) surface is terminated either by a Hg or by a $\text{Te}_x\text{S}_{1-x}$ layer. The surface electronic structure has been calculated for semi-infinite systems using Green function renormalization [48]. The dispersion, spin texture, and orbital composition of the surface states are obtained from the layer-resolved spectral density.

For building up a topological phase diagram, we varied the concentration x from 0 to 1 in steps of 0.1 and the strain β from 0.97 to 1.03 in steps of 0.01. For all nonmetallic systems we calculated the \mathcal{Z}_2 invariant and the mirror Chern numbers c_m for the two mirror planes perpendicular to the (001) surface, using the virtual crystal approximation. The phase diagram shows five topological phases, which are discussed in the following (Fig. 1).

Spin chirality tuning.—Unstrained HgTe is a semimetal: at the BZ center Γ the bulk bands at the Fermi level are

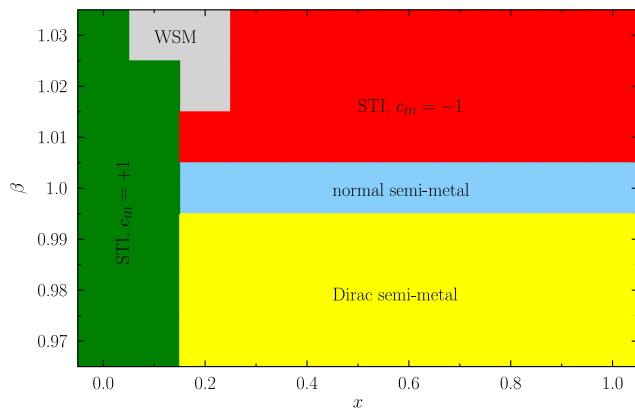


FIG. 1 (color online). Topological phase diagram of strained $\text{HgTe}_x\text{S}_{1-x}$ alloys. Parameters are the concentration x and the strain β . The phases are indicated by colors: strong TI (STI) with mirror Chern number $c_m = -1$ (red), strong TI with $c_m = +1$ (green), Dirac semimetal (yellow), Weyl semimetal (WSM) (gray), and normal semimetal (blue).

fourfold degenerate and are inverted; that is, the Γ_6 band has a lower energy than the Γ_8 band [15,16]. This degeneracy is lifted by positive in-plane strain ($\beta > 1$), making HgTe a strong TI with \mathcal{Z}_2 invariant $\nu = (1; 0, 0, 0)$ and a TCI with mirror Chern number $c_m = -1$. Hence, positively strained HgTe is a TI with clockwise spin chirality. The computed surface electronic structure (Fig. 2) fits well to that of Wu *et al.* (Ref. [17]). Thus, our approach reproduces the topological aspects reported earlier.

HgS is a strong TI with counterclockwise spin chirality [20,21,49], which is confirmed by our calculations: $\nu = (1; 0, 0, 0)$ and $c_m = +1$. The spectral density of the S -terminated (001) surface hosts a topological nontrivial surface state at $\bar{\Gamma}$ whose spin chirality is opposite to that of strained HgTe (Fig. 2). Application of both positive and negative in-plane strain does not change the topological properties (green area in Fig. 1).

With two similar systems but with opposite spin chirality at hand, one is able to tune—more precisely, reverse—the spin texture of the topologically nontrivial surface state by alloying. The topological phase transition $c_m = -1 \leftrightarrow +1$ is accompanied by a closing of the fundamental band gap and by a vanishing effective spin-orbit coupling. For the unstrained alloy $\text{HgTe}_x\text{S}_{1-x}$ this transition takes place at the critical concentration $x_c \approx 0.15$, for which the p bands are sixfold degenerate at Γ , indicating a semimetallic system. Calculations performed within the coherent potential approximation instead of the virtual crystal approximation yield an x_c of about 0.20. These numbers set the approximate range for experimental realization of the spin chirality

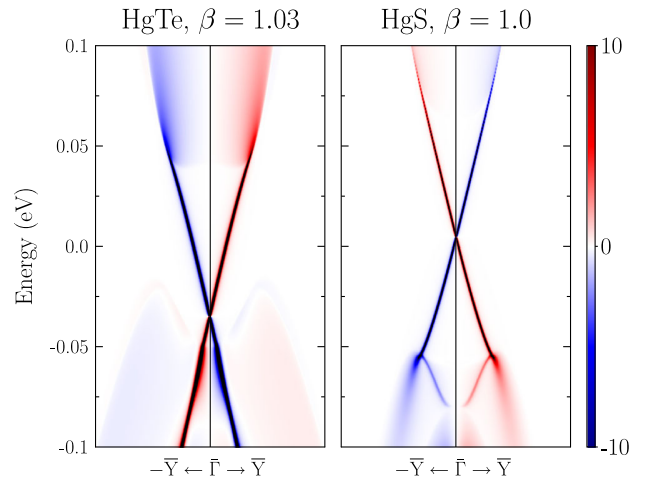


FIG. 2 (color online). Surface electronic structures of positively strained HgTe (left, $\beta = 1.03$) and unstrained HgS (right), with Te- or S-terminated (001) surfaces, respectively. The spin-resolved spectral density of the topmost layer is shown along a part of the $\bar{Y}-\bar{\Gamma}-\bar{Y}$ line of the surface Brillouin zone. The so-called Rashba component of the spin polarization (in plane, perpendicular to the wave vector) is given by the color scale with red positive and blue negative, in states per eV.

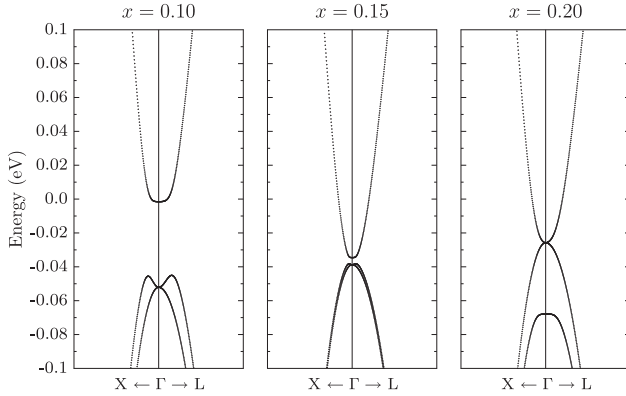


FIG. 3. Bulk band structures of unstrained $\text{HgTe}_x\text{S}_{1-x}$ for $x = 0.10$ (left), $x = 0.15$ (center), and $x = 0.20$ (right). The spin-orbit coupling almost vanishes at $x = 0.15$, and the system is close to the phase transition. One fifth of the $X-\Gamma$ and the $\Gamma-L$ lines is shown.

reversal. The bulk band structure near the phase transition is shown in Fig. 3.

Upon the application of strain to $\text{HgTe}_x\text{S}_{1-x}$ two topological semimetallic phases emerge: a Dirac semimetal and a Weyl semimetal.

Dirac semimetal.—This phase shows up for positive spin-orbit coupling (SOC) and negative strain (yellow area in Fig. 1). The application of negative strain to HgTe splits the degeneracy at Γ but, in contrast to positive strain, there is no fundamental band gap. More precisely, the valence and conduction bands touch at two points on the $Z-\Gamma-Z$ line, forming a pair of Dirac points (Fig. 4). The associated wave vectors are connected with each other by time-reversal symmetry [here $\mathbf{k} = (0, 0, \pm k_z)$]. The respective \mathcal{Z}_2 invariant ν_z is thus calculated for the plane with $\mathbf{k} = (k_x, k_y, 0)$ (Ref. [25]). Owing to the zinc blende lattice, the $k_z = 0$ plane is not a mirror plane of the sample, leading to $\nu_z = 1$, which indicates that positively strained HgTe is a topological Dirac semimetal. Any surface perpendicular to

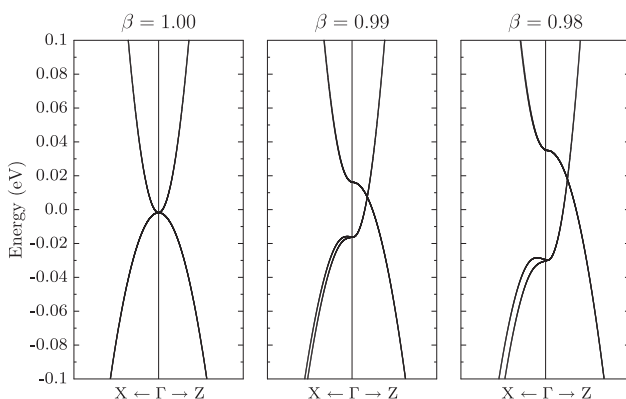


FIG. 4. Bulk band structure of negatively strained HgTe. The Dirac point on the $\Gamma-Z$ line shows up for $\beta < 1$. One fifth of the $X-\Gamma$ and the $\Gamma-Z$ lines is shown.

the $k_z = 0$ plane features both topologically protected bulk and surface states (not shown here).

Weyl semimetal.—This phase requires either broken time-reversal symmetry or broken inversion symmetry (as is the case for a zinc blende lattice). In a Weyl semimetal, the fundamental band gap does not reopen immediately at the phase transition; instead, each point at which the valence and the conduction band touch splits into a pair of Weyl points that carry opposite topological charges (Chern numbers ± 1). The associated topologically nontrivial surface states connect the projections of the Weyl points in the bulk onto the surface BZ, leading to so-called Fermi arcs with unique transport properties. These fascinating features are investigated with great effort [50–53].

For positively strained $\text{HgTe}_x\text{S}_{1-x}$, we found Weyl semimetal phases in a region of concentrations with small effective SOC. Starting at $\beta = 1.03$ and $x = 0.0$ (HgS) in the topological phase diagram (gray area in Fig. 1), a phase transition takes place at $x_c \approx 0.08$. There, the valence and conduction bands touch at four points on the $\Gamma-K$ lines, which are cuts of the $k_z = 0$ plane with the (110) or the $(1\bar{1}0)$ mirror plane in the BZ, respectively. Hence, there is a fourfold degeneracy at these points. Upon increasing x , these points split into pairs of twofold degenerate touching points; the bands there disperse linearly, forming Dirac cones. The topological charges associated with these Weyl points are calculated to be ± 1 .

These bulk properties are nicely supported by the electronic structure of the (001) surface (Fig. 5). For Fermi energy cuts, the spectral densities show Fermi arcs that connect projections of the Weyl points onto the surface BZ. A further increase of x shifts the Weyl points within the $k_z = 0$ plane towards the $\Gamma-X$ lines. The four pairs touch (but do not recombine because the touching Weyl points possess the same topological charge), exactly for vanishing SOC ($x_c \approx 0.15$). For positive SOC ($x > 0.15$), the Weyl

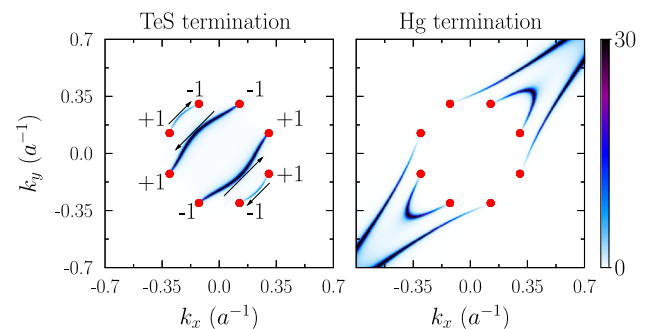


FIG. 5 (color online). Electronic structure of the (001) surface of positively strained $\text{HgTe}_{0.11}\text{S}_{0.89}$ with $\beta = 1.03$. The spectral density of the topmost layer is given by the color scale (in states per eV). Left: TeS termination. Right: Hg termination. Red dots mark the position of the Weyl points on the surface BZ; their topological charges ± 1 are indicated. The arrows sketch the spin polarization. a is the lattice constant.

points emerge again. The Fermi arcs have a reversed spin polarization, owing to the change of sign of the SOC. Eventually, at $x \approx 0.24$, the pairs of Weyl points recombine at the mirror lines and the system enters the strong TI phase for $x > 0.24$.

It turned out that the Fermi arcs connect different pairs of Weyl points, depending on the surface terminations (Fig. 5). The Fermi arcs are reminiscent of Dirac strings that connect oppositely charged Dirac monopoles; this picture is supported by the spin polarization that follows a Fermi arc's line (arrows in Fig. 5).

Concluding remarks.—Strained $\text{HgTe}_x\text{S}_{1-x}$ alloys show a surprisingly rich topological phase diagram: besides a reversal of the spin chirality in the strong topological insulator phase, we predict two semimetallic topological phases, namely, a Dirac semimetal and a Weyl semimetal. These findings call for experimental verification, for example, by spin- and angle-resolved photoelectron spectroscopy [54,55]. In transport measurements, all the phases would have different signatures. In Weyl semimetals, the surface contribution should be highly anisotropic because of the shape of the Fermi arcs, which could be detected by surface sensitive measurements. In contrast, the anisotropy should nearly vanish in topological Dirac semimetals, since the Fermi lines are closed. Finally, for the STI phases, the bulk contribution should vanish because of the insulating bulk nature. This would not be the case in the semimetallic phases.

Positive or negative strain may be introduced by appropriate substrates, as is successfully done for HgTe sandwiched between CdTe (Ref. [14]). With the assumption that the lattice constant of $\text{HgTe}_x\text{S}_{1-x}$ varies linearly with x , we propose GaSb with a lattice constant of 6.1 \AA [56] as a substrate for the Weyl semimetal phase. To achieve the topological Dirac semimetal phase, we propose $\text{Cd}_{0.7}\text{Zn}_{0.3}\text{Te}$ (lattice constant 6.364 \AA [57]) as a suitable substrate. Figure S3 of the Supplemental Material [58] provides in-plane lattice constants for the entire topological phase diagram.

In our work, the alloy was simulated mainly by the virtual crystal approximation. A big advantage is the possibility of calculating the topological invariants from eigenstates and eigenvalues combined with the fact that we do not need to construct large supercells. In the DFT approach, different methods for simulating alloys are possible. One is to construct a supercell, where the atoms of compound A are exchanged by compound B according to the given concentration. The system is then lattice periodic. The biggest disadvantage of this approach is the need for large supercells, which can become computationally demanding. It was used to calculate, e.g., the properties of $\text{Hg}_x\text{Zn}_{1-x}\text{Te}$ [15], which is similar to the system we investigate. Another possibility is the CPA. Since this method is based on a Green function approach, it is well suited for our Korringa-Kohn-Rostoker package.

The next step would be to calculate the properties of alloys using the CPA directly within DFT.

We thank Binghai Yan for fruitful discussions. This work is supported by the Priority Program SPP 1666 of Deutsche Forschungsgemeinschaft (DFG).

*Corresponding author.

tomas.rauch@physik.uni-halle.de

- [1] M. Z. Hasan and C. Kane, *Rev. Mod. Phys.* **82**, 3045 (2010).
- [2] M. Z. Hasan and J. E. Moore, *Annu. Rev. Condens. Matter Phys.* **2**, 55 (2011).
- [3] C. L. Kane and E. J. Mele, *Phys. Rev. Lett.* **95**, 146802 (2005).
- [4] L. Fu, C. Kane, and E. Mele, *Phys. Rev. Lett.* **98**, 106803 (2007).
- [5] J. C. Y. Teo, L. Fu, and C. L. Kane, *Phys. Rev. B* **78**, 045426 (2008).
- [6] H. Zhang, C.-x. Liu, X.-l. Qi, X. Dai, Z. Fang, and S.-C. Zhang, *Nat. Phys.* **5**, 438 (2009).
- [7] L. Fu, *Phys. Rev. Lett.* **106**, 106802 (2011).
- [8] T. H. Hsieh, H. Lin, J. Liu, W. Duan, A. Bansil, and L. Fu, *Nat. Commun.* **3**, 982 (2012).
- [9] T. Rauch, M. Flieger, J. Henk, I. Mertig, and A. Ernst, *Phys. Rev. Lett.* **112**, 016802 (2014).
- [10] H. Zhang, C.-X. Liu, and S.-C. Zhang, *Phys. Rev. Lett.* **111**, 066801 (2013).
- [11] R. Takahashi and S. Murakami, *Phys. Rev. Lett.* **107**, 166805 (2011).
- [12] B. A. Bernevig, T. L. Hughes, and S.-C. Zhang, *Science* **314**, 1757 (2006).
- [13] M. König, S. Wiedmann, C. Brüne, A. Roth, H. Buhmann, L. W. Molenkamp, X.-L. Qi, and S.-C. Zhang, *Science* **318**, 766 (2007).
- [14] C. Brüne, C. X. Liu, E. G. Novik, E. M. Hankiewicz, H. Buhmann, Y. L. Chen, X. L. Qi, Z. X. Shen, S. C. Zhang, and L. W. Molenkamp, *Phys. Rev. Lett.* **106**, 126803 (2011).
- [15] S. Zaheer, S. M. Young, D. Cellucci, J. C. Y. Teo, C. L. Kane, E. J. Mele, and A. M. Rappe, *Phys. Rev. B* **87**, 045202 (2013).
- [16] F. Viot, R. Hayn, M. Richter, and J. van den Brink, *Phys. Rev. Lett.* **111**, 146803 (2013).
- [17] S.-C. Wu, B. Yan, and C. Felser, *Europhys. Lett.* **107**, 57006 (2014).
- [18] It has to be noted that HgS has also been found to be a normal insulator with negative SOC [19].
- [19] A. Svane, N. E. Christensen, M. Cardona, A. N. Chantis, M. van Schilfhaarde, and T. Kotani, *Phys. Rev. B* **84**, 205205 (2011).
- [20] F. Viot, R. Hayn, M. Richter, and J. van den Brink, *Phys. Rev. Lett.* **106**, 236806 (2011).
- [21] A. Delin, *Phys. Rev. B* **65**, 153205 (2002).
- [22] B. Al Shafaay, F. El Haj Hassan, and M. Korek, *Comput. Mater. Sci.* **83**, 107 (2014).
- [23] J. Vidal, X. Zhang, V. Stevanović, J.-W. Luo, and A. Zunger, *Phys. Rev. B* **86**, 075316 (2012).
- [24] X. Wan, A. M. Turner, A. Vishwanath, and S. Y. Savrasov, *Phys. Rev. B* **83**, 205101 (2011).
- [25] B.-J. Yang and N. Nagaosa, *Nat. Commun.* **5**, 4898 (2014).

- [26] Details of the computations are provided in the Supplemental Material [58], which includes Refs. [27–33].
- [27] W. A. Harrison, *Elementary Electronic Structure*, rev. ed. (World Scientific, New Jersey, 2004).
- [28] T. Fukui and Y. Hatsugai, *J. Phys. Soc. Jpn.* **76**, 053702 (2007).
- [29] L. Fu and C. Kane, *Phys. Rev. B* **74**, 195312 (2006).
- [30] R. Yu, X. L. Qi, A. Bernevig, Z. Fang, and X. Dai, *Phys. Rev. B* **84**, 1 (2011).
- [31] E. Prodan, *Phys. Rev. B* **80**, 125327 (2009).
- [32] D. J. Thouless, M. Kohmoto, M. P. Nightingale, and M. den Nijs, *Phys. Rev. Lett.* **49**, 405 (1982).
- [33] A. Bödicker, W. Schattke, J. Henk, and R. Feder, *J. Phys. Condens. Matter* **6**, 1927 (1994).
- [34] P. Hohenberg and W. Kohn, *Phys. Rev.* **136**, B864 (1964).
- [35] J. P. Perdew, K. Burke, and M. Ernzerhof, *Phys. Rev. Lett.* **77**, 3865 (1996).
- [36] J. Koringa, *Physica (Amsterdam)* **13**, 392 (1947).
- [37] W. Kohn and N. Rostoker, *Phys. Rev.* **94**, 1111 (1954).
- [38] M. Gradhand, M. Czerner, D. V. Fedorov, P. Zahn, B. Y. Yavorsky, L. Szunyogh, and I. Mertig, *Phys. Rev. B* **80**, 224413 (2009).
- [39] T. Skauli and T. Colin, *J. Cryst. Growth* **222**, 719 (2001).
- [40] H. Aimin, G. Chunxiao, L. Ming, H. Chunyuan, H. Xiaowei, Z. Dongmei, Y. Cuiling, L. Hongwu, M. Yanzhang, T. Yongjun, and Z. Guangtian, *J. Phys. Condens. Matter* **19**, 425222 (2007).
- [41] O. Crauste, Y. Ohtsubo, P. Ballet, P. Delplace, D. Carpentier, T. Meunier, A. Taleb-ibrahimi, and L. P. Lévy, [arXiv:1307.2008v1](https://arxiv.org/abs/1307.2008v1).
- [42] S. H. Yao, B. Zhou, M. H. Lu, Z. K. Liu, Y. B. Chen, J. G. Analytis, C. Brüne, W. H. Dang, S.-K. Mo, Z.-X. Shen, I. R. Fisher, L. W. Molenkamp, H. L. Peng, Z. Hussain, and Y. L. Chen, *Phys. Status Solidi RRL* **7**, 130 (2013).
- [43] J. C. Slater and G. F. Koster, *Phys. Rev.* **94**, 1498(1954).
- [44] N. Metropolis, A. W. Rosenbluth, M. N. Rosenbluth, A. H. Teller, and E. Teller, *J. Chem. Phys.* **21**, 1087 (1953).
- [45] P. M. Laufer and D. A. Papaconstantopoulos, *Phys. Rev. B* **35**, 9019 (1987).
- [46] J. S. Faulkner, *Phys. Rev. B* **13**, 2391 (1976).
- [47] S. Adachi, *Properties of Semiconductor Alloys* (Wiley, New York, 2009).
- [48] J. Henk and W. Schattke, *Comput. Phys. Commun.* **77**, 69 (1993).
- [49] Q.-Z. Wang, S.-C. Wu, C. Felser, B. Yan, and C.-X. Liu, *Phys. Rev. B* **91**, 165435 (2015).
- [50] D. Bulmash, C.-X. Liu, and X.-L. Qi, *Phys. Rev. B* **89**, 081106 (2014).
- [51] K. Dolui and T. Das, [arXiv:1412.2607v1](https://arxiv.org/abs/1412.2607v1).
- [52] J. Liu and D. Vanderbilt, *Phys. Rev. B* **90**, 155316 (2014).
- [53] R. Okugawa and S. Murakami, *Phys. Rev. B* **89**, 235315 (2014).
- [54] D. Hsieh, Y. Xia, D. Qian, L. Wray, F. Meier, J. H. Dil, J. Osterwalder, L. Patthey, A. V. Fedorov, H. Lin, A. Bansil, D. Grauer, Y. S. Hor, R. J. Cava, and M. Z. Hasan, *Phys. Rev. Lett.* **103**, 146401 (2009).
- [55] D. Hsieh, Y. Xia, L. Wray, D. Qian, A. Pal, J. H. Dil, J. Osterwalder, F. Meier, G. Bihlmayer, C. L. Kane, Y. S. Hor, R. J. Cava, and M. Z. Hasan, *Science* **323**, 919 (2009).
- [56] W. Lei, R. J. Gu, J. Antoszewski, J. Dell, and L. Faraone, *J. Electron. Mater.* **43**, 2788 (2014).
- [57] *Properties of Narrow Gap Cadmium-based Compounds*, edited by P. Capper (IEEE, London, 1994).
- [58] See Supplemental material at <http://link.aps.org/supplemental/10.1103/PhysRevLett.114.236805> for more details.

Spin chirality tuning and topological semi-metals in strained $\text{HgTe}_x\text{S}_{1-x}$

— Supplementary Material —

Tomáš Rauch,¹ Steven Achilles,¹ Jürgen Henk,¹ and Ingrid Mertig^{1,2}

¹*Institute of Physics, Martin Luther University Halle-Wittenberg, Halle (Saale), Germany**

²*Max Planck Institute for Microstructure Physics, Halle (Saale), Germany*

(Dated: May 22, 2015)

FIRST-PRINCIPLES ELECTRONIC STRUCTURE CALCULATIONS

For the *ab initio* determination of the bulk electronic structures, we performed density-functional calculations using a homemade screened Korrington-Kohn-Rostoker (KKR) computer code. In the muffin-tin approximation, the potential is approximated spherical within site-centered spheres and constant otherwise. It turned out that four spheres have to be used within the elementary unit cell of HgTe and HgS: one for Hg, one for Te or S, and two ‘empty’ spheres to account for the interstitial region.

We have performed both scalar-relativistic and fully relativistic calculations. In the former, which relies on the Schrödinger equation, spin-orbit coupling is not taken into account. For the latter, we solve the Dirac equation which *per se* includes all relativistic effects, in particular spin-orbit coupling.

The self-consistent solution of the Kohn-Sham equation requires integration over energy and the Brillouin zone. The integration over energy is performed in the complex energy plane. The contour consists of a semi-circle, a straight line parallel to the real axis, and Matsubara frequencies. Forty complex energy points between the bottom of the valence bands and the Fermi level have been used. The integration over the first Brillouin zone is done on a $48 \times 48 \times 48$ mesh.

The band structure is obtained by solving a non-linear eigenvalue problem for 300 real energies, each associated with 1280 wavevectors along the high symmetry lines.

TIGHT-BINDING CALCULATIONS

The main results of this work are achieved by means of an *ab-initio* based tight binding (TB) model. First, the band structures of HgTe and HgS with and without SOC were calculated in the KKR method. Then, the Slater-Koster (SK) parameters of a next-nearest neighbor TB model were optimized using a Monte Carlo method, using the KKR bands as reference. To describe relativistic effects in the TB model, the spin-orbit coupling constant λ for the *p* orbitals is set to reproduce the Γ_7 – Γ_8 band gap of the KKR calculations. The results of this optimization are shown in Figs. S1 and S2.

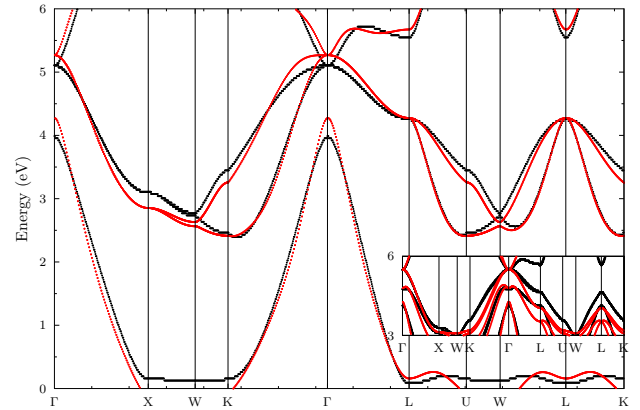


FIG. S1. Bulk band structure of HgTe without spin-orbit coupling in the region of the *p* bands. Black: density-functional calculations; red: tight-binding calculations. Inset: bulk band structures with spin-orbit coupling included.

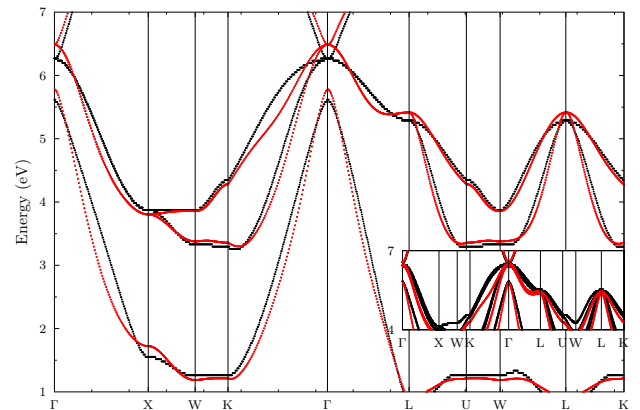


FIG. S2. As Figure S1 but for HgS.

Strain

Strain has been applied in the [001] direction, described by a parameter α . This ‘out-of plane’ strain is accompanied by in-plane strain β . The parameters α and β are

TABLE I. Slater-Koster tight-binding parameters for HgTe and HgS. E^s , E^p , E^d are the on-site energies, λ_p is the spin-orbit coupling of the p orbitals. The subscript of the Slater-Koster parameters indicates the atom: 1 for Hg, 2 for Te or S, respectively. All numbers in eV.

	HgTe	HgS
E_1^s	-1.034	-1.284
E_2^s	-10.343	-11.691
E_1^p	3.896	5.075
E_2^p	-1.650	-1.184
E_1^d	-6.552	-6.365
E_2^d	9.713	6.176
λ_p	0.29	-0.053
$(ss\sigma)_{12}$	0.730	1.429
$(sp\sigma)_{12}$	1.623	1.849
$(ps\sigma)_{12}$	0.775	0.774
$(sd\sigma)_{12}$	1.225	0.837
$(ds\sigma)_{12}$	-0.696	-0.921
$(pp\sigma)_{12}$	1.431	1.942
$(pp\pi)_{12}$	-0.923	-0.629
$(pd\sigma)_{12}$	-0.084	0.660
$(dp\sigma)_{12}$	0.378	0.917
$(pd\pi)_{12}$	0.608	0.174
$(dp\pi)_{12}$	-0.291	-0.457
$(dd\sigma)_{12}$	-0.904	-0.370
$(dd\pi)_{12}$	-0.870	-0.291
$(dd\delta)_{12}$	1.107	-0.135
$(ss\sigma)_{11}$	-0.090	-0.232
$(sp\sigma)_{11}$	-0.352	0.029
$(sd\sigma)_{11}$	-0.231	0.028
$(pp\sigma)_{11}$	0.435	0.551
$(pp\pi)_{11}$	-0.267	-0.172
$(pd\sigma)_{11}$	-0.571	-0.256
$(pd\pi)_{11}$	0.299	-0.243
$(dd\sigma)_{11}$	0.094	-0.121
$(dd\pi)_{11}$	-0.110	0.085
$(dd\delta)_{11}$	-0.052	0.003
$(ss\sigma)_{22}$	-0.039	-0.302
$(sp\sigma)_{22}$	0.004	0.361
$(sd\sigma)_{22}$	0.596	-0.563
$(pp\sigma)_{22}$	0.280	0.857
$(pp\pi)_{22}$	0.118	-0.066
$(pd\sigma)_{22}$	0.601	-1.649
$(pd\pi)_{22}$	0.076	0.242
$(dd\sigma)_{22}$	-0.370	-0.838
$(dd\pi)_{22}$	-0.756	0.245
$(dd\delta)_{22}$	0.115	-0.007

defined as

$$a_{\parallel} = \beta a, \quad (\text{S1})$$

$$a_{\perp} = \alpha a, \quad (\text{S2})$$

with a being the original lattice constant of the unstrained cubic system; a_{\parallel} and a_{\perp} are the in-plane and out-of plane lattice constants of the strained sample, respectively. The relation of α and β is given by the elastic constants C_{11} and C_{12} [1],

$$\alpha = 1 - 2(\beta - 1) \frac{C_{12}}{C_{11}}. \quad (\text{S3})$$

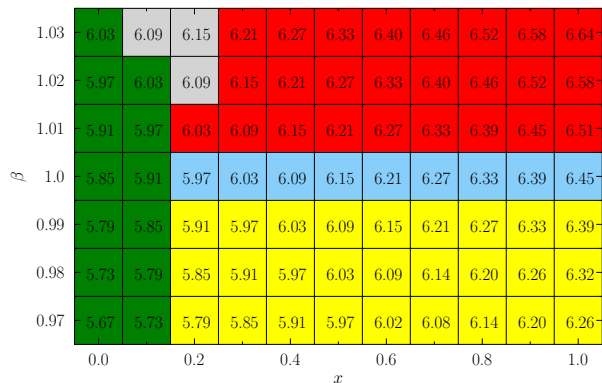


FIG. S3. Same as Figure 1 of the Paper but with in-plane lattice constants a_{\parallel} (in Å) for each point in the topological phase diagram.

To account for the distance-dependence of the TB parameters we applied Harrison's rule,[2]

$$(\text{SK})_{\text{strained}} = \left(\frac{d_{\text{unstrained}}}{d_{\text{strained}}} \right)^2 (\text{SK})_{\text{unstrained}}, \quad (\text{S4})$$

in which (SK) denote a SK parameter in Table I. d_{strained} and $d_{\text{unstrained}}$ are the interatomic distances for the strained and the unstrained sample, respectively.

Assuming the lattice constant of unstrained $\text{HgTe}_x\text{S}_{1-x}$ depends linearly on x , we calculate the in-plane lattice constants a_{\parallel} for each point of the topological phase diagram (Fig. S3). This information may be helpful in finding suitable substrates for experimental realizations of strained samples.

Alloying

The alloying of HgTe and HgS was simulated by both the virtual crystal approximation (VCA) and the coherent potential approximation (CPA) [3, 4].

In the VCA for $\text{HgTe}_x\text{S}_{1-x}$, the TB parameters and the elastic constants are scaled linearly with the concentration x . This approach allows to calculate both the band structure and the eigenstates; the latter serve as input for the subsequent calculations of the topological invariants.

In the CPA, the alloying is described by a complex self-energy which is added to the Hamiltonian matrix. The self-energy is calculated self-consistently for a given x and accounts for renormalization of the band energies and lifetime broadening. The electronic structure is obtained from the resulting Green function from the Bloch spectral density. Being a Green function approach, the CPA does not allow to calculate the topological invariants.

Typically, the CPA provides a better description of the alloys than the VCA, with the drawback that the

topological invariants cannot be calculated. Since these invariants are essential for the present investigation, we checked the VCA results versus the CPA results. Of particular importance are the critical concentration x_c at which a topological phase transition takes place and the fundamental band gap closes. The x_c 's of VCA and CPA differ by less than 0.05.

Topological invariants

To build up a topological phase diagram, we varied the alloy concentration x and the strain β .

\mathcal{Z}_2 invariants were calculated for all insulating samples, using two methods. The first calculational scheme, proposed by Fukui and Hatsugai [5], relies on the Fu-Kane expression [6] and uses a discrete wavevector mesh in the BZ. In the second approach, the evolution of Wannier function centers along lines in the BZ has been tracked [7]. Both methods yield identical results.

For the calculation of mirror Chern numbers we follow the concept of spin Chern numbers [8]. For all wavevectors \mathbf{k} in a mirror plane, the Bloch states are classified according to their mirror eigenvalue $\pm i$. For each class the Chern number $c_{\pm i}$ is calculated as an integral of the Berry curvature [9] over the intersection of the BZ with the mirror plane. The mirror Chern number c_m is the difference of the two Chern numbers,

$$c_m = \frac{1}{2} (c_{+i} - c_{-i}). \quad (\text{S5})$$

Surface electronic structure

A nontrivial topological phase is accompanied by the emergence of topological surface states that are protected by a symmetry of the system (here: time reversal and mirror symmetries); this is the bulk-boundary correspondence. To corroborate and check the topological phase diagram—which is obtained from electronic structure cal-

culations for the bulk—we computed the electronic structure of (001) surfaces.

For this purpose we utilized a Green function renormalization scheme [10, 11] which mimics semi-infinite systems. The outcome is the layer-resolved Green function matrix $\mathbf{G}_{lm}(E, \mathbf{k}_{\parallel})$; l and m denote layers, while the ‘internal’ indices of \mathbf{G} are orbital and atom. The surface electronic structure is then obtained from the layer-resolved spectral density of the topmost layer ($l = m = 0$),

$$N_0(E, \mathbf{k}_{\parallel}) = -\frac{1}{\pi} \text{Im tr } \mathbf{G}_{00}(E + i\eta, \mathbf{k}_{\parallel}). \quad (\text{S6})$$

η is a small offset from the energy axis, leading to a broadening of the spectral density ($\eta = 0.0005$ eV). The orbital composition and the spin texture of the surface states is deduced from partial traces in eq. (S6).

-
- * Corresponding author: tomas.rauch@physik.uni-halle.de
- [1] S. Adachi, *Properties of Semiconductor Alloys* (Wiley, United Kingdom, 2009).
 - [2] W. A. Harrison, *Elementary Electronic Structure*, revised ed. (World Scientific, New Jersey, 2004).
 - [3] P. M. Laufer and D. A. Papaconstantopoulos, *Physical Review B* **35** (1987).
 - [4] J. S. Faulkner, *Physical Review B* **13** (1976).
 - [5] T. Fukui and Y. Hatsugai, *Journal of the Physical Society of Japan* **76**, 053702 (2007).
 - [6] L. Fu and C. Kane, *Physical Review B* **74**, 1 (2006).
 - [7] R. Yu, X. L. Qi, A. Bernevig, Z. Fang, and X. Dai, *Physical Review B* **84**, 1 (2011).
 - [8] E. Prodan, *Physical Review B* **80**, 1 (2009).
 - [9] D. J. Thouless, M. Kohmoto, M. P. Nightingale, and M. den Nijs, *Physical Review Letters* **49**, 405 (1982).
 - [10] J. Henk and W. Schattke, *Computer Physics Communications* **77**, 69 (1993).
 - [11] A. Bödicker, W. Schattke, J. Henk, and R. Feder, *J. Phys.: Condens. Matter* **6**, 1927 (1994).

CONCLUSIONS

In the present work, various properties of different topological insulators (TIs) and metals were studied within an *ab initio* based tight-binding (TB) model. The Slater-Koster (SK) parameters were either extracted from pre-calculated *ab initio* band structures or taken from literature. In the TB model, the effects of several perturbations of the initial system, such as strain, disorder or an external magnetic field, were analysed. The aim of these simulations was the investigation of topological properties and their variation upon specific modifications. For each value of system parameters, e.g., the lattice constant or defects concentration, topological invariants of the bulk electronic states were calculated, primarily as an integrated Berry curvature, which is well accessible in the TB model. In addition, the surface electronic structure was calculated for different parameter sets. The connection between topological invariants and surface states was proved and the properties of the latter were probed under different conditions. Being a cumulative thesis, this work includes results published in peer-reviewed journals.

The first publication (section 6.2) showed the possibility of tuning the different materials with rocksalt structure from a normal insulating phase to a topologically crystalline one by increasing the ambient pressure. The pressure necessary to enter the TCI phase was explained microscopically by examining the properties of the hybridized *s-p* orbitals of different compounds. Thus, PbTe, PbS and PbSe were proposed to become topologically crystalline insulators (TCIs) under hydrostatic pressure, next to the previously known SnTe.

In the second study (section 6.3), the possibility of characterizing \mathcal{Z}_2 TIs also by the mirror Chern number, which is the invariant for TCIs with mirror symmetries, was examined for the example of Bi₂Te₃. A very important result of this work is the fact that magnetic fields or a magnetization oriented perpendicular to a mirror plane of the system do not break the corresponding mirror symmetry. The mirror Chern number is still well defined in this case and the Dirac point of the surface state is protected by the symmetry, as it is otherwise not the case for an arbitrary oriented magnetic field. These findings explain the existence of ungapped surface states in \mathcal{Z}_2 TIs, even when time-reversal symmetry is broken by magnetic impurities, a magnetic toplayer or an external magnetic field.

An interface between a \mathcal{Z}_2 TI and a TCI was modelled in the next paper (section 6.4). Based on a previous discussion of interface states of TIs being preserved or annihilated depending on the respective topological invariants of the two materials forming the interface, the interface between Bi₂Te₃ and SnTe was studied. A global mirror symmetry was identified allowing for the calculation of the mirror Chern numbers that read $n_M = -1$ for Bi₂Te₃ and $n_M = -2$ for SnTe. The number of interface states is given by the modulus of the total mirror Chern number across the interface, $|n_{\text{int}}| = \left| n_M^{\text{Bi}_2\text{Te}_3} - n_M^{\text{SnTe}} \right| = 1$. This was confirmed by an electronic structure calcula-

tion for the interface, showing only one interface state. The other two surface states that occur at the free surfaces of the respective materials annihilate each other during the interface formation.

Finally, in the last publication (section 6.5) the topological properties were calculated in a disordered $\text{HgTe}_x\text{S}_{1-x}$ system for a phase diagram spanned by concentration x and strain in (001) direction. First, the known facts of negatively strained HgTe and unstrained HgS being TIs with opposite spin chirality of the surface states were confirmed by calculations of the topological invariants and the surface electronic structure. The phase boundary of these phases is located at $x \approx 0.15$ across which the effective spin-orbit coupling (SOC) constant of the p orbitals changes sign. A second, even more important result of the work was the identification of two additional topological phases; the Weyl semimetal (WSM) and the topological Dirac semimetal (TDS) phase. The Weyl points in the WSM phase are located in the k_x - k_y plane and their projections can be observed in the surface electronic structure of the (001) surface. Each Weyl point possesses a topological charge of ± 1 . In addition, the Weyl point projections are connected by surface states whose Fermi energy cut forms open lines connecting Weyl point projections with opposite topological charges, called the Fermi arcs. The second metallic phase, the TDS, was found for negatively strained HgTe, featuring doubly degenerate bands crossing on the Γ -Z line of the Brillouin zone (BZ). The dispersion of the bulk bands in the vicinity of the crossings is linear, forming the bulk Dirac states. The topological character was confirmed by calculating the value of the \mathcal{Z}_2 invariant for the k_x - k_y plane as $\nu = 1$. Owing to these findings, the (100) surface features the projections of the two bulk Dirac states as well as the surface state emerging from the topologically non-trivial character of the k_x - k_y plane.

Summarizing, the bulk topological invariants and the surface electronic structure were investigated in this work. Since the topological materials should be used in real-world applications, the transport properties of both the bulk and surface Dirac states have to be studied. Therefore, the next step based on the current results is to calculate the transport properties of the topological materials for different geometries, especially parallel and perpendicular to the surface. This is possible for the ballistic regime by means of a Green function approach in the TB model. In this way all the topological properties can be calculated in one common model, including electronic and spin transport.

BIBLIOGRAPHY

- [1] **K. v. Klitzing, G. Dorda, and M. Pepper**, *New method for high-accuracy determination of the fine-structure constant based on quantized Hall resistance*, Phys. Rev. Lett. **45**, 494 (1980).
- [2] **R. B. Laughlin**, *Quantized Hall conductivity in two dimensions*, Phys. Rev. B **23**, 5632 (1981).
- [3] **D. J. Thouless, M. Kohmoto, M. P. Nightingale, and M. den Nijs**, *Quantized Hall conductance in a two-dimensional periodic potential*, Phys. Rev. Lett. **49**, 405 (1982).
- [4] **D. Hsieh et al.**, *A tunable topological insulator in the spin helical Dirac transport regime*, Nature **460**, 1101 (2009).
- [5] **D. Hsieh et al.**, *Observation of time-reversal-protected single-Dirac-cone topological-insulator states in Bi_2Te_3 and Sb_2Te_3* , Phys. Rev. Lett. **103**, 146401 (2009).
- [6] **T. Zhang et al.**, *Experimental demonstration of topological surface states protected by time-reversal symmetry*, Phys. Rev. Lett. **103**, 266803 (2009).
- [7] **P. Cheng et al.**, *Landau quantization of topological surface states in Bi_2Se_3* , Phys. Rev. Lett. **105**, 076801 (2010).
- [8] **L. Barreto, F. Edler, J. Mi, M. Bremholm, B. B. Iversen, C. Frydendahl, M. Bianchi, and P. Hofmann**, *Direct measurement of surface transport on a bulk topological insulator* (2013), arXiv:1310.0202v1.
- [9] **I. Zutic, J. Fabian, and S. D. Sarma**, *Spintronics: Fundamentals and applications*, Rev. Mod. Phys. **76**, 323 (2004).
- [10] **L. Fu and C. Kane**, *Superconducting proximity effect and Majorana fermions at the surface of a topological insulator*, Phys. Rev. Lett. **100**, 096407 (2008).
- [11] **M. Berry**, *Quantal phase factors accompanying adiabatic changes*, Proc. Roy. Soc. London A **392**, 45 (1984).
- [12] **M. Born and V. Fock**, *Beweis des Adiabatenatzes*, Z. Phys. A **51**, 165 (1928).
- [13] **G. Moore and N. Read**, *Nonabelions in the fractional quantum hall effect*, Nucl. Phys. B **360**, 362 (1991).
- [14] **D. Xiao, M.-C. Chang, and Q. Niu**, *Berry phase effects on electronic properties*, Rev. Mod. Phys. **82**, 1959 (2010).
- [15] **Y.-Q. Ma, S. Chen, H. Fan, and W.-M. Liu**, *Abelian and non-Abelian quantum geometric tensor*, Phys. Rev. B **81**, 245129 (2010).
- [16] **J. Zak**, *Berry's phase for energy bands in solids*, Phys. Rev. Lett. **62**, 2747 (1989).
- [17] **F. Bloch**, *Über die Quantenmechanik der Elektronen in Kristallgittern*, Z. Phys. **52**, 555 (1929).
- [18] **M. Born and R. Oppenheimer**, *Zur Quantentheorie der Molekeln*, Ann. Phys. **84**, 30 (1927).
- [19] **J. C. Slater and G. F. Koster**, *Simplified LCAO method for the periodic potential problem*, Phys. Rev. **94**, 1498 (1954).

Bibliography

- [20] **D. A. Papaconstantopoulos** and **M. J. Mehl**, *The Slater-Koster tight-binding method: a computationally efficient and accurate approach*, J. Phys. F: Met. Phys. **15**, R413 (2003).
- [21] **P.-O. Löwdin**, *On the non-orthogonality problem connected with the use of atomic wave functions in the theory of molecules and crystals*, J. Chem. Phys. **18**, 365 (1950).
- [22] **K. Takegahara**, **Y. Aoki**, and **A. Yanase**, *Slater-Koster tables for f electrons*, J. Phys. C: Sol. State Phys. **13**, 583 (1980).
- [23] **M. D. Jaffe** and **J. Singh**, *Inclusion of spin-orbit coupling into tight binding bandstructure calculations for bulk and superlattice semiconductors*, Sol. State Commun. **62**, 399 (1987).
- [24] **K. Hagiwara** et al., *Review of particle properties*, Phys. Rev. D **66**, 010001 (2002).
- [25] **M. D. Jones** and **R. C. Albers**, *Spin-orbit coupling in an f-electron tight-binding model* (2008), arXiv:0806.0420v1.
- [26] **P. Zeeman**, *On the influence of magnetism on the nature of the light emitted by substance*, Phil. Mag. **43**, 226 (1897).
- [27] **T. Fließbach**, *Quantenmechanik* (Spektrum Akademischer Verlag Heidelberg, 2008).
- [28] **N. Metropolis**, **A. W. Rosenbluth**, **M. N. Rosenbluth**, **A. H. Teller**, and **E. Teller**, *Equation of state calculations by fast computing machines*, J. Chem. Phys. **21**, 1087 (1953).
- [29] **P. Vogl**, **H. P. Hjalmarson**, and **J. D. Dow**, *A semi-empirical tight-binding theory of the electronic structure of semiconductors*, J. Phys. Chem. Sol. **44**, 365 (1983).
- [30] **G. Klimeck**, **R. Bowen**, **T. B. Boykin**, **C. Salazar-Lazaro**, **T. a. Cwik**, and **A. Stoica**, *Si tight-binding parameters from genetic algorithm fitting*, Supperlattice. Microst. **27**, 77 (2000).
- [31] **S. Sapra**, **N. Shanthi**, and **D. Sarma**, *Realistic tight-binding model for the electronic structure of II-VI semiconductors*, Phys. Rev. B **66**, 205202 (2002).
- [32] **N. Marzari** and **D. Vanderbilt**, *Maximally localized generalized Wannier functions for composite energy bands*, Phys. Rev. B **56**, 847 (1997).
- [33] **W. A. Harrison**, *New tight-binding parameters for covalent solids obtained using Louie peripheral states*, Phys. Rev. B **24**, 5835 (1981).
- [34] **L. Vitos**, *Computational quantum mechanics for materials engineers* (Springer-Verlag London, 2007).
- [35] **K. A. Mäder** and **A. Zunger**, *Short- and long-range-order effects on the electronic properties of III-V semiconductor alloy*, Phys. Rev. B **51**, 10462 (1995).
- [36] **L. Nordheim**, *Zur Elektronentheorie der Metalle*, Ann. Phys. **401**, 607 (1931).
- [37] **L. Bellaiche** and **D. Vanderbilt**, *Virtual crystal approximation revisited: Application to dielectric and piezoelectric properties of perovskites*, Phys. Rev. B **61**, 7877 (2000).
- [38] **J. S. Faulkner**, *The modern theory of alloys*, Prog. Mat. Sci. **27**, 1 (1982).
- [39] **P. Soven**, *Coherent-potential model of substitutional disordered alloys*, Phys. Rev. **156**, 809 (1964).
- [40] **F. Yonezawa** and **K. Morigaki**, *Coherent potential approximation*, Prog. Theor. Phys. Sup. **53**, 1 (1973).

- [41] **H. Ehrenreich** and **L. M. Schwartz**, *The electronic structure of alloys*, Sol. State Phys. **31**, 150 (1976).
- [42] **J. S. Faulkner**, *Electronic states of substochiometric compounds and application to palladium hydride*, Phys. Rev. B **13**, 2391 (1976).
- [43] **P. M. Laufer** and **D. A. Papaconstantopoulos**, *Tight-binding coherent-potential-approximation study of the electronic states of palladium-noble-metal alloys*, Phys. Rev. B **35**, 9019 (1987).
- [44] **D. A. Papaconstantopoulos**, **A. Gonis**, and **P. M. Laufer**, *Tight-binding coherent-potential approximation including off-diagonal disorder*, Phys. Rev. B **40**, 196 (1989).
- [45] **J. Hartung**, **B. Elpelt**, and **K.-H. Klösener**, *Statistik: Lehr- und Handbuch der angewandten Statistik* (Oldenbourg Verlag München Wien, 2005).
- [46] **J. Henk** and **W. Schattke**, *A subroutine package for computing Green's functions of relaxed surfaces by the renormalization method*, Comp. Phys. Commun. **77**, 69 (1993).
- [47] **A. Bödicker**, **W. Schattke**, **J. Henk**, and **R. Feder**, *Interface electronic structure by the renormalization method: theory and application to Sb/GaAs*, J. Phys.: Condens. Matt. **6**, 1927 (1994).
- [48] **M. Gradhand**, **D. V. Fedorov**, **F. Pientka**, **P. Zahn**, **I. Mertig**, and **B. L. Györfly**, *First-principle calculations of the Berry curvature of Bloch states for charge and spin transport of electrons.*, J. Phys.: Condens. Matt. **24**, 213202 (2012).
- [49] **F. Pientka**, *Geometrical concepts in the band theory of solids*, PhD thesis (MLU Halle-Wittenberg, Halle (Germany), 2010).
- [50] **L. Gaggero-Sager** and **S. Vlaev**, *Exchange and correlation in a semi-empirical tight binding calculation within the Thomas-Fermi approximation*, phys. stat. sol. (b) **215**, 1049 (1999).
- [51] **C. M. Goringe**, **D. R. Bowler**, and **E. Hernandez**, *Tight-binding modelling of materials*, Rep. Prog. Phys. **60**, 1447 (1997).
- [52] **W. H. Press**, **S. A. Teukolsky**, **W. A. Vetterling**, and **B. P. Flannery**, *Numerical recipes in C: The art of scientific computing* (Cambridge university press, Cambridge, 1992).
- [53] **M. Hasan** and **C. Kane**, *Colloquium: Topological insulators*, Rev. Mod. Phys. **82**, 3045 (2010).
- [54] **J. E. Moore**, *The birth of topological insulators*, Nature **464**, 194 (2010).
- [55] **X.-L. Qi** and **S.-C. Zhang**, *Topological insulators and superconductors*, Rev. Mod. Phys. **83**, 1057 (2011).
- [56] **S.-Q. Shen**, *Topological insulators* (Springer-Verlag Berlin Heidelberg, 2012).
- [57] **J. D. Jackson**, *Classical electrodynamics* (John Wiley & Sons Ltd., 1962).
- [58] **F. D. M. Haldane**, *Model for a quantum Hall effect without Landau levels: Condensed-matter realization of the "parity anomaly"*, Phys. Rev. Lett. **61**, 2015 (1988).
- [59] **K. F. Garrity** and **D. Vanderbilt**, *Chern insulators from heavy atoms on magnetic substrates*, Phys. Rev. Lett. **110**, 116802 (2013).
- [60] **C.-X. Liu**, **X.-L. Qi**, **X. Dai**, **Z. Fang**, and **S.-C. Zhang**, *Quantum anomalous Hall effect in $Hg_{1-y}Mn_yTe$ quantum wells*, Phys. Rev. Lett. **101**, 146802 (2008).

Bibliography

- [61] **Z. Qiao, S. A. Yang, W. Feng, W.-K. Tse, J. Ding, Y. Yao, J. Wang, and Q. Niu**, *Quantum anomalous Hall effect in graphene from Rashba and exchange effects*, Phys. Rev. B **82**, 161414 (2010).
- [62] **R. Yu, W. Zhang, H.-J. Zhang, S.-C. Zhang, X. Dai, and Z. Fang**, *Quantized anomalous Hall effect in magnetic topological insulators*, Science **329**, 61 (2010).
- [63] **C.-Z. Chang et al.**, *Experimental observation of the quantum anomalous Hall effect in a magnetic topological insulator.*, Science **340**, 167 (2013).
- [64] **M. Kohmoto**, *Topological invariant and the quantization of the Hall conductance*, Ann. Phys. **160**, 343 (1985).
- [65] **J. E. Avron, R. Seiler, and B. Simon**, *Homotopy and quantization in condensed matter physics*, Phys. Rev. Lett. **51**, 51 (1983).
- [66] **Y. Hatsugai**, *Characterization of topological insulators: Chern numbers for ground state multiplet*, J. Phys. Soc. Jpn. **74**, 1374 (2005).
- [67] **F. Haldane**, *Berry curvature on the Fermi surface: Anomalous Hall effect as a topological Fermi-liquid property*, Phys. Rev. Lett. **93**, 206602 (2004).
- [68] **Y. Hatsugai**, *Chern number and edge states in the Integer quantum Hall effect*, Phys. Rev. Lett. **71**, 3697 (1993).
- [69] **T. Thonhauser and D. Vanderbilt**, *Insulator/Chern-insulator transition in the Haldane model*, Phys. Rev. B **74**, 235111 (2006).
- [70] **M. I. Dyakonov and V. I. Perel**, *Current-induced spin orientation of electrons in semiconductors*, Phys. Lett. A **35**, 459 (1971).
- [71] **N. F. Mott**, *The Scattering of Fast Electrons by Atomic Nuclei*, Proc. Roy. Soc. A **124**, 425 (1929).
- [72] **T. Kimura, Y. Otani, T. Sato, S. Takahashi, and S. Maekawa**, *Room-temperature reversible spin Hall effect*, Phys. Rev. Lett. **98**, 156601 (2007).
- [73] **C. L. Kane and E. J. Mele**, *Z₂ topological order and the quantum spin Hall effect*, Phys. Rev. Lett. **95**, 146802 (2005).
- [74] **C. L. Kane and E. J. Mele**, *Quantum spin Hall effect in graphene*, Phys. Rev. Lett. **95**, 226801 (2005).
- [75] **B. A. Bernevig, T. L. Hughes, and S.-C. Zhang**, *Quantum spin Hall effect and topological phase transition in HgTe quantum wells.*, Science **314**, 1757 (2006).
- [76] **M. König, S. Wiedmann, C. Brüne, A. Roth, H. Buhmann, L. W. Molenkamp, X.-L. Qi, and S.-C. Zhang**, *Quantum spin Hall insulator state in HgTe quantum wells.*, Science **318**, 766 (2007).
- [77] **L. Fu and C. Kane**, *Time reversal polarization and a Z₂ adiabatic spin pump*, Phys. Rev. B **74**, 195312 (2006).
- [78] **T. Fukui and Y. Hatsugai**, *Quantum spin Hall effect in three dimensional materials: Lattice computation of Z₂ topological invariant and its application to Bi and Sb*, J. Phys. Soc. Jpn. **76**, 053702 (2007).
- [79] **J. E. Moore and L. Balents**, *Topological invariants of time-reversal-invariant band structures*, Phys. Rev. B **75**, 121306 (2007).
- [80] **X.-L. Qi, T. L. Hughes, and S.-C. Zhang**, *Topological field theory of time-reversal invariant insulators*, Phys. Rev. B **78**, 195424 (2008).

- [81] **R. Roy**, *Z₂ classification of quantum spin Hall systems: An approach using time-reversal invariance*, Phys. Rev. B **79**, 195321 (2009).
- [82] **T. Inui, Y. Tanabe, and Y. Onodera**, *Group theory and its application in physics* (Springer-Verlag Berlin Heidelberg, 1990).
- [83] **T. Fukui, Y. Hatsugai, and H. Suzuki**, *Chern numbers in discretized Brillouin zone: Efficient method of computing (spin) Hall conductances*, J. Phys. Soc. Jpn. **74**, 1674 (2005).
- [84] **R. Resta**, *Macroscopic polarization in crystalline dielectrics: the geometric phase approach*, Rev. Mod. Phys. **66**, 899 (1994).
- [85] **R. Yu, X. L. Qi, A. Bernevig, Z. Fang, and X. Dai**, *Equivalent expression of Z₂ topological invariant for band insulators using the non-Abelian Berry connection*, Phys. Rev. B **84**, 075119 (2011).
- [86] **A. Soluyanov and D. Vanderbilt**, *Wannier representation of Z₂ topological insulators*, Phys. Rev. B **83**, 035108 (2011).
- [87] **A. Alexandradinata, X. Dai, and B. A. Bernevig**, *Wilson-loop characterization of inversion-symmetric topological insulators*, Phys. Rev. B **89**, 155114 (2014).
- [88] **A. A. Soluyanov**, *Topological aspects of band theory*, PhD thesis (Graduate School-New Brunswick Rutgers, The State University of New Jersey, 2012).
- [89] **H. A. Kramers**, *Théorie générale de la rotation paramagnétique dans les cristaux*, Proc. Amsterdam Acad. **33**, 959 (1930).
- [90] **C. Xu and J. Moore**, *Stability of the quantum spin Hall effect: Effects of interactions, disorder, and Z₂ topology*, Phys. Rev. B **73**, 045322 (2006).
- [91] **L. Fu, C. Kane, and E. Mele**, *Topological insulators in three dimensions*, Phys. Rev. Lett. **98**, 106803 (2007).
- [92] **R. Roy**, *Characterization of three-dimensional topological insulators by two-dimensional invariants*, New J. Phys. **12**, 065009 (2010).
- [93] **L. Fu and C. Kane**, *Topological insulators with inversion symmetry*, Phys. Rev. B **76**, 045302 (2007).
- [94] **D. Hsieh, D. Qian, L. Wray, Y. Xia, Y. S. Hor, R. J. Cava, and M. Z. Hasan**, *A topological Dirac insulator in a quantum spin Hall phase*, Nature **452**, 970 (2008).
- [95] **Y. Xia et al.**, *Observation of a large-gap topological-insulator class with a single Dirac cone on the surface*, Nature Phys. **5**, 398 (2009).
- [96] **H. Zhang, C.-x. Liu, X.-l. Qi, X. Dai, Z. Fang, and S.-c. Zhang**, *Topological insulators in Bi₂Se₃, Bi₂Te₃ and Sb₂Te₃ with a single Dirac cone on the surface*, Nature Phys. **5**, 438 (2009).
- [97] **E. Prodan**, *Robustness of the spin-Chern number*, Phys. Rev. B **80**, 125327 (2009).
- [98] **S.-Q. Shen, W.-Y. Shan, and H.-Z. Lu**, *Topological Insulator and the Dirac Equation*, Spin **01**, 33 (2011).
- [99] **L. Fu**, *Hexagonal warping effects in the surface states of the topological insulator Bi₂Te₃*, Phys. Rev. Lett. **103**, 266801 (2009).
- [100] **L. Fu**, *Topological crystalline insulators*, Phys. Rev. Lett. **106**, 106802 (2011).

Bibliography

- [101] **T. H. Hsieh, H. Lin, J. Liu, W. Duan, A. Bansil, and L. Fu**, *Topological crystalline insulators in the SnTe material class*, Nature Comms. **3**, 982 (2012).
- [102] **Y. Tanaka, Z. Ren, T. Sato, K. Nakayama, S. Souma, T. Takahashi, K. Segawa, and Y. Ando**, *Experimental realization of a topological crystalline insulator in SnTe*, Nature Phys. **8**, 800 (2012).
- [103] **J. Teo, L. Fu, and C. Kane**, *Surface states and topological invariants in three-dimensional topological insulators: Application to $Bi_{1-x}Sb_x$* , Phys. Rev. B **78**, 045426 (2008).
- [104] **Y. Kim, C. Kane, E. Mele, and A. M. Rappe**, *Layered topological crystalline insulators*, Phys. Rev. Lett. **115**, 086802 (2015).
- [105] **K. S. Novoselov, A. K. Geim, S. V. Morozov, D. Jiang, Y. Zhang, S. V. Dubonos, I. V. Grigorieva, and A. A. Firsov**, *Electric field effect in atomically thin carbon films*, Science **306**, 666 (2004).
- [106] **Z. Wang, H. Weng, Q. Wu, X. Dai, and Z. Fang**, *Three-dimensional Dirac semimetal and quantum transport in Cd_3As_2* , Phys. Rev. B **88**, 125427 (2013).
- [107] **B.-J. Yang and N. Nagaosa**, *Classification of stable three-dimensional Dirac semimetals with nontrivial topology.*, Nature Comms. **5**, 4898 (2014).
- [108] **B.-J. Yang, T. Morimoto, and A. Furusaki**, *Topological charges of three-dimensional Dirac semimetals with rotation symmetry*, Phys. Rev. B **92**, 165120 (2015).
- [109] **S. Murakami, S. Iso, Y. Avishai, M. Onoda, and N. Nagaosa**, *Tuning phase transition between quantum spin Hall and ordinary insulating phases*, Phys. Rev. B **76**, 205304 (2007).
- [110] **X. Wan, A. Turner, A. Vishwanath, and S. Savrasov**, *Topological semimetal and Fermi-arc surface states in the electronic structure of pyrochlore iridates*, Phys. Rev. B **83**, 205101 (2011).
- [111] **S. Murakami**, *Phase transition between the quantum spin Hall and insulator phases in 3D: emergence of a topological gapless phase*, New J. Phys. **9**, 356 (2007).
- [112] **B.-J. Yang, M. S. Bahrany, R. Arita, H. Isobe, E.-G. Moon, and N. Nagaosa**, *Theory of topological quantum phase transitions in 3D noncentrosymmetric systems*, Phys. Rev. Lett. **110**, 086402 (2013).
- [113] **R. Okugawa and S. Murakami**, *Dispersion of Fermi arcs in Weyl semimetals and their evolutions to Dirac cones*, Phys. Rev. B **89**, 235315 (2014).
- [114] **J. Liu and D. Vanderbilt**, *Weyl semimetals from noncentrosymmetric topological insulators*, Phys. Rev. B **90**, 155316 (2014).
- [115] **D. Bulmash, C.-X. Liu, and X.-L. Qi**, *Prediction of a Weyl semimetal in $Hg(1-x-y)Cd(x)Mn(y)Te$* , Phys. Rev. B **89**, 081106 (2014).
- [116] **B. Lv et al.**, *Experimental discovery of Weyl semimetal TaAs*, Phys. Rev. X **5**, 031013 (2015).
- [117] **B. Q. Lv et al.**, *Observation of Weyl nodes in TaAs*, Nature Phys. **11**, 724 (2015).
- [118] **H. Weng, C. Fang, Z. Fang, B. A. Bernevig, and X. Dai**, *Weyl semimetal phase in noncentrosymmetric transition-metal monophosphides*, Phys. Rev. X **5**, 011029 (2015).
- [119] **Y. Sun, S.-C. Wu, and B. Yan**, *Topological surface states and Fermi arcs of the noncentrosymmetric Weyl semimetals TaAs, TaP, NbAs, and NbP*, Phys. Rev. B **92**, 115428 (2015).

- [120] **S. M. Young, S. Zaheer, J. C. Y. Teo, C. L. Kane, E. J. Mele, and A. M. Rappe**, *Dirac semimetal in three dimensions*, Phys. Rev. Lett. **108**, 140405 (2012).
- [121] **P. Dirac**, *Quantised singularities in the electromagnetic field*, Proc. Roy. Soc. A **133**, 60 (1931).
- [122] **Y. L. Chen et al.**, *Massive Dirac fermion on the surface of a magnetically doped topological insulator*, Science **329**, 659 (2010).
- [123] **T. Schlenk et al.**, *Controllable magnetic doping of the surface state of a topological insulator*, Phys. Rev. Lett. **110**, 126804 (2013).
- [124] **R. Takahashi and S. Murakami**, *Gapless interface states between topological insulators with opposite Dirac velocities*, Phys. Rev. Lett. **107**, 166805 (2011).

LIST OF PUBLICATIONS

- [TR1] **T. Rauch, S. Achilles, J. Henk, and I. Mertig**, *Spin chirality tuning and topological semimetals in strained $\text{HgTe}_x\text{S}_{1-x}$* , Phys. Rev. Lett. **114**, 236805 (2015).
- [TR2] **T. Rauch, M. Flieger, J. Henk, I. Mertig, and A. Ernst**, *Dual topological character of chalcogenides: Theory for Bi_2Te_3* , Phys. Rev. Lett. **112**, 016802 (2014).
- [TR3] **P. Barone, T. Rauch, D. Di Sante, J. Henk, I. Mertig, and S. Picozzi**, *Pressure-induced topological phase transitions in rocksalt chalcogenides*, Phys. Rev. B **88**, 045207 (2013).
- [TR4] **T. Rauch, M. Flieger, J. Henk, and I. Mertig**, *Nontrivial interface states confined between two topological insulators*, Phys. Rev. B **88**, 245120 (2013).
- [TR5] **N. F. Hinsche, S. Zastrow, J. Gooth, L. Pudewill, R. Zierold, F. Rittweger, T. Rauch, J. Henk, K. Nielsch, and I. Mertig**, *Impact of the topological surface state on the thermoelectric transport in Sb_2Te_3 thin films*, ACS Nano **9**, 4406 (2015).
- [TR6] **F. Munoz, M. G. Vergniory, T. Rauch, J. Henk, E. V. Chulkov, I. Mertig, S. Botti, M. A. L. Marques, and A. H. Romero**, *Topological crystalline insulator in a new Bi semiconducting phase*, Sci. Rep. **6**, 21790 (2016).

EIDESSTATTLICHE ERKLÄRUNG

Hiermit erkläre ich gemäß §5 der Promotionsordnung der Naturwissenschaftlichen Fakultäten I, II, III und des Zentrums für Ingenieurwissenschaften der Martin-Luther-Universität Halle-Wittenberg vom 13.06.2012, dass ich die vorliegende Arbeit

TOPOLOGICAL INSULATORS AND SEMIMETALS: THEORY FOR BULK AND SURFACE ELECTRONIC PROPERTIES

selbstständig und ohne fremde Hilfe verfasst, keine anderen als die angegebenen Quellen und Hilfsmittel benutzt und die den benutzten Werken wörtlich oder inhaltlich entnommenen Stellen als solche kenntlich gemacht habe. Ich erkläre weiterhin, die Angaben wahrheitsgemäß gemacht und weder diese noch eine andere Dissertation an einer anderen wissenschaftlichen Einrichtung vorgelegt zu haben.

Tomáš Rauch

CURRICULUM VITAE

PERSONAL INFORMATION

Name: **Tomáš Rauch**
Address: **Carl-von-Ossietzky-Straße 3, 06114 Halle(Saale), Germany**
Date and place of birth: **17th of Dezember 1986, Frýdlant, Czech Republic**

EDUCATION

since 10/2012 **PhD studies**, *Martin Luther University Halle-Wittenberg, Halle (Germany)*

10/2010 - 09/2012 **Master degree (M.Sc.) physics course**, *Martin Luther University Halle-Wittenberg, Halle (Germany)*, final grade: 1.0
Master thesis: *Topologische Isolatoren im Tight-Binding-Modell (Topological insulators in a Tight-Binding model)*

10/2007 - 09/2010 **Bachelor degree (B.Sc.) physics course**, *Martin Luther University Halle-Wittenberg, Halle (Germany)*, final grade: 1.1
Bachelor thesis: *Effektive Potentialmethode (Effective potential method)*

09/2006 - 05/2007 **High school**, *Podještědské gymnázium Liberec, Liberec (Czech Republic)*

08/2005 - 07/2006 **High school**, *Liborius-Gymnasium Dessau, Dessau-Roßlau (Germany)*

09/1998 - 06/2005 **High school**, *Podještědské gymnázium Liberec, Liberec (Czech Republic)*

09/1993 - 07/1998 **Elementary school**, *ZŠ Lesní, Liberec (Czech Republic)*

ACADEMIC WORK EXPERIENCE

since 01/2013 **Research assistant**, *Institute of Physics, Martin Luther University Halle-Wittenberg, Halle (Germany)*, research group of Prof. Dr. Ingrid Mertig

10/2012 - 12/2012 **Research assistant**, *Max Planck Institute of Microstructure Physics, Halle (Germany)*, fellow group of Prof. Dr. Ingrid Mertig

07/2009 - 09/2012 **Student assistant**, *Institutes of Physics and Mathematics, Martin Luther University Halle-Wittenberg, Halle (Germany)*

09/2008 **Student assistant**, *Institute of Physics, Martin Luther University Halle-Wittenberg, Halle (Germany)*